

**UTILISATION OF NUTMEG SEED SHELL-BASED
MATERIALS FOR MICROPOLLUTANT
REMEDIATION**

Thesis

Submitted in partial fulfilment of the requirements for the
degree of

DOCTOR OF PHILOSOPHY

By

TEEMA THOMAS
(Roll. No. 187CV013)



**DEPARTMENT OF CIVIL ENGINEERING
NATIONAL INSTITUTE OF TECHNOLOGY KARNATAKA,
SURATHKAL, MANGALORE-575025
OCTOBER, 2023**

UTILISATION OF NUTMEG SEED SHELL-BASED MATERIALS FOR MICROPOLLUTANT REMEDICATION

Thesis

Submitted in partial fulfilment of the requirements for the
degree of

DOCTOR OF PHILOSOPHY

By

TEEMA THOMAS

(Roll. No. 187CV013)

Under the guidance of

Dr. ARUN KUMAR THALLA



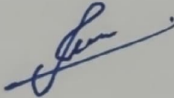
**DEPARTMENT OF CIVIL ENGINEERING
NATIONAL INSTITUTE OF TECHNOLOGY KARNATAKA,
SURATHKAL, MANGALORE-575025
OCTOBER, 2023**

DECLARATION

I hereby *declare* that the Thesis entitled “**UTILISATION OF NUTMEG SEED SHELL-BASED MATERIALS FOR MICROPOLLUTANT REMEDIATION**”, which is being submitted to the **National Institute of Technology Karnataka, Surathkal**, in partial fulfilment of the requirements for the award of the **Degree of Doctor of Philosophy** in the **Department of Civil Engineering** is a *bonafide report of the research work carried out by me*. The material contained in this Thesis has not been submitted to any University or Institution for the award of any degree.

Register Number : 187005CV013

Name of the Research Scholar : Teema Thomas

Signature of the Research Scholar : 

Department of Civil Engineering

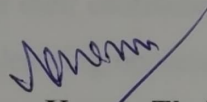
Place: NITK-Surathkal

Date: 19/10/2023

CERTIFICATE

This is to *certify* that the Research Thesis entitled “UTILISATION OF NUTMEG SEED SHELL-BASED MATERIALS FOR MICROPOLLUTANT REMEDIATION” submitted by **Ms. Teema Thomas (187005CV013)** as the record of the research work carried out by her, is *accepted as the Research Thesis submission* in partial fulfilment of the requirements for the award of degree of **Doctor of Philosophy**.

Research guide

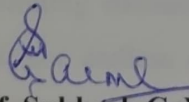


Dr. Arun Kumar Thalla

Professor

Department of Civil Engineering

(Signature with date and seal)



Prof. Subhash C. Yaragal

Chairperson-DRPC

(Signature with date and seal)

Chairman (DRPC)
Department of Civil Engineering
National Institute of Technology Karnataka
Surathkal, Mangalore - 575 025, Karnataka, INDIA



ACKNOWLEDGEMENT

It is an immense pleasure to express my heartfelt gratitude to various people who helped and motivated me to carry out the Ph.D. dissertation.

I express my sincere gratitude and thanks to my esteemed Supervisor, **Dr. Arun Kumar Thalla**, Professor, Department of Civil Engineering, for the valuable guidance, suggestion and motivations, which played an inspiring role throughout the research work to fulfil the criteria.

I owe my thanks to **Prof. Subhash C. Yaragal**, Head of the Department, Civil Engineering and **Dr. B. R. Jayalekshmi**, **Dr. K. Swaminathan**, and **Dr. Varghese George**, previous Head of the Department, Civil Engineering, NITK Surathkal, for extending the facilities and wonderful supports in every stage of research work in the Department. I also sincerely thank **Prof. Vidya Shetty**, Academic Dean, NITK Surathkal, for the support rendered throughout the work.

I would like to thank my RPAC committee members, **Dr. Ramesh H and Prof. AU Ravi Shankar**, for their continued support and encouragement. I offer my sincere appreciation for the learning opportunities provided by the RPAC members. Also, I would like to express my heartfelt gratitude to all faculty and staff members Department of Civil Engineering, NITK Surathkal. Their continuous encouragement and support were inspiring towards work.

I would like to express my heartfelt gratitude to all my **friends and colleagues** for their unremitting encouragement, help and support. I am grateful to my **family** members, whose endless encouragement and support were an endless source of inspiration for this work. I thank the almighty for his loveliness upon me throughout my life. Once again, I thank one and all who have helped me directly or indirectly complete my project in time.

NITK Surathkal

Teema Thomas

ABSTRACT

Waste management of both solid and liquid fractions is gaining priority due to urbanisation, industrialisation, and increased resource demand. Agricultural waste, one of the components of solid waste, has huge potential to convert into several by-products. Nutmeg seed shell (NSS) is an agricultural waste obtained from the cultivation of nutmeg (*Myristica Fragrans*) spice that can convert into useful products due to its high calorific value and lignin content. NSS can find applications as in refuse-derived fuel (RDF) in the form of briquettes and adsorbents for wastewater treatment. An in-depth research and development in NSS waste valorisation can find its whole potential in wastewater treatment.

Removal of micropollutants in wastewater is a significant challenge due to their diverse chemical properties. Even after numerous treatment processes, treated water still contains micropollutants, which include hazardous synthetic dyes; this shows the importance of including advanced treatment techniques in wastewater treatment. Thermally modified NSS can be used as an adsorbent for wastewater treatment. The higher phenolic and lignin content in NSS can be utilised to prepare biomass-based catalysts for wastewater treatment.

The current research examines the removal of anionic dye: Remazol Brilliant Blue Reactive (RBBR), cationic: Methyl Violet 10B (MV), and zwitterionic dye: Rhodamine B (RhB), using NSS-based materials to evaluate the removal efficiency of textile wastewater treatment that contains dyes with various ionic states.

Thermally modified NSS (NSS Biochar) was identified with micropores and nanopores, resulting in 93.41% RBBR dye removal, but it was less efficient in the case of other dyes. Due to the presence of reducing and capping agents in NSS aqueous extract, it is used to synthesise silver nanoparticles (AgNPs). The optimised synthesis process resulted in the formation of AgNPs with a size 10–60 nm and a surface area of 88.16 m²/g. The best radical scavenging activity was seen at 200 g/mL for AgNPs. The application of these AgNPs in antibacterial uses is supported by their bacterial inhibition against both gram-positive and gram-negative bacteria (IZD ≥ 15 mm) when

compared to ampicillin (IZD \leq 13 mm) at a concentration of 50 $\mu\text{g/mL}$. Synthesised AgNPs were used to study their feasibility in dye removal, and the results showed a better photocatalytic degradation ($>90\%$) of RhB (10 mg/L), RBBR (100 mg/L), and MV (100 mg/L) when exposed to UV light. According to the degradation process, AgNP's affinity towards dye and their radical action impacts how effectively the dye degrades. The degradation mechanism was found by analysing the degradation products using HRLC-MS. In the presence of AgNP, the fluorescent dye RhB could not degrade at higher concentrations.

The NSS's higher lignin and phenolic content are also utilised to prepare the catalyst for dye degradation. Lignin was extracted from NSS using alkali; the optimal extraction was achieved with 12% sodium hydroxide, resulting in 33% of lignin yield. To separate the catalyst after the treatment process, a composite built on NSS lignin and silver with magnetic property (Ag/Fe/Lignin) is used for dye degradation. Ag/Fe/Lignin resulted in improved degradation for all category dyes, even at higher concentrations. The research was also done on a mixture of cationic, anionic, and zwitterionic dyes. Ag/Fe/Lignin accomplished 94% degradation for a dye mixture at 100 mg/L concentration under UV light. It degraded more quickly and efficiently at greater concentrations when H_2O_2 was added as an activator in the presence of UV light. The processes that degrade dyes into simple organic molecules include deamination, demethylation, dihydroxylation, and cleavage of the aromatic ring by radical action. The degradation efficiency for the reusability study was $>95\%$ even after five cycles of experiments. The dye degradation capacity NSS-based composite (Ag/Fe/Lignin) demonstrated an improved method of utilising lignocellulosic waste components, such as NSS with high lignin content, in wastewater treatment.

Keywords: *Biochar, Silver nanoparticle, Lignin, Magnetised catalyst, Dyes, Degradation*

CONTENTS

ABSTRACT	i
CHAPTER 1	1
INTRODUCTION	1
1.1 General	1
1.2 An overview of agricultural waste	1
1.3 Nutmeg (<i>Myristica fragrans</i>)	2
1.4 Micropollutants	3
1.5 Textile dyes and its impacts	4
1.6 Textile wastewater treatment- Current approaches	5
1.7 Framework of thesis	6
CHAPTER 2	7
LITERATURE REVIEW	7
2.1 General	7
2.2 Nutmeg shell as biomass substrate	7
2.2.1 Antioxidant properties of plant extracts	9
2.2.2 Antimicrobial effect of plant extracts	10
2.2.3 Nanotechnology and nutmeg applications	11
2.2.3.1 Synthesis of nanoparticles-General	15
2.2.4 Agricultural waste: Source of lignin	21
2.3 Micropollutants and their removal	25
2.3.1 Nanoparticles and composites for catalytic treatment of wastewater	29
2.4 Summary of literature review	30
2.5 Objectives	31
CHAPTER 3	33
MATERIALS AND METHODOLOGY	33
3.1 General	33
3.2 Materials	33
3.2.1 NSS collection and pre-processing	33
3.2.2 Chemicals	33
3.3 Overall workflow	35

3.4	NSS biochar as an adsorbent for the removal of dyes	35
3.4.1	NSS biochar preparation	35
3.4.2	Biochar yield	37
3.4.3	Adsorption	37
3.4.4	Adsorption isotherms	37
3.4.5	Adsorption kinetics	38
3.4.6	Thermodynamic studies	39
3.5	Synthesis of AgNPs using NSS extract and evaluation of its potential as a catalyst for dye degradation	39
3.5.1	Preparation of NSS aqueous extract	39
3.5.2	Phytochemical analysis of NSS extract	40
3.5.3	Green synthesis of AgNPs	41
3.5.4	Characterisation of AgNPs	41
3.5.5	Antioxidant activity of AgNPs	43
3.5.6	Antibacterial activity of AgNPs	44
3.5.7	Photocatalytic degradation of dyes using synthesised AgNPs	44
3.5.8	Isotherm study for degradation of dyes	45
3.5.9	Kinetic study for degradation of dyes	46
3.5.10	Dye degradation pathway studies	46
3.6	Utilisation of NSS lignin-based catalyst for dye degradation	46
3.6.1	Preparation of alkali-soluble lignin-based catalysts	46
3.6.1.1	Preparation of alkali-soluble lignin	46
3.6.1.2	Preparation of magnetic iron oxide nanoparticles (Fe_3O_4)	47
3.6.1.3	Preparation of magnetised lignin (Fe/Lignin)	47
3.6.1.4	Preparation of silver-coated lignin (Ag/Lignin)	47
3.6.1.5	Preparation of magnetised silver-lignin composite (Ag/Fe/Lignin)	47
3.6.2	Characterisation of composites	47
3.6.3	Preparation of dye solutions	48
3.6.4	Photocatalytic degradation of dyes using catalysts	48
3.6.5	Kinetic study and isotherm study for degradation of dyes using Ag/Fe/Lignin composite	49

3.6.6	Reusability study for Ag/Fe/Lignin composite	49
CHAPTER 4		
RESULTS AND DISCUSSIONS		51
4.1	General	51
4.2	Characterisation of biomass	51
4.3	NSS biochar as an adsorbent for the removal of dyes	52
4.3.1	NSS biochar as an adsorbent for the removal of RBBR dye	53
4.3.2	Characterisation of NSS and NSS biochar	53
4.3.3	Response surface methodology-based optimisation of RBBR dye removal using NSS biochar	58
4.3.3.1	Analysis of variance for RBBR dye removal	59
4.3.3.2	Effect of independent variables on adsorption	61
4.3.4	Adsorption isotherm for RBBR dye removal using NSS biochar	64
4.3.5	Adsorption kinetics for RBBR dye removal using NSS biochar	65
4.3.6	Thermodynamic study for RBBR dye removal using NSS biochar	67
4.3.7	Performance evaluation of NSS biochar as an adsorbent for the removal of dyes	68
4.4	Synthesis of AgNPs using NSS extract: its characterisation and application in photocatalysis-based dye removal	70
4.4.1	Characterisation of NSS aqueous extract	70
4.4.2	Synthesis of AgNPs	70
4.4.3	Characterisation of AgNPs	72
4.4.3.1	Antioxidant activity of AgNPs	76
4.4.3.2	Antibacterial properties of AgNPs	77
4.4.4	Preliminary studies on dye degradation	78
4.4.5	Photocatalytic degradation of dyes- Optimisation of parameters	79
4.4.5.1	Kinetic study for RhB, RBBR and MV dye	84
4.4.5.2	Isotherm study for RhB, RBBR and MV dye	86
4.4.6	Degradation mechanism	88
4.4.7	By-products of photocatalytic dye degradation using AgNPs	88
4.5	Utilisation of Ag/Fe/Lignin composite for dye degradation	94

4.5.1 Lignin extraction and characterisation	94
4.5.2 Synthesis and characterisation of Ag/Fe/Lignin	96
4.5.3 Photocatalytic degradation of dyes using Ag/Fe/Lignin	104
4.5.4 Photocatalytic degradation of a mixture of dyes using Ag/Fe/Lignin	106
4.5.5 Effect of H ₂ O ₂ on degradation of a mixture of dyes	108
4.5.6 Kinetic and isotherm study for removal of a mixture of dyes	109
4.5.7 Mechanism of dye degradation using Ag/Fe/Lignin composite	113
4.5.8 Reusability study for Ag/Fe/Lignin composite used in dye degradation	116
4.5.9 Comparison with other photocatalytic studies conducted for the degradation of dyes	117
4.6 Summary	119
CHAPTER 5	121
CONCLUSIONS	121
REFERENCES	125
APPENDICES	150
PUBLICATIONS	153

LIST OF FIGURES

Figure 1.1	(a) Nutmeg b) Diagram showing the seed in a cross-section of nutmeg fruit (Singh et al. 2015)	3
Figure 2.1	Synthesis of nanoparticles	16
Figure 2.2	Mechanism of nanoparticle synthesis using a reducing and capping agent	17
Figure 2.3	Characterisation of nanoparticles	20
Figure 2.4	a) Structure of lignin b) Coniferyl alcohol c) P-coumaryl alcohol and d) Sinapyl	21
Figure 3.1	Experimental flowchart for present project work	35
Figure 3.2	Photocatalytic experimental setup	45
Figure 3.3	Photocatalytic experimental setup used for Ag/Fe/Lignin as the catalyst	49
Figure 4.1	a) Dried NSS b) FESEM image of dried (105°C) NSS powder c) NSS powder with 200 K magnification, d) FESEM image for NSS biochar e) NSS biochar with micropores (2 K magnification) f) NSS biochar with nanopores (10 K magnification) g) NSS biochar after adsorption	54
Figure 4.2	DTG and TGA curve for a) NSS and b) NSS biochar	55
Figure 4.3	XRD pattern for a) NSS b) NSS biochar c) NSS biochar after adsorption	56
Figure 4.4	FTIR spectra of a) NSS b) NSS biochar c) NSS biochar after adsorption	57
Figure 4.5	Graphs of a) Actual and predicted values b) Normal probability of the residuals	61
Figure 4.6	3D and contour plots of a) AB interactions on RBBR removal b) DB interactions on RBBR removal	63
Figure 4.7	a) Adsorption isotherm of RBBR onto NSS biochar b) Langmuir adsorption isotherm model c) Freundlich adsorption isotherm model d) Temkin adsorption isotherm model	64

Figure 4.8	Kinetic plots of a) adsorption kinetics b) Pseudo-first-order model c) Pseudo-second-order model d) Intraparticle diffusion model e) Elovich kinetic model	66
Figure 4.9	Von't Hoff plot for thermodynamic studies	68
Figure 4.10	The effect of a) time b) pH c) Dosage and d) Initial dye concentration on RhB dye, RBBR dye and MV dye degradation	69
Figure 4.11	AgNPs synthesis using NSS extract: a) NSS extract, b) silver nitrate solution c) Colour change due to the formation of nanoparticles d) UV visible spectrum for AgNPs and NSS extract e) Effect of amount of extract f) Effect of concentration silver nitrate solution, g) Effect of pH h) Effect of contact time	72
Figure 4.12	a) SAXS curve for an aqueous solution of AgNPs b) Particle size distribution c) XRD pattern for dried AgNPs d) FTIR e) DTG and TGA curve f) N ₂ adsorption/desorption isotherm plot and pore size distribution g) FESEM image h) Zeta potential analysis	74
Figure 4.13	Antioxidant activity of AgNPs: a) DPPH free radical scavenging activity b) Hydroxyl radical-scavenging activity, Antibacterial activity of AgNPs against pathogenic microorganisms: c) <i>E. coli rosetta</i> (RDS) d) <i>Pseudomonas aeruginosa</i> (PA) e) <i>Bacillus subtilis</i> (BS) f) <i>Bacillus haynesii</i> (BH) (1. AgNPs: 50 µg/mL, 2. AgNPs: 25 µg/mL, 3. NSS aqueous extract 4. Ampicillin 50 µg/mL, 5. Silver nitrate)	77
Figure 4.14	Dye removal using AgNPs under different light sources	79
Figure 4.15	The effect of a) time b) pH c) adsorbent dose and d) Initial dye concentration on RhB dye, RBBR dye and MV dye degradation	82
Figure 4.16	a) Adsorption kinetics b) Pseudo-first-order kinetic model c) Pseudo-second-order kinetic model d) Interparticle diffusion	85

	kinetic model e) Elovich kinetic model for degradation of RhB dye, RBBR dye and MV dye	
Figure 4.17	The plots of a) Adsorption isotherm b) Langmuir isotherm c) Freundlich isotherm d) Temkin isotherm of RhB dye, RBBR dye and MV dye	86
Figure 4.18	Degradation mechanism of dyes using AgNPs	88
Figure 4.19	Possible degradation pathway of a) RhB dye b) RBBR dye c) MV dye based on HRLC-MS analysis	90
Figure 4.20	Alkali lignin obtained from NSS	94
Figure 4.21	¹ H NMR spectra for a) Commercially available alkali lignin and b) alkali lignin extracted from NSS	95
Figure 4.22	SEM images of a) 25 K b) 50 K c) 100 K magnification, elemental mapping images of Ag/Fe/Lignin: d) Carbon e) Oxygen f) Nitrogen g) Sodium h) Iron i) Silver and j) EDX spectrum	96
Figure 4.23	FTIR results for a) NSS b) AgNPs c) Lignin d) Fe/Lignin e) Ag/Fe/Lignin	98
Figure 4.24	XRD analysis for a) NSS b) Lignin c) AgNPs d) Fe ₃ O ₄ e) Ag/Lignin f) Fe/Lignin g) Ag/Fe/Lignin	99
Figure 4.25	Raman spectra for a) Lignin b) AgNPs c) Ag/Lignin d) Fe ₃ O ₄ e) Fe/Lignin f) Ag/Fe/Lignin	100
Figure 4.26	a) N ₂ adsorption/desorption isotherm plot and pore size distribution for Ag/Fe/Lignin b) VSM spectra for Ag/Fe/Lignin and Fe ₃ O ₄ c) PL spectra for AgNPs, Ag/Lignin and Ag/Fe/Lignin d) TGA graph analysis for Ag/Fe/Lignin	101
Figure 4.27	Zero-point charge of Ag/Fe/Lignin	103
Figure 4.28	Effect of pH for a) MV dye b) RhB dye c) RBBR dye degradation Effect of d) time e) concentration f) dosage on dye degradation using Ag/Fe/Lignin	105
Figure 4.29	Effect of a) pH b) time c) concentration d) dosage on the degradation of the mixture of dyes using Ag/Fe/Lignin	107

Figure 4.30	a) UV-visible spectra for the mixture of dyes degradation using Ag/Fe/Lignin b) UV-visible spectra for the mixture of dyes degradation using Ag/Fe/Lignin with H ₂ O ₂ c) Effect of time for degradation of the mixture of dyes d) Effect of initial concentration for degradation of the mixture (catalyst and H ₂ O ₂)	109
Figure 4.31	The plots of a) Adsorption isotherm b) Langmuir isotherm c) Freundlich isotherm d) Temkin isotherm of the mixture of dyes with and without H ₂ O ₂	110
Figure 4.32	a) Adsorption kinetics b) Pseudo-first-order kinetic model c) Pseudo-second-order kinetic model d) Interparticle diffusion kinetic model e) Elovich kinetic model for degradation of a mixture of dyes with and without H ₂ O ₂	111
Figure 4.33	Schematic representation of possible degradation mechanism of dyes	114
Figure 4.34	Pathway mechanism for the degradation of the mixture of dyes using Ag/Fe/Lignin	115
Figure 4.35	Reusability study of Ag/Fe/Lignin for degradation of the mixture of dyes	117

List of tables

Table 2.1 Total phenolic content of the 80% methanol extracts of different parts of <i>Myristica fragrans</i> (Sulaiman and Ooi 2012)	8
Table 2.2 Catalyst synthesis using plant extractives	10
Table 2.3 Nanoparticle synthesis using nutmeg extracts	12
Table 2.4 Nutmeg extracts used for AgNPs synthesis	19
Table 3.1 Physical and chemical properties of dyes used in the study	34
Table 3.2 Biomass characterisation and techniques	36
Table 3.3 Characterisation and techniques	42
Table 4.1 Quantitative analysis of solids in NSS	52
Table 4.2 Biomass composition of NSS	52
Table 4.3 FTIR spectra bands for NSS, NSS biochar and NSS biochar after adsorption	57
Table 4.4 The experimental data for RBBR dye removal	58
Table 4.5 ANOVA table for RBBR dye removal	60
Table 4.6 Parameters of the isotherm models for RBBR dye adsorption onto NSS biochar	65
Table 4.7 RL values for adsorption of RBBR on NSS biochar based on the Langmuir model	65
Table 4.8 Parameter values of kinetic models	67
Table 4.9 Thermodynamic parameters for RBBR dye adsorption on NSS biochar	68
Table 4.10 Phytochemical analysis of NSS extract	70
Table 4.11 Inhibition zone diameter for AgNPs against bacterial strains	78
Table 4.12 Preliminary study on degradation efficiency of dyes	80
Table 4.13 Parameters of kinetic and isotherm study for RhB, RBBR and MV dyes	87
Table 4.14 AgNP synthesis from Nutmeg	91

Table 4.15 Synthesis of AgNPs using various plant extracts and their dye degradation efficiency	93
Table 4.16 Lignin yield from NSS	94
Table 4.17 Lignin yield with different concentrations of sodium hydroxide	95
Table 4.18 Parameters of kinetic and isotherm study for the mixture of dyes with and without H ₂ O ₂	112
Table 4.19 Comparative study with other lignin based photocatalysts	118

ABBREVIATIONS

Ag/Fe/Lignin	Magnetised silver-lignin composite
Ag/Lignin	Silver-lignin composite
AgNPs	Silver nanoparticle
ANOVA	Analysis of variance
ASTM	American Society for Testing and Materials
BBD	Box-Behnken Design
BET	Brunauer, Emmett and Teller
BH	<i>Bacillus haynesii</i>
BS	<i>Bacillus subtilis</i>
CDMR	Ceramic Discharge Metal halide Reflector bulb
DPPH	2,2-diphenyl-1-picrylhydrazyl
DTG	Differential thermogravimetry
EDX	Energy-dispersive X-ray spectroscopy
Fe/Lignin	Lignin with magnetic property
FESEM	Field Emission Scanning Electron Microscope
FTIR	Fourier Transformation Infra-Red Spectrophotometer
GAE	Gallic Acid Equivalent
GC-MS	Gas Chromatography–Mass Spectrometry
HRLC-MS	High Resolution performance Liquid Chromatography- Mass Spectrometer
IUPAC	International Union of Pure and Applied Chemistry
IZD	Inhibition Zone Diameter
JCPDS	Joint Committee on Powder Diffraction Standards
LED	Light Emitting Diode
MBC	Minimum Bactericidal Concentration
MIC	Minimum Inhibitory Concentration
Ms	Saturation Magnetisation
MSW	Municipal Solid Waste
MV	Methyl Violet 10B
NMR	Nuclear Magnetic Resonance

NREL	National Renewable Energy Laboratory
NSS	Nutmeg seed shell
PA	<i>Pseudomonas aeruginosa</i>
pH _{ZPC}	Zero point of charge
PL	Photoluminescence
RBBR	Remazol Brilliant Blue Reactive
RDF	Refuse-Derived Fuel
RhB	Rhodamine B
ROS	Reactive Oxygen Species
RSM	Response Surface Methodology
RSS	Residual Sum of Squares
SAXS	Small-Angle X-ray Scattering
TAPPI	Technical Association of Pulp and Paper Industry
TEM	Transmission Electron Microscopy
TGA	Thermo Gravimetric Analyzer
TPC	Total Phenolic Content
VSM	Vibrating Sample Magnetometer
XRD	X-ray diffraction

CHAPTER 1

INTRODUCTION

1.1 General

Municipal solid waste (MSW) is produced in enormous quantities worldwide due to urbanisation and change in lifestyle; hence proper waste management is a stinging and widespread issue to maintain a healthy and hygienic environment. Solid waste may include electrical and electronic waste, hazardous waste (paints, spray, and chemicals), agricultural waste, and medical waste (Niazi et al. 2016). Globally, around 1.5 billion tonnes/year of MSW has been produced in recent years, and its generation is predicted to increase up to 2.5 billion tonnes/year by 2025 (Hoorweg and Bhada-Tata 2012). Agricultural waste is a low-cost material that has the potential for various eco-friendly applications (Ikram et al. 2021; Zhao et al. 2021). Agricultural waste is used extensively in preparing low-cost sorbents, which finds its application in contaminated water remediation (Memon, 2014) and air purification. However, the utilisation rate of agricultural waste is less than 30% (Uma et al. 2020).

1.2 An overview of agricultural waste

Agricultural waste contributes to a significant proportion of total solid waste. Globally 998 million tonnes/year of agricultural waste are produced, which has a huge economic value, contributing to around 1.2 billion tonnes of oil equivalent, approximately 15% of the world's energy consumption (Obi et al. 2016).

Globally, lignocellulosic feedstock, including agricultural waste, is rich in cellulose, hemicellulose, and lignin sources. Biomass is organic material that comes from plants and animals. Agricultural residues are one such biomass waste which is underutilized. A complete valorisation of such biomass waste can be done instead of discarding them. Replacing harmful chemicals with the agricultural residue-based products is an excellent option of environmental friendly approach leading to sustainability (Le et al. 2021; Soleimani and Kaghazchi 2007). Applications of agricultural waste include compost preparation, briquette production (a form of refuse-derived fuel), animal fodder, biogas production, aggregates/binding materials in the

construction field etc. (Salah and El-Haggar 2007). Development and use of rich biomass resources are strongly recommended for rectifying environmental and energy concerns (Srisasiwimon et al. 2018). Cellulose and hemicellulose have applications in different fields, but lignin is not used much and is still being developed continuously to be beneficial (Chen et al. 2016). Agricultural wastes, like coconut shells, mango chestnut shells, and nutmeg shells (endocarp of biomass), have a non-edible high-lignin content, not of use for livestock feed (Mendu et al. 2012). This agro-waste has been investigated as a potential alternative to preparing the low-cost adsorbent for contaminated water remediation (Memon 2014).

1.3 Nutmeg (*Myristica fragrans*)

Nutmeg belongs to the family of *Myristicaceae* with a natural origin in the Moluccas; however, its major cultivation is seen in Indonesia, Malaysia, Sri Lanka, the West Indies, the southern part of India, and in the island of Zanzibar (Widelski 2017). In India, it is mainly cultivated in the South region, particularly in Kerala, Andhra Pradesh and northeastern India. In 2022, India produced 15384 tonnes spread over 24080 hectares (Spices Board, 2022). Out of this, 14589 tonnes are cultivated in Kerala. The fruit is a one-seeded fleshy drupe, yellow in colour with a pleasing aroma in nature and pear-shaped (figure 1.1). The orange pericarp splits during fruit ripening, disclosing the black seed surrounded by a red coloured net-like aril(mace), which is separated, dried, and processed for future application. Nutmeg contains 30- 40% of fats and about 10% of essential oils. Nutmeg seed shell (NSS) is the major waste content generated during the production of high-valued nutmeg seeds and nutmeg mace (Rema and Krishnamoorthy 2012)

Nutmeg shells are mainly used for drying fish, making tiles and briquettes, and converting as adsorbents for various uses (Activated carbon) (Akpor et al. 2013; Suryaningsih et al. 2017; Syahiddin and Muslim 2018). Studies including modified adsorbents are also trending since it has possibilities to improve the surface characteristics of adsorbents due to the presence of metal nanoparticles or chemical modifications (Thakur et al. 2017). Ssynthesised nanoparticles using plant extracts are considered strong antioxidants, antimicrobial material and catalysts for the degradation of pollutants in wastewater (John 2019).

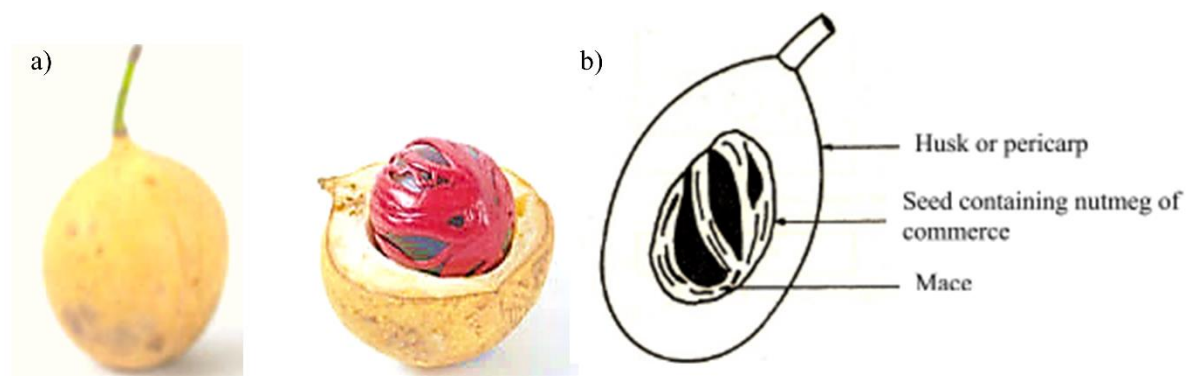


Figure 1.1 (a) Nutmeg b) Diagram showing the seed in a cross-section of nutmeg fruit (Singh et al. 2015)

Lignin in lignocellulosic biomass has increased adsorption capacity (Idris et al. 2018). The higher amount of lignin in the NSS can be used to synthesise nutmeg shell-based sorbents for wastewater treatment. Coir fibres, among other biomass feedstocks, have been shown to possess 59.4 weight per cent of the lignin. Lignin is also a by-product of industrial processes such as acid hydrolysis, kraft, sulphite, soda, organosolv, and hydrothermal and acid hydrolysis processes, for lignin that is of commercial quality, prepared by the kraft process. Industrial lignin is a by-product obtained from the paper and pulp industry and is produced in quantities of 1.5 and 1.8 billion tonnes annually. The kraft process generates 130 million tonnes of lignin annually. As a part of lignin valorisation, researchers now utilise it to enhance the mechanical properties of biopolymers by using it as a reinforcement (Mariana et al. 2021a). Much research has not been devoted to lignin and its oxidative, reductive, and redox-neutral reactions to degrading wastewater pollutants. Studies on lignin and lignin-based composites are also progressing due to their high potential for better removal of contaminants from wastewater.

1.4 Micropollutants

Micropollutants are chemicals in the environment in small quantities yet potentially harm living things, including humans. Their stability, bioaccumulation, and toxicity serve as typical identifiers. Micropollutants include both synthetic and natural compounds, emerging contaminants, pharmaceuticals, steroid hormones, dyes, personal care products, and chemical fertilisers (Atas et al. 2017; Stamm et al. 2016). Textile dyes are also considered micropollutants in the environment due to the

enhanced demand and toxicity (Hoerger et al. 2009). Studies have stated that micropollutants in water cause chronic health effects on organisms (Quesada et al. 2019). So, efficient removal of these pollutants is essential for a clean environment and good health conditions. Adsorption with different adsorbents, Fenton oxidation, and membrane filtration are the conventional methods used to treat micropollutants in water. Real-time wastewater treatment should be done to manage wastewater effectively.

1.5 Textile dyes and its impacts

Micropollutants, especially textile dyes, are more evidently focused due to their toxicity. Pollution caused by the coloured wastewater discharged from textile, paper, leather industries etc., cause environmental toxicity even at lower concentration levels. Globally more than 0.7 million tonnes/annum of dyes produced with 1000 varieties of dyes resulted in more complex organic and inorganic pollutants in the water matrix (Atas et al. 2017; Budnyak et al. 2021). India and China are the two largest dye suppliers worldwide. China and India also export huge quantities of raw materials and chemicals required for dye manufacturing (Chemical Economics Handbook 2021). Textile dyes are almost non-biodegradable and more stable in structure (Suteu et al. 2010). The treated effluents from wastewater treatment plants that discharge into the aquatic environment still include synthetic organic dyes. An Indian case study revealed that farmers who lived close to the impacted farmlands experienced sickness symptoms, including joint discomfort or grey hair as a result of the long-term (20 years) use of water containing dyes to irrigate crops. (Tkaczyk et al. 2020). Dyes do not adhere completely to the cloth/fabrics/material firmly; they can be released into the water as effluent in amounts ranging from less in the case of (2%) basic dyes to as high as half the amount for reactive dyes (Sharma et al. 2021). Due to the continued uncontrolled release of textile dyes into the environment and their persistence, there is an increased risk to aquatic flora, a decline in water quality, including turbidity colour, odour and eutrophication, and an increase in the content of carcinogenic products in the water matrix. Textile industrial waste containing synthetic dyes influences environmental toxicity and human health negatively. Aromatic compounds in dyes result in health issues like skin diseases, allergies and even carcinogenic effects in the

human body (Suteu et al. 2010). Conventional wastewater treatment plant usually does not remove these pollutants (Zhang et al. 2017). Adsorption is the easiest and best method for reactive dye removal (Lai 2021), among several physical, chemical and aerobic/anaerobic biological methods (Bhatia et al. 2017).

1.6 Textile wastewater treatment- Current approaches

Activated carbon is mainly utilised for wastewater treatment in the textile sector (Raj et al. 2021). Adsorbent, synthesised from bio-waste (Mariana et al. 2021b), minimise the raw material cost and thus reduces the expense of contaminant removal from wastewater (Corral-Bobadilla et al. 2021). But these methods don't completely degrade the dyes from wastewater due to their complex structure (Budnyak et al. 2021).

Nanoparticles have greater importance due to their large surface area, highly reactive nature, etc. Physical, chemical and biological methods can do nanoparticle synthesis. Biogenic nanoparticle possesses more enhanced properties than chemically or mechanically derived nanoparticles due to their cytotoxic activity, antioxidant, photocatalytic activity, and biocompatibility so that they can be applied in water treatment and even medical applications (Chung et al. 2017). Due to the higher energy consumption and health issues caused by physical and chemical methods, it is not promoted for the synthesis of nanoparticles. Biological synthesis can be done by Bacteria, yeast, fungi, algae, plant extractives, etc., which are more effective due to their reducing capacity (antioxidant property). The biological process reduces process toxicity, and the conditions maintained for the biological process are comparatively normal environmental conditions, so it will reduce the process's complexity. As a result of new research, dyes are also removed using polymer composites with higher adsorption capacity than other composites (El-Shamy 2022). But the processing and further degradation of these polymer composites create environmental issues. In this context, the removal of dye, especially the cationic and anionic dyes from its aqueous solution by biochar prepared from biomass, nanoparticles synthesised with biomass extracts and lignin-based adsorbents from biomass promote the conversion of biowaste to useful products for wastewater treatment.

1.7 Framework of thesis

The thesis includes a study carried out regarding the research objectives. A brief skeletal structure of the thesis is given below.

Chapter 1 gives a general introduction and discusses the objectives and outline of the thesis.

Chapter 2 includes the literature reviews on NSS, application of nanoparticles in wastewater treatment, the presence of lignin, and textile wastewater treatment.

Chapter 3 includes the materials and methods used for the experimental studies on synthesis, characterisation of adsorbents and catalysts and their utilisation in adsorption/photocatalytic degradation of dyes

Chapter 4 describes the results and discussion on

- (a) Dye removal using NSS-based biochar
- (b) Nanoparticle synthesis and photocatalytic degradation of dyes
- (c) Synthesis of lignin-based composite and photocatalytic degradation of dyes

Chapter 5 outlines the conclusions obtained and possible future scope.

CHAPTER 2

LITERATURE SURVEY

2.1 General

Massive waste production and overuse of natural resources have prompted research on efficient waste management. Solid waste conversion to value-added products is getting more relevant due to the possibility of waste reduction and reusing it for different purposes, especially in wastewater treatment (Mariana et al. 2021b).

2.2 Nutmeg shell as biomass substrate

Nutmeg is a spice having high medicinal value, regularly cultivated in Southern India, which is used for flavouring, therapeutic applications and even as a preservative (Sulaiman and Ooi 2012a). All the parts of nutmeg contain almost similar components but different concentrations (Rema and Krishnamoorthy 2012). Seed and mace are the main parts that are used for the main applications, and nutmeg pericarp is used in making pickles and juice, also used in medical applications (Sulaiman and Ooi 2012b). Leaves of nutmeg are used in medical applications because of their antioxidant property.

Nutmeg seed shell is primarily used for drying fish and other biomasses, briquette making, and to date, it is utilized as an adsorbent by thermal modification (Akpor et al. 2013; Idris et al. 2018). NSS have a high calorific value of up to 4471.26 cal/g. The lignin content in the NSS is (43- 51%), higher compared with cellulose (14-18%) and hemicellulose (22-26%) (Idris et al. 2018). Carbonated forms of nutmeg shell resulted in efficient removal of nitrate from aqueous solution. Chemical modifications of the shell do not improve the efficiency of phosphate removal (Akpor et al. 2013). Syahiddin and Muslim, (2018) studied the adsorption of Cu (II) ions onto *Myristica fragrans* shell-activated carbon in batch mode with chemical activation using NaOH, and its best concentration to activate was 0.5 M. Based on BET analysis, it resulted in the total surface area and pore volume of 99.85 m²/g and 0.086 cm³/g, respectively. The maximum adsorption capacity obtained was 107.65mg/g based on the pseudo-

first-order of adsorption kinetics. NSS contains 35.25% of the total weight of its nutmeg seed, including the shell. It is a raw material that used to make charcoal briquettes. The pyrolysis process will proceed more quickly as the temperature rises, producing more gases and liquids while producing less solids (Idris et al., 2017). Salindeho et al. (2014) assessed the effect of different smoke sources on skipjack tuna (*Katsuwonus pelamis*). The results showed the high protein content (38.95%) and lowest fat content (2.13%) in the nutmeg shell smoked skipjack fish and had the highest polyunsaturated acid content which is different from that obtained from other smoking sources.

The total phenolic content and antioxidant properties of nutmeg parts are discussed more due to their medicinal value and their applicability as a reducing agent. The total phenolic content of nutmeg parts is in the order of pericarp < leaf < seed kernel < mace < shell (Table 2.1). But the extraction yields less for NSS as compared to the other parts of nutmeg (Sulaiman and Ooi 2012b).

Table 2.1 Total phenolic content of the 80% methanol extracts of different parts of *Myristica fragrans* (Sulaiman and Ooi 2012)

Sample	Total phenolic content (mg GAE/g extract)
Leaf	6.8±0.2
Pericarp	2.3±0.2
Aril	48.2±1.2
Seed kernel	46.3±0.6
shell	48.9±4.2

Phenolic compounds in plant extractives will enhance the possibility of metal nanoparticle synthesis from its metal salts. Phenolic compounds from the lignans group have properties such as chelating with metallic elements to form complex compounds. The presence of phenols and proteins may act as reducing and stabilising agents for silver nanoparticle (AgNPs) (Sharma et al. 2014). Metal chelating capacity enables nutmeg leaves and pericarps to reduce metal oxides to their nano size. Phytochemical compounds responsible for their potential as antioxidants, antimicrobial, anti-diabetic

and anti-inflammatory properties are present in nutmeg seed and mace. These contents are also in lower concentrations in nutmeg leaf and pericarp.

2.2.1 Antioxidant properties of plant extracts

The antioxidant property of plant extractives is due to the presence of reducing agents present in them. Strong antioxidant activity is a characteristic of plant extractives. Free radicals can be scavenged and neutralised by them in the body. Free radicals are very reactive chemicals that may harm cells and induce oxidative stress, which can result in a number of illnesses and ageing. By stopping the harm done by free radicals, antioxidants help against oxidative stress. Plant extractives' antioxidant properties are due to their unique chemical makeup, which enables them to stabilise and neutralise free radicals by donating electrons or hydrogen atoms (Motelica et al. 2020). Pharmaceuticals, nutraceuticals, and functional foods can employ plant extractives with antioxidant qualities to promote health and resist illnesses caused by oxidative stress. They can boost cardiovascular health, improve immunological function, reduce inflammation, and guard against age-related illnesses. Additionally, nanoparticle-based medicine delivery systems and bioimaging agents can be created by using the capping capabilities of plant extractives (Aziz et al. 2018). Plant extracts with antioxidant qualities are frequently used as natural antioxidants in cosmetic compositions. They aid in defending the skin from deterioration brought on by UV rays, pollution, and other environmental stresses. By serving as natural preservatives, these substances can also improve the stability and shelf-life of cosmetic items (Velsankar et al. 2020a).

The reduction capacity of plant extracts is utilised for the synthesis of different types of catalysts for wastewater treatment and different types of medical applications. Plant extractives can serve as capping agents (agents which help to stabilize the particle size at the nano level) during the production of nanoparticles, which is essential for regulating the particles' size, stability, and dispersibility. Nanoparticles are more stable and less likely to aggregate when capping agents adhere to their surface. Functional groups found in plant extractives, such as hydroxyl (-OH), carboxyl (-COOH), and amino (-NH₂) groups, can attach to metal nanoparticles and form a shield around them. This capping layer gives the emerging nanomaterials special qualities and utility in

addition to stabilising the nanoparticles (Rao et al. 2020). The use of plant extractives as environmentally friendly and long-lasting metal nanoparticle synthesisers has gained popularity. The manufacture of stable and useful nanoparticles for a variety of applications is made possible by their antioxidant and capping characteristics. The resultant nanoparticles are employed in various industries, including catalysis, sensing, energy storage, and environmental remediation. Some of the catalysts synthesised using plant extracts are listed in Table 2.2.

Table 2.2 Catalyst synthesis using plant extractives

Product	Reducing agent	Reference
NiFe ₂ O ₄	Onion extract	(Stratil et al. 2006)
Antimicrobial agent	Pereskia bleo	(Johari and Khong 2019)
gold-based catalysts	wood extractive	(Bogdanchikova et al. 2019)
photocatalytic activity of Fe nanoparticle	Ageratum conyzoides extracts	(Shigwenya et al. 2019)
cytotoxic copper nanoparticle	Eclipta prostrata leaves extract	(Chung et al. 2017)

2.2.2 Antimicrobial effect of plant extracts

Plant extracts have the capacity to inhibit the growth of microbes. The amino acids, polyphenolic content, saccharides, polyols, fatty acids, and dicarboxylic acids etc. were probable causes for the observed bioactivities of plant extracts, which can be identified by GC-MS will impart antimicrobial effect which will help to use in medical applications like bandages, medicines, covering materials etc. (Stagos 2020). Numerous plant extracts have antibacterial qualities that can stop microbes from multiplying. When fighting dangerous microorganisms and halting the development of infectious illnesses, this can be very crucial. Some plant extracts have demonstrated effectiveness against antibiotic-resistant bacteria, making them potential alternatives or adjuncts to conventional antibiotics.

Plant extracts have antimicrobial properties to inhibit the growth of bacteria, fungi, and algae (Dipankar and Murugan 2012). Minimum bactericidal concentration (MBC), minimum inhibitory concentration (MIC), and inhibition zone diameter are

measured for microbes to determine microbial concentration up to which the specific extract will inhibit the growth of microbes.

2.2.3 Nanotechnology and nutmeg applications

Phenolic compounds in plant extractives will enhance the possibility of metal nanoparticle synthesis from its metal salts. NSS extract has a higher total phenolic content (TPC). The presence of phenols and proteins may act as reducing and stabilising agents for AgNPs (Sharma et al. 2014). The metal chelating capacity of nutmeg leaves and pericarp can be utilised for nanoparticle synthesis.

Myristica fragrans essential oil was encapsulated into a chitosan nano-matrix, and their characterization and determination of antimicrobial activity and inhibition potential for the effect of aflatoxin were analysed (Das et al. 2020). Nutmeg as a reinforcement to increase mechanical strength and antimicrobial behaviour is getting more importance due to more trending needs in medical applications and material preserving processes. Polyurethane forms with nutmeg seed reinforcement show antimicrobial behaviour against both gram-positive and gram-negative bacteria (Członka et al. 2020). The reinforcement of polyurethane nutmeg composite is confirmed with its enhanced thermal, mechanical, antimicrobial, and anti-ageing properties, enabling use in medical applications and material-preserving processes.

Nutmeg is applied as a biocomposite in antimicrobial applications, showing better performance against dental infections. Hydroxyapatite nanoparticles and a polymer combined with nutmeg essential oil are used to prepare dental bio-composite due to its low colony-forming unit in biofilm (Rohini and Ramachandran 2020). The anti-oxidant property of nutmeg seed extract is utilized to reduce the radical effect in case of dental infections. This composite resulted in better antimicrobial properties against *Lactobacillus* spp., *Streptococcus mutants*, and *Enterococci*. The secondary metabolites like alkaloids, tannins, phenols, carbohydrates, saponins, flavonoids, and terpenoids contribute to antimicrobial and anti-oxidant properties for nutmeg extracts. The contents of these metabolites will vary with the extraction conditions and different parts of nutmeg (Izah et al. 2016). Nutmeg extracts used for nanoparticle synthesis are listed in Table 2.3.

Table 2.3 Nanoparticle synthesis using nutmeg extracts

Material	Nanoparticle	Size of nanoparticle	Method	Application	Reference
Dried nutmeg seed	TiO ₂ nanoparticle	24.58 nm	Biogenic nanoparticle synthesis using water extract.	Photocatalytic degradation of dye, antibacterial activity	(Sagadevan et al. 2021)
Nutmeg fruit	ZnO-nanoparticles	41.23 nm	Nanoparticle green synthesised using extracts of nutmeg fruits	Reducing, capping, and stabilizing agents	(Faisal et al. 2021)
Myristica fragrans Houtt dried leaves	Gd ₂ O ₃ nanoparticles	40 nm	Biogenic nanoparticle synthesis using hexane extract.	Photodegradation activity of malachite green	(Eprasatya et al. 2020)
Myristica fragrans seed	AgNPs	-	Nutmeg aqueous seed extract biosynthesized AgNPs	Antiquorum sensing and antibiofilm potential	(Balakrishnan et al. 2017)
Grounded dried nutmeg fruit's pericarp	Silver and copper oxide nanoparticles	13 ±0.63 nm	Green synthesis using an aqueous extract of grounded dried nutmeg fruit's pericarp	Antimicrobial and catalytic applications	(Sasidharan et al. 2020)
Dried nutmeg seed powder	Fe ₃ O ₄ -MgO nanoparticles	10–15 nm	Nanoparticle green synthesised using ethanol/methanol extracted nutmeg	Antibacterial and anti-fungal performance	(Mojtaba et al. 2019)
Fresh nutmeg fruit aqueous extract	Gold Nanoparticle	-	Biogenic nanoparticle synthesis using aqueous extract.	Environment, biotechnological and biomedical field	(John 2019)

Myristica fragrans (Nutmeg) oil	AgNPs	33.2 - 39.7 nm	Green approach synthesis of AgNPs using an equal amount of nutmeg oil to 1mM silver nitrate	Antimicrobial and anti-fungal agent	(Pauline et al. 2019)
Nutmeg leaves	Nutmeg leaf ester capped -zinc oxide nanoparticle	48.32 ± 2.5 nm	Green synthesis using an aqueous extract of green leaves of <i>M. fragrans</i>	Antibacterial and ant biofilm activities in clinical isolates	(Cherian et al. 2019)
Nutmeg oleoresin	AgNPs	spherical-shaped, 20–50 nm	Biogenic nanoparticle synthesis using nutmeg oleoresin	Antibacterial, cytotoxicity, drug delivery, and biosensor applications	(Madhumithaa et al. 2019)
Dried nutmeg seed powder	AgNPs	25 nm	Biogenic nanoparticle synthesis using water-extracted nutmeg seed (15 g in 250 ml 12 hrs, soxhlet extraction)	Enhanced antibacterial activity against multidrug-resistant fungal strains	(Balakrishnan et al. 2017)
Dried leaves of nutmeg	Zinc oxide nanorods	100 to 200 nm	Biogenic nanoparticle synthesis using methanol extract from nutmeg leaves	Toxicity on dengue mosquito vectors and cytotoxic effects on liver cancer cells	(Ashokan et al. 2017)

Material	Nanoparticle	Size of nanoparticle	Method	Application	Reference
Ethanol extract from nutmeg seed	AgNPs	~10 nm	Biogenic nanoparticle synthesis using ethanol extract from the nutmeg seed	Antibacterial activities	(Malini et al. 2019)
Nutmeg bark and seed extract Bark(dried)	AgNPs	-	Green approach synthesis of AgNPs using aqueous extract	medicine and related fields due to antibacterial property	(Jelin et al. 2015)
Fresh leaves of nutmeg	gold nanoparticle	29 nm	Biogenic nanoparticle synthesis using water-extracted nutmeg leaf oil	Nanocatalyst for lowering the activation energy for the reduction of methylene blue, methyl orange and para-nitrophenol	(Vilas et al. 2014)
Dried nutmeg seed powder	AgNPs	7–20 nm	Biogenic nanoparticle synthesis using water-extracted nutmeg seed (8 g/100ml at 95°C for 1 hr)	Antimicrobial activities against E. coli and S. aureus cells.	(Sharma et al. 2014)

2.2.3.1 Synthesis of nanoparticles-General

Nanotechnology, a flourished field, deals with the synthesis and utility of nanoscale structures. Nanoparticles are used in water treatment in membranes, filters, disinfection, catalytic activity, and sensors (Roy et al. 2021; Velsankar et al. 2020a). The synthesis of nanoparticles with various chemical compositions, sizes, shapes, and controlled disparities is a significant area of research in this area of study.

a) Synthesis of metal nanoparticles

Metal nanoparticles can be synthesized by using the top-down syntheses method, which uses a destructive approach (figure 2.1). Larger molecules are broken into smaller units and converted into nanoparticles. The bottom-up synthesis approach (building up strategy) is done in reverse as nanoparticles are synthesised from relatively simpler materials (Khan et al. 2017).

Various plant extracts, such as those made from leaves, stems, or fruits, may be used as reducing and stabilising agents for nanoparticle synthesis. Natural substances, including phenols, flavonoids, and terpenoids found in these extracts, can transform metal ions into nanoparticles. When the extract is combined with a metal precursor solution, the reduction process takes place under the right circumstances, creating nanoparticles (Devatha et al. 2016).

Platinum, gold, palladium, and AgNPs are widely used in fast-moving consumer products such as soaps, shampoos, toothpaste, shoes, detergents, cosmetics, and their uses in pharmaceutical and medical items. The use of gold nanoparticles in medicine, illness diagnosis, and drug delivery systems is widespread. In sensor technology, biological levelling, and other biomedical applications, AgNPs are used. (Khandel and Kumar 2018).

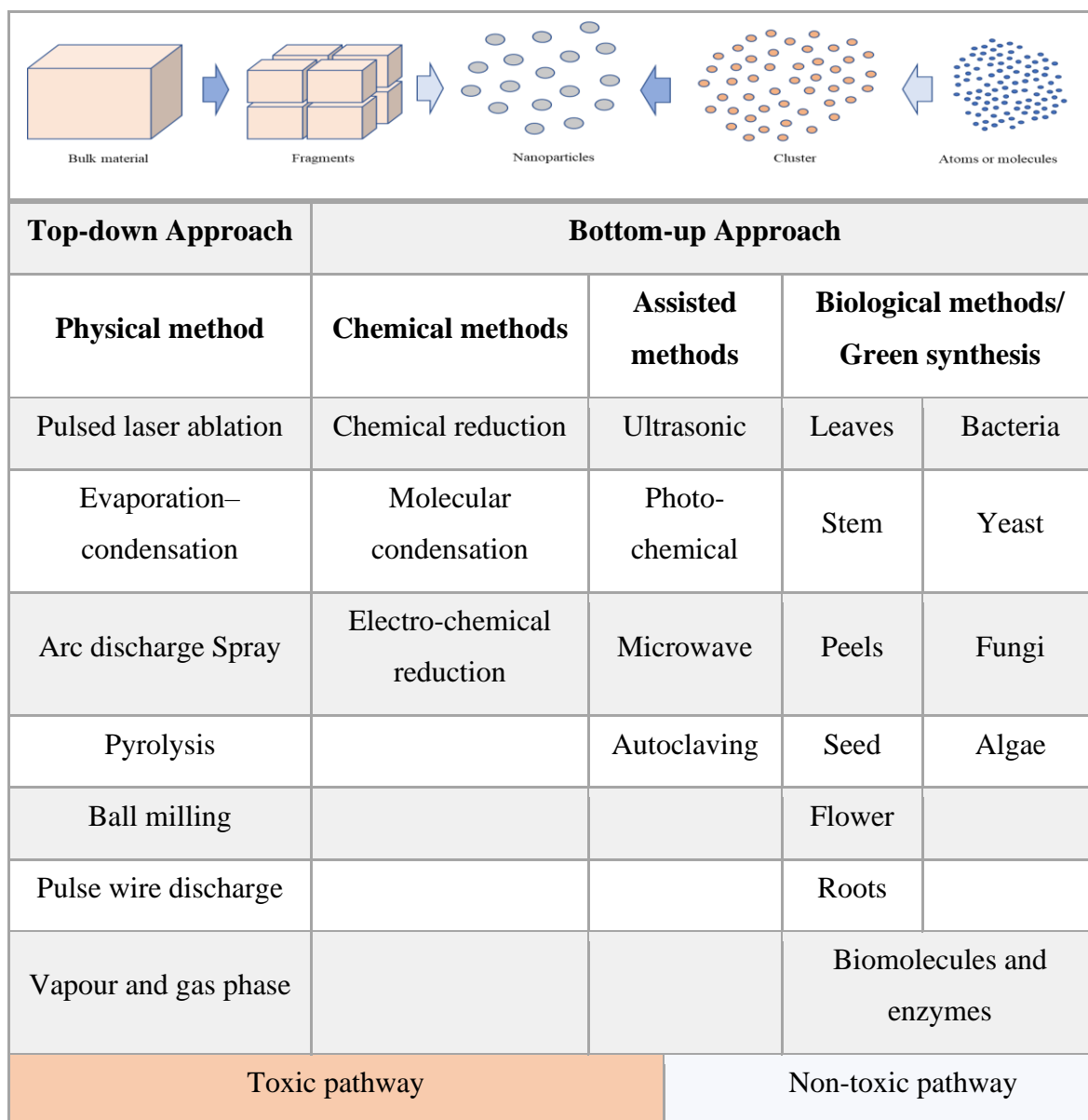


Figure 2.1 Synthesis of nanoparticles

b) Nanoparticle synthesis using nutmeg extracts

Phenolic compounds in plant extractives will enhance the possibility of metal nanoparticle synthesis from its metal salts. NSS extract has higher total phenolic content. The existence of phenols and proteins may act as reducing and stabilising agents (Sharma et al. 2014). Considering its metal chelating capacity, the NSS also can be utilised to reduce metal oxides in its nanoparticle.

Nanoparticle synthesis from metal precursor is done with the help of a reducing agent, which will reduce the ionic state of metal into its neutral state. This particle will be in

its nanosized, and further attraction and formation of bigger size is restricted by the action of a capping agent or stabilising agent, which will cover the nanoparticles with the same charge resulting in repulsion to each other. This mechanism of nanoparticle synthesis is demonstrated in Figure 2.2. Materials required for nanoparticle synthesis, precursor metal: metal salts such as silver nitrate, copper sulphate etc.; stabilising and capping agents: chemicals or plant-based extracts containing reducing and capping agents.

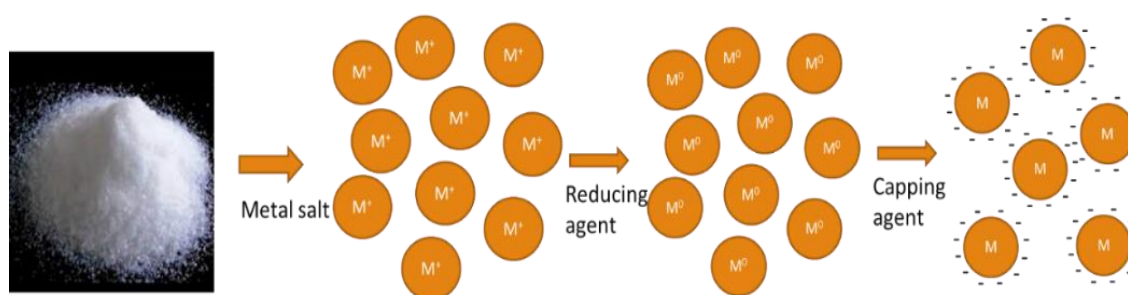


Figure 2.2 Mechanism of nanoparticle synthesis using a reducing and capping agent

AgNPs have wide applications in the medicinal field, textiles, food packaging, plastic coatings, and disinfectant in water treatment systems due to their capability to act against infectious diseases and their application as strong adsorbents (Aravind et al. 2021). Ag NP is attached to the proteins containing sulphur, resulting in the cell malfunctioning. The attachment on the cell wall or penetration through the cell wall results in the cell's death (Haider and Kang 2015). AgNPs are conventionally synthesised using the chemical method using chemicals like hydrazine or sodium borohydride, which is not highly promoted due to its environmental toxicity (Chen et al. 2021). A wide range of applicability leads to a higher demand for AgNPs. A composite of AgNPs with tamarind fruit shell powder is used for the antimicrobial study to check the possibility of its application in the manufacture of antibacterial polymer nanocomposite films for packaging and medical applications (Li et al. 2019).

Biological methods are more applicable in nanoparticle synthesis due to their non-toxic nature, Chemical-free bio-reduction and stabilisation of formed nanoparticles (Aravind et al. 2021). Silver nitrate is considered a precursor for the synthesis of AgNPs. Depending on the synthesis method, nanoparticles can be spherical, rod, triangular shapes, or coated with biomolecules (Haider and Kang 2015). Plant extractives containing proteins, terpenoids, ascorbic acid, and polyphenols act as reducing agents for nanoparticle synthesis

(Shafey 2020; Sharma et al. 2014). These days, agricultural wastes are considered a resource for these bioprocesses (Bankar et al. 2010). The phenolic compounds present in plant extractives will enhance the possibility of metal nanoparticle synthesis from its metal salts. Phenolic compounds belong to the lignans group, which have a chelating property with metallic elements to produce complex compounds (Al-Zahrani and Al-Garni 2019). Nutmeg extracts used for AgNP synthesis are listed in Table 2.4.

Numerous fields have found a use for photocatalysis utilising AgNPs. It is used, for example, to break down organic contaminants in wastewater treatment, synthesise organic chemicals, kill bacteria and viruses, and remove harmful fumes from the environment. The reactive species that are produced can subsequently take part in different catalytic processes. For example, organic pollutants or chemicals may experience oxidation processes in the presence of AgNPs, resulting in their destruction or transformation into less dangerous molecules. The AgNPs facilitate the process while remaining unaltered, acting as a catalyst (Seerangaraj et al. 2021). The production of reactive species is caused by the excited electrons in the AgNPs, which can transmit their energy to nearby molecules or reactants upon light absorption. For instance, depending on the particular parameters of the process, AgNPs can generate electron-hole pairs, reactive oxygen species (ROS), or superoxide radicals (Kordy et al. 2022).

Table 2.4 Nutmeg extracts used for AgNPs synthesis

Material	Extract	Size of nanoparticle	Application and Reference
Nutmeg seed	Ethanol extract	~10 nm	Anti-bacterial activities (Malini et al. 2019)
	Aqueous extract	-	Antiquorum sensing and antibiofilm potential (Balakrishnan et al. 2020)
		25 nm	Enhanced anti-bacterial activity against MDRS (Balakrishnan et al. 2017)
		-	Medicine and related fields due to anti-bacterial properties (Jelin et al. 2015)
		7–20 nm	Antimicrobial activities towards <i>E. coli</i> and <i>S. aureus</i> cells. (Sharma et al. 2014)
Aqueous extract with caffeic acid	20-300 nm	Antimicrobial activities against <i>Bacillus subtilis</i> and <i>Escherichia coli</i> (Thummaneni et al. 2022)	
Nutmeg bark	Aqueous extract	-	Medicine and related fields due to anti-bacterial properties (Jelin et al. 2015)
Nutmeg pericarp	Aqueous extract	13 ±0.63 nm	Antimicrobial and catalytic applications (Sasidharan et al. 2020)
nutmeg oleoresin	-	spherical-shaped, 20–50 nm	Antibacterial, cytotoxicity, drug delivery, and biosensor applications (Madhumithaa et al. 2019)
Nutmeg oil	-	33.2 - 39.7 nm	Antibacterial (<i>S. aureus</i>) and anti-fungal agent (<i>A. niger</i>) (Pauline et al. 2019)

Different techniques are available for characterising green synthesized nanoparticles. A UV-visible spectrophotometer analysis is to confirm the formation of the nanoparticles using plant extracts (Vijayakumar et al. 2021). Higher contact time results in narrow and sharper peak formation in UV- visible spectrophotometer analysis. This indicates the formation of monodispersed nanoparticles. Nanoparticles formation can be confirmed in the liquid state by using small-angle X-ray scattering (SAXS) (Li et al. 2016). And in dried form, the nanoparticles can be analysed for their crystallinity and composition by using X-ray diffraction (XRD) (Kordy et al. 2022). Surface morphology and size are analysed using a field emission scanning electron microscope (FESEM) and a particle size analyser. Fourier-transform infrared spectroscopy (FTIR) analysis determines the chemical compounds responsible for nanoparticle synthesis. Different bioassays are there to assess the antimicrobial, antioxidant, anti-cancer, and anti-diabetic activity (Rahman et al. 2019). The characterization of these nanoparticles is listed in Figure 2.3.

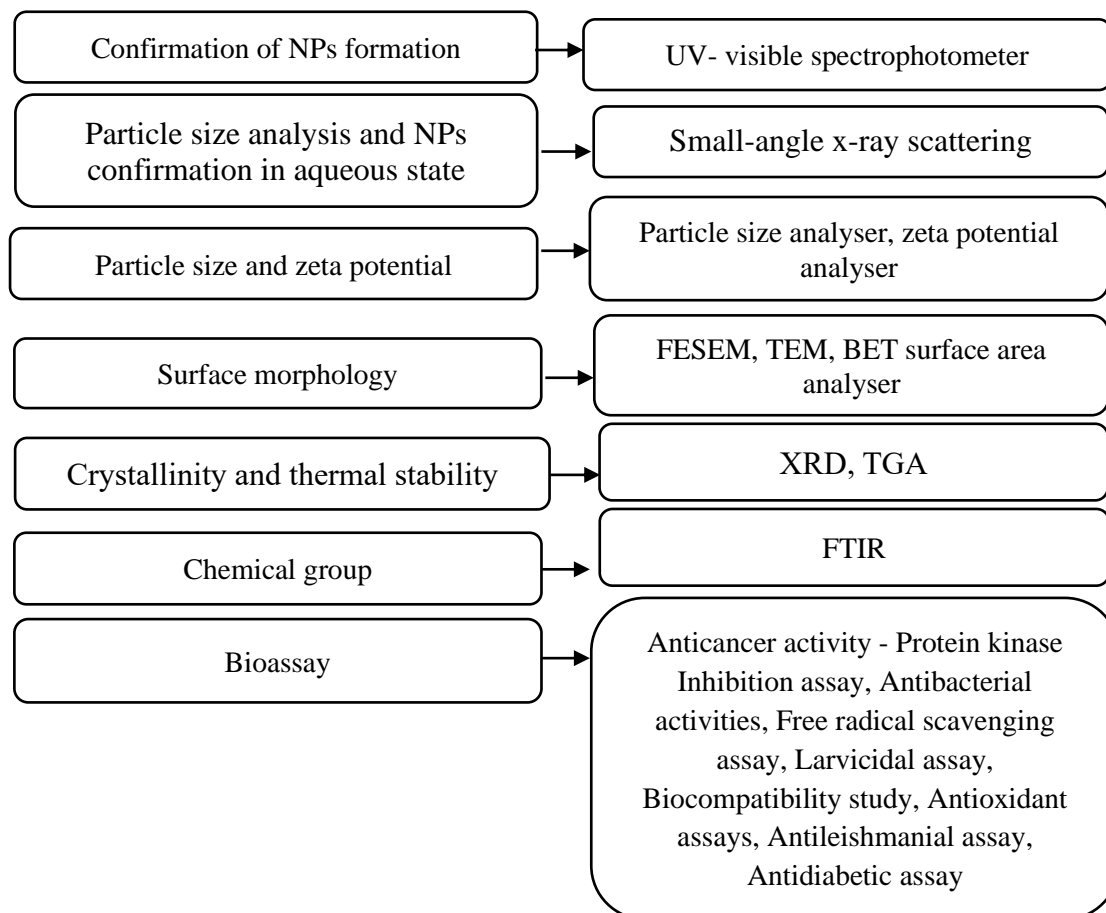


Figure 2.3 Characterisation of nanoparticles

The utilisation of nutmeg for synthesising nanoparticles is being explored in the area of research. To attain the desired nanoparticle properties, optimisation of factors such as extract concentration, reaction duration and pH is required. Depending on their unique features, the use of nanoparticles created also vary. Their prospective uses in a variety of industries, including as catalysis, medicine, and environmental remediation, require more study.

2.2.4 Agricultural waste: Source of lignin

Lignin is the second most abundant polymer on earth. Lignin makes the lignocellulosic biomass rigid and resistant in nature (Xiang et al. 2020). It is carbon-rich and contains poly aromatic structure includes sinapyl, coniferyl and p-coumaryl alcohol (figure 2.4), which makes it more stable in structure and, thus it is not easily degradable as other components of biomass (Donar et al. 2020; Lis et al. 2022). Due to these reasons, it has fewer applications than cellulose, which is mainly used for different applications in the cloth and paper industries.

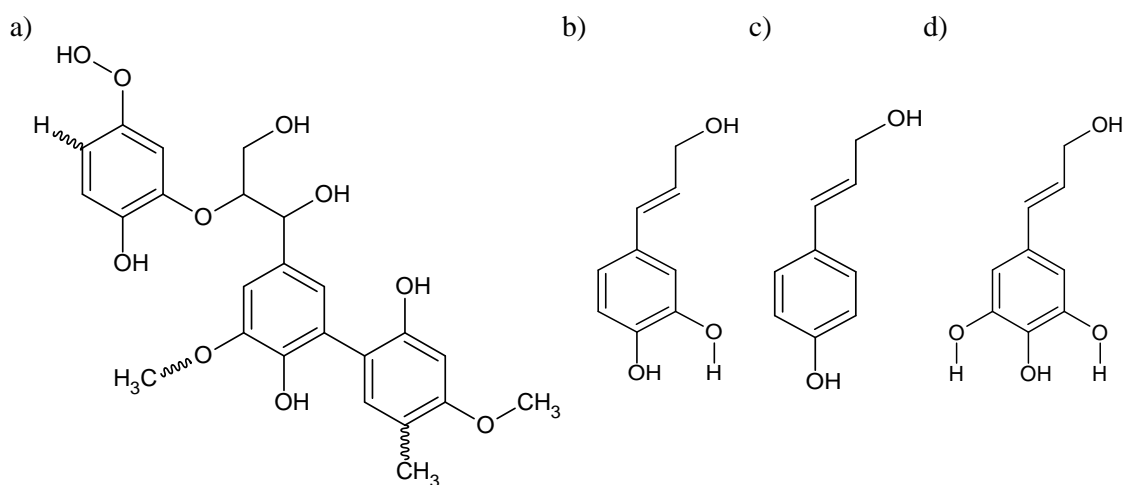


Figure 2.4 a) Structure of lignin b) Coniferyl alcohol c) P-coumaryl alcohol and d) Sinapyl

Studies show more lignin content in peanut shells: 33.5%, coconut shells: 30% (Ragan et al. 2011), almond tree pruning: 25% (P. González-García 2018), Rice straw: 24% (HU et al. 2017) (Table 2.5). The lignin has different applications in water treatment, cosmetics, and UV protection composite preparation. It is possible to use lignin as a renewable energy source.

Table 2.5 Lignin content in different biomass

Material	Lignin content (%)	Reference
Rice straw	24.0	(HU et al. 2017)
Corn stalk	16.0	
Argan press cake	21.7	
Peanut shells	33.5	(P. González-García 2018)
Walnut shell	18.2	
Cocoa shell	13.2	
Bagasse	13.02	
almond tree pruning	25.0	
Coconut shell	30.0	(Ragan et al. 2011)

Considering lignin's complicated structure and strong interactions with other components, extracting it from biomass may become difficult. But a number of techniques have been designed to separate lignin from biomass, including the sulphite process, kraft process, organosolv, soda process, enzymatic process and ionic liquids (Lis et al. 2022).

In the kraft lignin process, the biomass is processed at high temperatures (150–180°C) in a pressurised digester with a solution of sodium hydroxide (NaOH) and sodium sulphide (Na₂S). In the sulphite process, the biomass is treated with a solution of calcium hydroxide (Ca(OH)₂) or sodium hydroxide (NaOH) and sulfuric acid (Shahi 2014). The organosolv extraction technique includes treatment with a solution of acid catalysts and organic solvents, such as ethanol or methanol. The solvents destroy the lignin structure, and the acid catalyst breaks down the lignin-carbohydrate linkages more quickly. Water or a less polar solvent is added to precipitate organosolv lignin (Vannarath and Thalla 2021).

Extraction with a concentrated alkaline solution, such as potassium hydroxide or sodium hydroxide, and precipitation with acid will result in alkaline lignin. With the Steam Explosion technique, lignin is extracted by rapidly depressurizing biomass after short-term exposure to high-pressure steam to cause structural changes. Also, lignin structure is selectively broken-down using enzymes like ligninases or cellulases—this

technique is currently in the early stages of development. The choice of lignin extraction technique is influenced by biomass feedstock, required lignin quality, and intended use. To optimise lignin extraction and purity (Kim et al. 2022).

Kraft and sulphite processes generate higher sulphur content in extracted lignin in these methods. And organosolv, enzymatic and extraction using ionic liquids and not much feasible in case of operational cost and time. Considering all these factors, sulfur-free and pure lignin can be extracted using soda (Lis et al. 2022).

The uses of lignin are now being explored and expanded via continuing research and development. Utilising lignin helps to forward the shift to a more sustainable and circular economy by increasing the value of lignocellulosic biomass and lowering waste. Lignin can be chemically altered to create specific products and high-value compounds. Among these are phenolic chemicals, vanillin (a flavouring ingredient), carbon black (used in the production of rubber), and antioxidants based on lignin. The chemical transformation of lignin can result in the manufacture of a number of chemicals having uses in cosmetics, food additives, medicines, and other fields (Gómez-Avilés et al. 2019). Researchers found that compared to polymers made from petroleum, lignin is sustainable and biodegradable. As a filler or reinforcement in biocomposites, it can be converted into lignin-based polymers or employed to give the materials more stiffness and strength. Potential uses for lignin-based bioplastics include building materials, packaging, and automobile components (Rinaldi et al. 2016).

Lignin-based materials are used for UV protection as binding agents, dispersing agents, carbon filters, and adsorbents (Srisasiwimon et al. 2018). Lignin-based compounds have been investigated for use in agriculture as crop protection agents, plant growth supplements, and fertilisers. Materials made of lignin can improve soil quality, encourage nutrient retention, and aid in managing pests and diseases in crops (Mendu et al. 2012).

Different procedures like pyrolysis or fermentation may transform lignin into liquid biofuels like lignin-based bio-oil or bioethanol or burnt as biomass to provide heat and electricity in factories. By using less fossil fuel and emitting fewer greenhouse

gases, these energy applications help to reduce our dependency on them (Olajuyigbe et al. 2018). Through carbonization or pyrolysis, lignin may be transformed into carbon compounds, including activated carbon and carbon fibres. Applications for lignin-derived activated carbon include gas separation, energy storage, and water and air filtration. Potential applications for carbon fibres made from lignin include lightweight, high-strength materials used in aerospace and automotive components (Ma et al. 2018).

Lignin is used as a carbon precursor for carbon-based materials due to its low toxicity, cost and peculiar properties due to the availabilities of various functional groups (Liu et al. 2021). For the synthesis of semiconductor-based composites, lignin proved its role in the action of controlled nucleation, enhanced catalytic activity and results in microporous morphology. Biosorbents and catalysts are prepared based on lignin due to its above-listed properties and the possibility of enhanced capping molecules in lignin improve the kinetics for the synthesis of semiconductor-doped catalysts (Chen et al. 2016; Srisasiwimon et al. 2018). But the main problem that comes across the use of lignin-based materials is its difficulty in separating the material from treated water by normal processes like sedimentation and filtration. This issue can be rectified by magnetizing the composite to separate it from the solution using a magnet (Jiang et al. 2022).

Lignin-derived materials are used in wastewater treatment due to their high potential to remove pollutants (Wang et al. 2020). Recent years have seen an increase in interest in lignin-based photocatalysts as a sustainable and renewable substitute for dye degradation in wastewater treatment. Lignin as a multifunctional photocatalyst that enables the difficult task of catalysis under solar light, specifically by in situ H_2O_2 production by O_2 reduction and H_2O oxidation (Kim et al. 2022). Lignin's photocatalytic activities can be improved by altering it or combining it with other substances. For instance, lignin may be chemically changed to include more functional groups that improve its light absorption and ROS production. Furthermore, lignin can be mixed with semiconducting substances like silver zinc oxide (ZnO) or titanium dioxide (TiO_2) to make composite photocatalysts that work in concert to increase degradation efficiency. Joshi et al. (2019) reported that a lignin-based ZnO nanostructure synthesis can be used to sense ammonia gas. Modified lignin which is

extracted from oil palm fronds, is proven to be used as a corrosive inhibitor of metals and alloys; this study is mainly intended to extract hydrophobic lignin and thus can improve the anticorrosive property of the prepared material (Hussin 2018).

2.3 Micropollutants and their removal

Micropollutants can include both synthetic chemicals like highly halogenated molecules (like fluorinated surfactants) and naturally occurring substances like oestrogens or antibiotics like penicillin. pharmaceuticals, dyes and personal care products are complex molecules that can persist in the environment and are difficult to treat wastewater.

Numerous textile dyes are made to resist fading and deterioration, so they can keep their colour and look for extended periods of time. However, because of their perseverance, they are also able to sustain themselves beyond textile production plants. Some dyes are difficult to biodegrade and may remain very long in soil, water, and sediments, potentially negatively affecting the environment. Some textile dyes, especially those from the azo dye, anthraquinone dye, and metal-complex dye families, can be poisonous. These colours could have additions that are toxic to aquatic life and ecosystems, such as heavy metals, aromatic compounds, or other chemicals. They may harm aquatic life and upset the balance of ecosystems when discharged into water bodies. It is possible for certain textile dyes to bioaccumulate in living things. As they advance up the food chain, they run the risk of accumulating in the tissues of living things. Higher trophic levels may have higher dye concentrations due to bioaccumulation, which might have an effect on the health of species that consume polluted organisms, such as humans (Cardoso et al. 2022).

Dyes are mainly classified in terms of ionic nature and chemical structure. In terms of ionic nature, it can be classified into ionic and non-ionic. Ionic dyes are more toxic due to their high solubility in water and reactive and stable structure. Most of the non-ionic dyes are less toxic, and dyes which are toxic non-ionic are water-insoluble and hydrophobic. Dyes in the different ionic states as cationic, anionic and zwitterionic, are present in textile wastewater. In terms of chemical structure, dyes are classified as azo (-N=N-), anthraquinone, nitro (-NO₂), triarylmethane, nitroso (-N=O) and indigoid

(Yazdani 2018). To study the real wastewater with different dyes of different ionic states, synthetic wastewater of three different types of ionic dyes is better to be analysed. Anionic, cationic and zwitterionic dyes are considered for this study, and its characteristics and research on removing these dyes are explained in the following paragraphs.

Remazol brilliant blue R (RBBR) is a resistant dye due to an anthraquinone structure. The category of reactive dye is most frequently used in the textile industry due to its long-lasting colour throughout its use. RBBR dye removal using sewage sludge biochar treated at 450°C shows a maximum removal capacity of 126.59 mg/g (Raj et al. 2021). RBBR removal from polyethyleneimine-modified calcium alginate beads also resulted in less adsorption capacity of 28.069 ± 11.659 mg/g (Isik et al. 2021). As a biomass waste for RBBR removal, dried stink bean powder showed less adsorption capacity than other studies. Magnetic chitosan-glutar- aldehyde/zinc oxide/ Fe_3O_4 nanocomposite is also used for RBBR removal, including the complex procedure for the adsorbent process. It brings about a maximum capacity of 176.6 mg/g at an elevated temperature of 60°C (Reghioua et al. 2021a). NSS utilization in the form of biochar has not been tested for its efficacy in removing textile dye. Activation of biomass is done by chemical treatment, which is not in the case of biochar preparation (Yuan et al. 2021).

Methyl violet 10B (MV), also known as crystal violet (Hexamethylpararosaniline Chloride) with chemical formula $\text{C}_{25}\text{H}_{30}\text{ClN}_3$, is a cationic synthetic dye with a highly stable organic structure and highly intense colour that is widely utilised as a biological staining agent and in textile applications. The dye is recalcitrant and has been discovered to result in cancer, chromosomal damage and mutagenesis with abnormal growth of metaphases (Seerangaraj et al. 2021).

Rhodamine B (RhB) is one of the most harmful dyes and is extensively used in industries like textile, ink and crackers due to its non-degradability and stability. RhB dye (zwitterionic dye) is carcinogenic and neurotoxic to animals and humans (Shaikh et al. 2020). These synthetic textile dyes are also illegally used in food commodities (sweets, chilli powder). Rhodamine B, malachite green, and methyl violet are restricted from use in the production of hair colours under the jurisdiction of Rule (EC) No.

1223/2009 due to their toxicity. This regulation also prohibits synthetic organic dyes. So far, most alerts concern the banned use of synthetic organic dyes such as Sudan I - IV, para red, RhB and orange II in food (Tkaczyk et al. 2020). Several studies have been conducted for RhB removal by adsorption and photocatalysis and show it is more efficient for a lower concentrated effluent treatment due to its fluorescent-resistive structure (Alshehri and Malik 2020; Islam 2020).

The removal of micropollutants in wastewater typically involves the application of various advanced treatment technologies, including adsorption, membrane filtration reverse osmosis, nanofiltration, ultrafiltration, advanced oxidation processes (ozonation, photocatalysis, and oxidation with hydrogen peroxide), biological treatment (degradation using microbes, sequencing batch reactors, activated sludge processes, and membrane bioreactors) (Punypwar and Mutnuri 2022; Pype et al. 2019), chemical precipitation, ion exchange and electrochemical treatment (electrocoagulation and electrooxidation) (Thamaraiselvan et al. 2021).

a) Adsorption: The adsorption technique is mainly used in textile wastewater treatment due to its simple process, low cost, specific physicochemical affinities between dyes, and minimal matrix effects (Suteu et al. 2010). It involves the adsorption of pollutant molecules to the surface of an adsorbent, a solid substance. Biochar, activated carbon, zeolites, silica gel, and other substances having a large surface area and an affinity for micropollutants can all be used as adsorbent material (Fu et al. 2021). It has become common to eliminate these micropollutants using modified adsorbents (Quesada et al. 2019).

The adsorption process includes the following steps: on the surface of the adsorbent, micropollutant molecules in the liquid phase come into contact. Diffusion is the mechanism by which the micropollutant molecules travel from the bulk liquid phase to the surface of the adsorbent. When the micropollutant molecules reach the adsorbent's surface, weak intermolecular forces such as van der Waals forces, hydrogen bonds, or electrostatic interactions help them stick to the surface. The concentration of micropollutants on the adsorbent surface remains constant when the rate of adsorption and desorption of micropollutant molecules reaches equilibrium (Ahmed et al. 2014; Al-Gheethi et al. 2022).

The kinetics of adsorption describes the rate at which adsorption takes place. The pseudo-first-order and pseudo-second-order models, intraparticle diffusion, and the Elovich model are the most often used kinetic models for adsorption (Chandra et al. 2020). The adsorption rate is assumed to be proportional to the difference between the equilibrium concentration and the concentration at any time in the pseudo-first-order model (Tepe 2018). In the pseudo-second-order model, the adsorption rate is assumed to be proportional to the square of the difference in the equilibrium concentration and the concentration at any given time. The intraparticle diffusion model assumes that the adsorbate diffusion within the adsorbent material's pores is the rate-limiting stage in adsorption. It implies that adsorption happens in multistage, starting with a quick adsorption phase and moving onto a slower phase where intraparticle diffusion acts as the rate-limiting step (Sathishkumar et al. 2012). The Elovich model is predicated on the assumption that there are several stages to the adsorption process, including chemisorption and surface reactions. According to the Elovich model, the initial adsorption rate of the process is large and steadily declines over time. The amount of adsorbate adsorbed and the time is assumed to have a logarithmic relationship in the model (Esvandi et al. 2020).

The relation between the quantity of pollutants adsorbed onto the adsorbent surface, and the concentration of micropollutant at a constant temperature can be observed by adsorption isotherms (Zulfiqar et al. 2020). The Langmuir, Freundlich, and Temkin isotherm models are some of the isotherm models that are most often employed. The Langmuir isotherm assumes that monolayer adsorption takes place on a homogenous surface with a limited number of identical sites for adsorption. The Freundlich isotherm proposes that multiple layers with varying adsorption energies are deposited onto a heterogeneous surface. The Temkin isotherm model assumes that binding energies will be dispersed uniformly over the adsorbent's surface. Adsorbate-adsorbate interactions and interactions between the adsorbate and the adsorbent are also considered (Reghioua et al. 2021b).

Thermodynamic studies can determine the viability and spontaneity of the adsorption process. Nature of adsorption, such as whether it is exothermic or endothermic and whether it is driven by entropy or enthalpy, can understand by looking

at the Gibbs free energy change, enthalpy change, and entropy change, which are three important thermodynamic parameters (Zulfiqar et al. 2020).

b) Photocatalysis: The photocatalysis method uses light energy to enhance chemical processes which will result in the degradation of pollutants. A photocatalyst absorbs light in the dye degradation process, producing reactive oxygen species (ROS) such as hydroxyl radicals ($\bullet\text{OH}$), which may oxidise and degrade organic molecules, including dyes. Photocatalysis has a potential method for dye degradation because it can eliminate contaminants from the environment by producing minute amounts of secondary waste in the presence of light. In actual use, several dyes are present in the wastewater due to the blending of the effluents or mixing of different dyes to make colour varieties. The efficiency of mixed dye solutions for photocatalytic dye degradation thus becomes crucial, yet there are few such experiments.

Some of the semiconductors (titanium dioxide, silver, iron nanoparticles) combined with plant compounds (cellulose, lignin) or polymers (polyvinyl alcohol, chitosan) or carbon components (biochar, activated carbon, carbon nanotubes, graphite oxide) resulted in better efficiency for degradation of emerging contaminants like micropollutants (Budnyak et al. 2021; Eskalen et al. 2022; Gómez-Avilés et al. 2019; Mohami et al. 2022).

2.3.1 Nanoparticles and composites for catalytic treatment of wastewater

For catalytic applications in wastewater treatment, nanoparticles and composites have demonstrated tremendous potential. These novel substances are useful in various wastewater treatment procedures because they have greater stability, expanded surface area, and enhanced catalytic activity. Various nanoparticles and composites are used in the catalytic treatment of wastewater. The kind of pollutants, the circumstances surrounding the reaction, and the desired outcome of the treatment all influence the selection of the best material. Ongoing research aims to improve existing materials, discover novel nanocomposites, and create sustainable and affordable catalytic methods for wastewater treatment.

Silver, gold, platinum, and palladium metal nanoparticles are good catalysts. They may be used for a variety of catalytic activities, such as the oxidation, reduction, and

degradation of organic pollutants in wastewater. To increase their stability and recyclability, these nanoparticles can be supported by substances like carbon nanotubes, graphene, or metal oxide supports (Podasca et al. 2019). The potential for catalytic wastewater treatment of carbon-based nanomaterials, such as graphene, carbon nanotubes, and activated carbon, has been extensively studied. These substances have a strong potential for adsorption and can support catalysts. They are efficient in removing heavy metal ions and organic pollutants from wastewater. (Anooj et al. 2019; Cardoso et al. 2022).

Photocatalytic characteristics may be found in semiconductor nanoparticles like silver, zinc oxide and titanium dioxide. They produce electron-hole pairs when exposed to light, which can take part in redox processes and oxidise organic contaminants. Removing numerous organic contaminants and dyes from wastewater has shown promise when using semiconductor nanoparticles (Sagadevan et al. 2021). Compared to single metal nanoparticles, bimetallic nanoparticles, made of two distinct metals, offer improved catalytic activity and selectivity. They have been utilised for wastewater treatment applications such as the degradation of organic pollutants, removal of heavy metals, and advanced oxidation processes. They may be synthesised using a variety of techniques (Umar et al. 2013).

2.4 Summary of literature review

Micropollutant removal using biochar derived from biomass wastes is the least studied research area. Industrial wastewater has a higher concentration of these pollutants. It is estimated that 10 – 40% of dye from industry is discharged to the surface water body, which will reduce dissolved oxygen and impart toxicity to the water body (Rainert et al. 2021). A category of reactive dye is most frequently used in the textile industry due to its long-lasting colour throughout its use. Remazol Brilliant Blue R (RBBR), Methyl Violet 10B (MV) and Rhodamine B (RhB) dye, which are some of these dyes, are resistant to degradation due to their stable structure. The conventional treatment methods and materials fail to remove these micropollutants from the wastewater to their safety level. Polymer composites and sponge-like materials are widely studied in this area due to their higher removal efficiency. These include polymers and chemicals in the production, which impact the environment

while disposing of and increasing the number of microplastics in the water matrix. Degradation of dyes is better than removing dyes using different treatment methods. Before wastewater is discharged into natural sources, dyes must be completely or partially removed, degraded or mineralized to CO₂, non-toxic chemicals with low molecular weight, and water. This poses a real and serious concern for environmental protection and public health (Suteu et al. 2010). NSS is an agricultural waste with a higher content of lignin, antioxidants, phenolic and flavonoid content. This agricultural waste will prepare materials such as lignin-based adsorbents and nanoparticles to effectively remove these pollutants. The researchers are concentrating on developing material for the simultaneous removal of pollutants sustainably (Budnyak et al. 2021).

In this project, the major motive is to synthesise material based on agricultural waste: an NSS with a higher removal capacity for dye degradation. Biochar preparation does not involve any chemical treatment for its activation (Yuan et al. 2021). Extractives from nutmeg-containing reducing and capping agents can be used to synthesise metal nanoparticles. Lignin has high phenolic content as a reducer and acts as a good adsorbent to remove pollutants from wastewater. In-situ preparation of magnetised lignin for the photocatalytic degradation of anionic and cationic dye can rectify the issue of separating the catalyst from the treated water. High lignin content in nutmeg shells leads to the possibility of synthesising lignin-based composites for better degradation of dyes at higher concentrations.

2.5 Objectives

- 1) To evaluate the performance of nutmeg seed shell-based biochar on removing micropollutants.
- 2) To synthesise and characterise nutmeg seed shell-based nanoparticles and composites
- 3) To assess the performance of nutmeg seed shell-based nanoparticles and composites for the micropollutant removal

CHAPTER 3

MATERIALS AND METHODOLOGY

3.1 General

In this chapter, a summary of the material used for the work and methodology adopted for the experimental studies are discussed in detail.

3.2 Materials

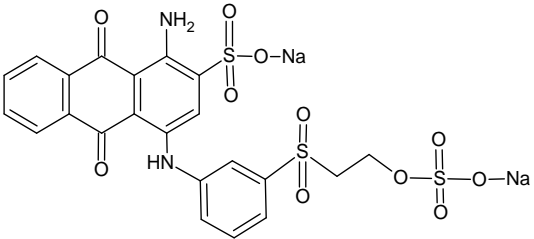
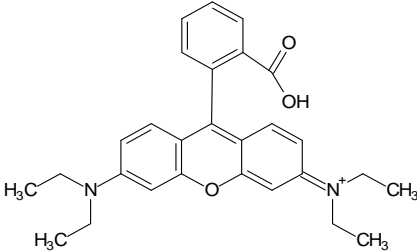
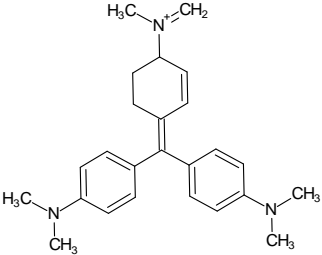
3.2.1 NSS collection and pre-processing

Nutmeg seed shell is the agricultural waste used as the substrate in this study to assess its capability of micropollutants removal. Nutmeg waste was collected from the Angamaly-Kalady region of Kerala, India, where the main production of nutmeg occurs. The dirt is removed by washing and rinsing with double-distilled water and then dried in a hot air oven at 105°C to a constant weight. Dried NSS were crushed, sieved to 105µm, and stored in an air-tight polyethene zip lock cover.

3.2.2 Chemicals

All the chemicals used for the experimental work are of analytical grade. 1,1-diphenyl-2-picrylhydrazyl (DPPH) (TCI chemicals), Silver nitrate (Molychem India), ampicillin (Sigma Aldrich), and other chemicals like gallic acid, hydrochloric acid, ferric cyanide, Sulphuric acid, Ferric chloride, Sodium hydroxide, chloroform, potassium hydroxide, salicylic acid, ferrous sulphate, Foline-Ciocalteu reagent and hydrogen peroxide are purchased from Sigma Aldrich and Loba chemi. The dyes used for the study and their properties are listed in Table 3.1.

Table 3.1 Physical and chemical properties of dyes used in the study

	Remazol Brilliant Blue R (RBBR)	Rhodamine B (RhB)	Methyl Violet 10B (MV)
Chemical name	Disodium 1- amino- 9, 10 – dioxo– 4 - [3 -(2sulfonatooxyethyl sulfonyl) anilino] anthracene – 2 -sulfonate	N-[9-(2-carboxyphenyl)-6-(diethylamino)-3H-xanthen-3-ylidene]-N-ethylethanaminium	Tris(4-(dimethylamino)phenyl)methylium chloride
Chemical Formula	C ₂₂ H ₁₆ N ₂ Na ₂ O ₁₁ S ₃	C ₂₈ H ₃₁ ClN ₂ O ₃	C ₂₅ H ₃₀ N ₃ Cl
Other names	Reactive Blue - 19	Brilliant Pink B	Basic Violet 3, Gentian Violet, Hexamethylpararosaniline chloride, Crystal Violet
Molecular Weight	626.54	479	407.98
Colour Index Number	61200	45170	42555
CAS number	2580-78-1	1-88-9	548-62-9
Maximum wavelength, λ_{max}	590 nm	568 nm	595 nm
Structure of dye			
Application	Textile industries	Ink, crackers, textiles, paper dyeing and dye laser	Pen ink, biological staining agents and textiles

3.3 Overall workflow

The present study includes the modification of NSS and its utilization for dye removal. Figure 3.1 shows the methodology adopted in the present work. The characterization of biomass selected for the study (NSS) is carried out as listed in Table 3.2. All the laboratory experiments are conducted in triplicates.

This project is executed mainly in three phases. The first phase deals with the biochar preparation from NSS, characterising and analysing its dye removal capacity. The second phase is based on the AgNP synthesis using NSS extract, its characterization and using AgNPs as a photocatalyst for dye degradation. The third phase deals with extracting lignin from NSS and then preparing a silver lignin composite with the magnetic property. This composite is further used for the dye degradation study.

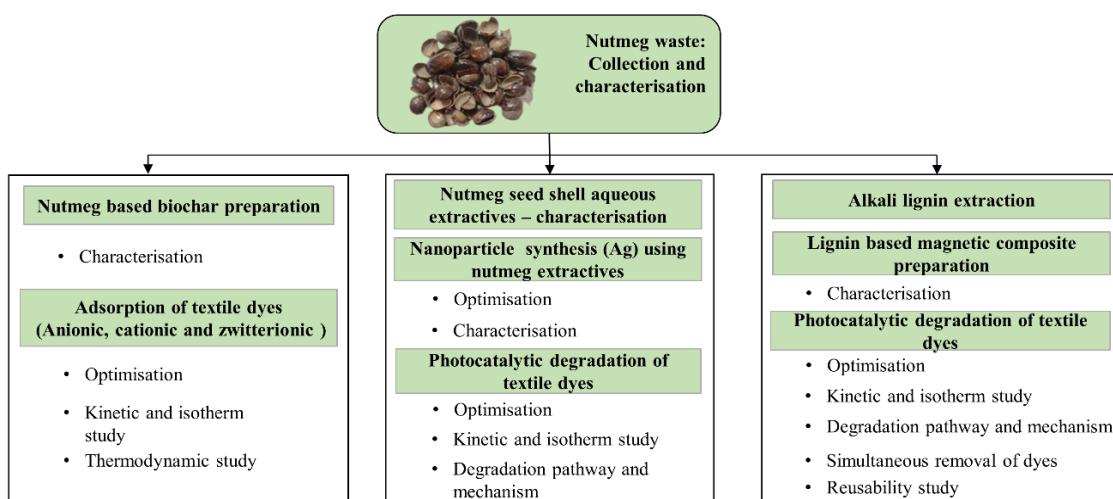


Figure 3.1 Experimental flowchart for present project work

3.4 NSS biochar as an adsorbent for the removal of dyes

3.4.1 NSS biochar preparation

NSS was cleaned several times using double distilled water to remove contaminants and soluble materials and sundried. The material was then kept in an oven to dry at 105°C, ground and sieved through a 106 µm sieve. NSS biochar was prepared in a muffle furnace at 500°C for 4 hours. The obtained NSS biochar was cooled in a desiccator and washed with double distilled water. The pH was neutralised using 0.1 M HCl solution. Biochar is then oven-dried at 105°C and stored in a desiccator to keep dry until use. Characterisation of NSS biochar is analysed as listed in Table 3.2.

Table 3.2 Biomass characterisation and techniques

<i>Technique / Instrument</i>	<i>Equipment model/ Method adopted</i>	<i>Purpose/parameters</i>
Characterisation of NSS		
Moisture content	ASTM D1348-94	Dry weight analysis
Ultimate analysis	ELEMENTAR Vario EL III	Elemental analysis
Experimental procedure for determination of biomass composition	TP-510-42618, TP-510-42620 and TP-51042621	Determination of lignin, hemicellulose and cellulose
Characterisation of NSS and NSS biochar		
X-ray diffraction (XRD)	Empyrean 3 rd Gen, Malvern PANalytical	Analysis of Elemental constituents, the crystallinity of sample 2 θ : 10° -80°, monochromatic Cu K γ radiation, λ = 0.1540598 nm, Generator voltage: 45 kV, Tube current: 40 mA
Thermogravimetric analysis (TGA)	Hitachi Exstar TGA-DTA 6300	Thermal stability analysis, Sample weight: 20mg in an alumina crucible, Scanning temperature 25 to 860°C, Heating rate: 20°C/min under nitrogen atmosphere
Fourier-transform infrared spectroscopy (FTIR)	PerkinElmer Spectrum	Functional groups (wavenumber range of 400 cm ⁻¹ – 4000 cm ⁻¹ KBr method, number of scans: 10 Resolution: 4 cm ⁻¹ at room temperature)
Surface morphology	Field Emission scanning electron microscope (FESEM)	GeminiSEM-300, (Samples are coated with gold to make the sample conductive)

3.4.2 Biochar yield

The percentage yield of NSS biochar obtained from raw NSS was calculated using Eq. (3.1) (Ahmad et al. 2020a):

$$\text{Percentage Yield (\%)} = \frac{M_{BC}}{M_N} \times 100 \quad (3.1)$$

Where, M_{BC} and M_N are the obtained masses of NSS biochar and NSS (g), respectively.

3.4.3 Adsorption

Removal of dye was analysed by batch mode adsorption study. The optimisation of the process considered independent parameters like pH, contact time, adsorbent dosage, and the concentration of dye in water (Morosanu et al. 2019). After the supernatant separation, the dye concentration in the solution was analysed using the UV-Visible spectrophotometer at λ max (RBBR: 590 nm, RhB: 568 nm, MV: 595 nm). The physical and chemical properties of the dyes used for this study are listed in Table 3.1. Optimisation of the adsorption process for the removal of dye is done by Response Surface Methodology (RSM). The quantity of the adsorbed dye on the adsorbent at the equilibrium time (q_e) was determined using Eq. (3.2) (Wang et al. 2011).

$$q_e = \frac{V(C_0 - C_e)}{m} \quad (3.2)$$

where C_0 is dye concentrations (mg/L) at the initial times, and C_e is dye concentrations (mg/L) at the equilibrium times. V is the volume (L) of the initial dye aqueous solution.

3.4.4 Adsorption isotherms

The adsorption isotherm illustrates the mechanism behind the mobility and retention of adsorbate with respect to the adsorbent. Three isotherm models are considered to evaluate adsorption behavior by examining adsorbent-adsorbate interaction and adsorption energy. Due to their adaptability, simplicity, and application to various adsorption systems, these isotherm models are frequently employed. In this study, the Langmuir, Freundlich and Temkin isotherm models (Hii 2021; Raj et al. 2021; Waheeb et al. 2020) are selected for fitting the adsorption data (Eq. 3.3 – 3.5).

$$\frac{C_e}{q_e} = \frac{1}{q_m K_L} + \frac{C_e}{q_m} \quad (3.3)$$

$$\ln q_e = \ln K_F + \left(\frac{1}{n}\right) \ln C_e \quad (3.4)$$

$$q_e = B_T \ln(K_T) + B_T \ln(C_e) \quad (3.5)$$

where C_e is the concentration of the dye at equilibrium condition (mg/L); q_e is the amount of adsorption at equilibrium (mg/g); q_m is the maximum adsorption amount from the Langmuir model (mg/g); K_L is the adsorption amount parameter for Langmuir isotherm (L/mg); K_F is affinity coefficient for Freundlich isotherm (L/g), and n is linearity index Freundlich isotherm study. $(1/n)$, determines the adsorption intensity. B_T is a factor associated with the heat of adsorption (J/mol), and K_T is the equilibrium constant for the Temkin model (L/mg) (Ghaedi et al. 2012). In particular, the Langmuir isotherm can be described with a dimensionless constant separation factor R_L (Eq. 3.6) (Ghaedi et al. 2012).

$$R_L = \frac{1}{C_0 K_L} \quad (3.6)$$

The R_L value reveals whether the isotherm is unfavourable if $R_L > 1$, the isotherm is linear if $R_L = 1$, the isotherm favourable if $0 < R_L < 1$, and if $R_L = 0$, the isotherm is irreversible.

3.4.5 Adsorption kinetics

The kinetic study determines the potential rate-limiting steps involved in the adsorption process. The pseudo-first-order, pseudo-second-order, Intraparticle diffusion and Elovich model (Eq. 3.7 – 3.10)(Rahmat et al. 2016; Raj et al. 2021; Zahoor and Ali Khan 2018), are considered to investigate adsorption kinetics in this work. Pseudo-first-order and pseudo-second-order models are used to distinguish kinetic equations based on the extent to which initial dye concentration affects adsorption capacity. The Elovich kinetic model assumes that the adsorbent surfaces are heterogeneous and in a multilayer adsorption process.

$$\ln q_e - q_t = \ln q_e - t k_1 \quad (3.7)$$

$$\frac{t}{q_t} = \frac{1}{(q_e)^2 K_2} + \frac{t}{q_e} \quad (3.8)$$

$$q_t = k_{dif} t^{(1/2)} + C \quad (3.9)$$

$$q_t = \frac{1}{b} \ln(ab) + \frac{1}{b} \ln t \quad (3.10)$$

where, q_e is the quantity of dye adsorped at equilibrium (mg/g); q_t is the quantity of adsorption at equilibrium at time t (mg/g); k_1 is the coefficients of reaction rate for

pseudo-first-order (min^{-1}); k_2 is coefficient of reaction rate for pseudo-second-order model ($\text{g}/(\text{mg}\cdot\text{min})$); k_{diff} is rate constant for intraparticle diffusion ($\text{mg}/\text{g min}^{1/2}$), and C is the intercept (gives information on the thickness of the boundary layer) (Suteu et al. 2010; Zahoor and Ali Khan 2018). a is the initial sorption rate (mg/gmin), and b is the extent of surface coverage and activation energy for chemisorption (g/mg) (Hii 2021).

3.4.6 Thermodynamic studies

Thermodynamic parameters are checked to analyse the dye adsorption process concerning the temperature change. The studies are conducted at the temperature range of $30^\circ\text{C} - 45^\circ\text{C}$. The parameters like entropy change (ΔS^0), Gibbs free energy change (ΔG) and enthalpy change (ΔH^0) are analysed. ΔG , which is expressed in kJ/mol , is calculated by Eq. (3.11 – 3.13) (Gautam et al. 2015):

$$\Delta G = -RT \ln K_d \quad (3.11)$$

Where R is the universal gas constant ($R = 8.314 \text{ kJ}/\text{mol}$), T represents the temperature (K), and K_d is the equilibrium constant for the adsorption process expressed in L/mol was determined by the following equation (Eq. (3.12)) (Raj et al. 2021):

$$K_d = \frac{q_e}{C_e} \quad (3.12)$$

Where q_e (mg/g) is the quantity of the dye adsorbed on the NSS biochar at the equilibrium stage, and C_e is the final dye concentration in solution (mg/L). Van't Hoff equation is used for the analysis, which can be written as shown in Eq. (3.13)(Suteu et al. 2010):

$$\ln K_d = \frac{\Delta S^0}{R} - \frac{\Delta H^0}{RT} \quad (3.13)$$

Where ΔS^0 is the entropy change (kJ/molK), and ΔH^0 is the enthalpy change (kJ/mol).

3.5 Synthesis of AgNP using NSS extract and evaluation of its potential as a catalyst for dye degradation

3.5.1 Preparation of NSS aqueous extract

NSS was washed with double distilled water to eliminate the impurities, then dried in a hot air oven at 105°C till it reached a constant weight. Dried NSS were crushed and sieved to $105 \mu\text{m}$ in size. 10g of the dried NSS powder was added to 100

mL of distilled water and stirred at 90°C for 1 hour. The solution obtained was then filtered and centrifuged at 10,000 rpm for 10 min. The supernatant solution was stored at 4°C for further use. NSS extract is used to synthesise AgNPs.

3.5.2 Phytochemical analysis of NSS extract

The NSS aqueous extract was tested to determine the presence of active chemical components by determining tannins, saponins, flavonoids, steroids, terpenoids, alkaloids, polyphenols, phlobatannins, alkaloids and quinones (Auwal et al. 2014; Rizwan et al. 2020; Saxena 2012; Velsankar et al. 2020b; Widjanarko et al. 2014). The methodology adopted to analyse these is explained below. The experiments are repeated for reliability.

a) Alkaloids (Wagner's test): To 2 ml of NSS extract with Wagner's reagent resulting in a reddish-brown tint precipitate shows the existence of alkaloids (Widjanarko et al. 2014)

b) Saponins: 2 mL of NSS extract mixed with 2 mL of double distilled water and shaken vigorously for 5 min. The presence of honeycomb froth even after 30 min indicates the presence of saponins (Saxena 2012).

c) Flavonoids: 5 mL ammonia solution with NSS extract and concentrated sulphuric acid, which resulted in yellow colour and then vanished with time due to the flavonoids' presence (Velsankar et al. 2020b).

d) Polyphenols: 4 mL ethanol with 1 mL of extract heated for 15 min, and three drops of ferric cyanide were added. The blue-green colour represents the presence of polyphenols (Velsankar et al. 2020b).

e) Phlobatannins: 2 mL of the NSS extract with diluted HCl resulted in the red precipitate, showing the existence of phlobatannins (Auwal et al. 2014).

f) Tannins: Ferric chloride solution (10%) added to 2 mL of extract. The blackish-blue or green-blackish colour indicates the occurrence of tannins (Auwal et al. 2014).

g) Terpenoids: 5 mL NSS extract was added to 2 mL of chloroform, and 3 mL concentrated H₂SO₄ resulted in reddish-brown colour, indicating the presence of terpenoids (Velsankar et al. 2020b).

h) Quinones: Alcoholic KOH with extract resulted in a red-to-blue colour showing the presence of quinines (Rizwan et al. 2020).

i) Steroids: 2 mL acetic anhydride added and mixed with 1 mL extract of NSS extract and 2 mL H₂SO₄ resulted in the violet colour change to blue or green, showing the presence of steroid content (Saxena 2012).

j) Total Phenolic compound: Folin–Ciocalteu colourimetric method analyses phenolic contents in NSS aqueous extract. Standards for the calibration is prepared using gallic acid. The results were expressed as gallic acid equivalents (GAE)/100 g dry weight of plant material (Saravanakumar et al. 2015).

3.5.3 Green synthesis of AgNPs

Synthesis of AgNPs is done by the method proposed by Sasidharan et al., (2020) with some modifications. Briefly, 5 ml of NSS extract with 95 ml of 1 mM silver nitrate is exposed to sunlight for 30 min. The dark brown colour in the reaction mixture represents the presence of synthesised AgNPs due to surface plasmon vibration. The contents are centrifuged at 10000 rpm for 20 minutes to separate the synthesised AgNPs, repeatedly washed with double distilled water, and then dried and stored.

3.5.4 Characterisation of AgNPs

The techniques and chemicals used for determining the characteristics of nanoparticles synthesised in this study are listed in Table 3.3.

Table 3.3 Characterisation and techniques

<i>S. No:</i>	<i>Technique / Instrument</i>	<i>Equipment model</i>	<i>Purpose/parameters</i>
1	UV-visible double-beam spectrophotometer	Analytical technologies 3080-TS	AgNP formation and dye concentration (spectral range of 200–800 nm)
2	Small-angle X-ray scattering (SAXS)	Empyrean 3 rd Gen, Malvern PANalytical	Size distribution of AgNPs in aqueous solution
3	Zeta potential	Malvern Zetasizer	Particle charge analysis
4	Particle size analysis	Horiba nano partica SZ-100	Particle size analysis
5	X-ray diffraction (XRD)	Empyrean 3 rd Gen, Malvern PANalytical	Analysis of elemental constituents
6	Thermogravimetric analysis (TGA)	Hitachi Exstar TGA-DTA 6300	Thermal stability of AgNPs (Sample tested at 30°C to 800°C in an alumina crucible under a nitrogen atmosphere)
7	Fourier-transform infrared spectroscopy (FTIR)	PerkinElmer Spectrum	Functional groups (wavenumber range of 400 – 4000 cm ⁻¹)
8	BET surface area analyser	Autosorb IQ-XR-XR, Anton Paar, Austria	Surface area, pore size and volume
9	Field Emission Scanning Electron Microscope (FESEM)	GeminiSEM-300	surface morphology of AgNPs (10 K magnification)
10	UPLC- MS	Xevo QToF, Waters	Parent and fragment molecule analysis

3.5.5 Antioxidant activity of AgNPs

The antioxidant activity of synthesised nanoparticles is carried out by conducting a 2,2, -Diphenyl-2-picrylhydrazyl (DPPH) free radical scavenging assay and a hydroxyl radical-scavenging assay. Free radicals are unstable chemicals that may damage cells and tissues through oxidative stress, whereas antioxidants are compounds that can shield cells from their harmful effects (Ansar et al. 2020).

a) DPPH free radical scavenging assay: The presence of free radicals results in cell degradation. The effect of synthesised AgNPs is tested against DPPH free radicals (Ansar et al. 2020; Brand-Williams et al. 1995) to determine the efficiency of AgNPs in reducing the effect of free radicals. Equal amounts of different concentrations (12.5 µg/mL, 25 µg/mL, 50 µg/mL, 100 µg/mL and 200 µg/mL) of synthesised AgNPs are mixed with 0.1 mM DPPH in 95% methanol. The mixture was shaken vigorously at room temperature for 30 min in the dark condition. As a control, ascorbic acid was used. The absorbance of the mixture was measured in a double-beam spectrophotometer at 515 nm, and the DPPH free radical scavenging activity was determined using Eq. (3.14).

$$DPPH \text{ free radical scavenging activity (\%)} = \left(1 - \frac{A_{AgNP}}{A_{DPPH}}\right) \times 100 \quad (3.14)$$

Where A_{AgNP} and A_{DPPH} are the absorbance of synthesised AgNPs and DPPH at 515 nm respectively.

b) Hydroxyl radical-scavenging assay: Free radicals similar to hydroxyl radical will result in DNA damage and thus leads to cell degradation (Rao et al. 2020). Synthesised AgNPs are also tested for their hydroxyl radical scavenging activity. Hydroxyl radical scavenging assay was conducted by adding 1 mL of synthesised AgNPs with different concentrations to a solution of 1.5 mL of salicylic acid (18 mM), 1.5 mL ferrous sulphate (18 mM) and 1 ml of hydrogen peroxide. This blend was incubated at 37 °C for 60 min. After incubation, the solution was analysed by a UV-visible double-beam spectrophotometer at a wavelength of 510 nm to determine the corresponding absorbance (Saravanakumar et al. 2015). Hydroxyl radical-scavenging activity was then determined by equation (3.15)

$$\text{Hydroxyl radical scavenging activity (\%)} = \left(1 - \frac{A_1}{A_0}\right) \times 100 \quad (3.15)$$

Where A_0 and A_1 are the absorbance of the control and sample, respectively.

3.5.6 Antibacterial activity of AgNPs

Gram-positive and Gram-negative bacterial infections fall into two primary types. Based on the way the bacteria respond to the gram stain, the classifications are determined. Thus, the antibacterial activity of extract and nanoparticles are analysed for gram-positive (*E. coli rosetta* (RDS) and *Pseudomonas aeruginosa* (P)) and gram-negative bacteria *Bacillus subtilis* (BS) and *Bacillus haynesii* (BH)). Microbes are cultured in nutrient agar in a petri dish. The disc diffusion method with 5 mm sterile discs is implemented for the antibacterial analysis by measuring the zone of inhibition (Ansar et al. 2020). Ampicillin was used as a positive control. AgNPs dispersed in autoclaved double distilled water (25 µg/L and 50 µg/L), 1 mM silver nitrate, NSS extract, and ampicillin (positive control) are tested for their antibacterial property. The Petri plates are sealed with parafilm and incubated at 30°C for 24 hours. After the incubation time, the inhibition zone diameter (IZD) was measured.

3.5.7 Photocatalytic degradation of dyes using synthesised AgNPs

Using synthesised AgNPs, preliminary experiments were carried out to determine the best operating and light conditions for optimal dye degradation, and experiments were conducted under different light sources and in dark conditions. Experiments under dark conditions were carried out to assess the effect of adsorption alone, and the reaction time maintained for these trials was 3 hours; for degradation under light sources, samples were kept under the dark condition to give sufficient time for adsorption of the pollutants on AgNPs, and later the experiments were continued for 3 hours under different light sources to check the photocatalytic ability of the synthesised nanoparticles. The photocatalytic degradation study for RhB, RBBR and MV dye is done in the presence of sunlight, tungsten filament, LED light, CDM-R 70W and UVB light installed in a closed chamber setup. The setup used for the study is shown in Figure 3.2.

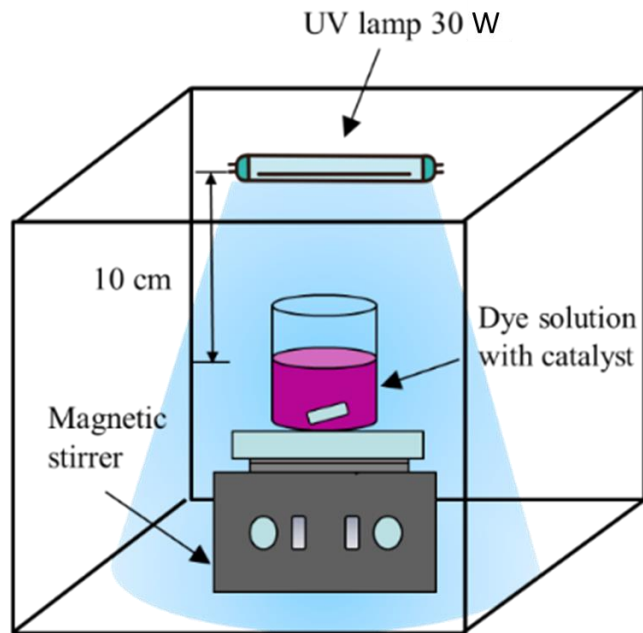


Figure 3.2 Photocatalytic experimental setup

The photocatalytic reaction is based on the separation and action of electron-hole pairs, which results in oxidation and reduction for the degradation of dyes (Alipour and Lakouraj 2019). Dye degradation capacity is carried out by adding 1 g/L AgNPs into an aqueous solution of RhB dye (10 mg/L), RBBR dye (100 mg/L) and MV (100 mg/L), aqueous solution. 2 mL of solution periodically was centrifuged at 10000 rpm for 5 min. The supernatant solution is then analysed in a UV-visible double-beam spectrophotometer at 250-800 nm. Photocatalytic degradation of AgNPs was determined by the equation (3.16):

$$\text{Photocatalytic degradation (\%)} = \left(1 - \frac{C_t}{C_0}\right) \times 100 \quad (3.16)$$

where C_0 and C_t are the concentrations of dye at an initial time and time t , respectively

3.5.8 Isotherm study for degradation of dyes

Isotherm models demonstrate the mechanism behind the affinity of dyes to the catalyst. This study uses the Langmuir, Freundlich and Temkin isotherm models (Eq. (3.3-3.5) (Bameri et al. 2022; Thomas and Thalla 2022) selected for fitting the experimental data. The parameters for each model are calculated from slope and intercept values in corresponding graphs.

3.5.9 Kinetic study for degradation of dyes

Photocatalytic degradation of pollutants will initiate in the presence of light if the pollutant is attached or available in nearby premises of the catalyst. So, to understand the photocatalytic ability of the nanoparticles in dye removal, first, we need to understand the adsorption capacity of nanoparticles on the dye (Abebe et al. 2018). The kinetic study reveals the relationship between adsorbate adsorbed on the adsorbent and adsorbate remaining in the solution at the time of equilibrium. The kinetic study for the photocatalytic removal of dyes is analysed with different models such as pseudo-first-order, pseudo-second-order, interparticle diffusion model and Elovich kinetic model (Eq. (3.7-3.10)) (Bameri et al. 2022; Far et al. 2022).

3.5.10 Dye degradation pathway studies

The degradation products were characterised by High-Resolution Liquid Chromatography Mass Spectrometer (HR-LCMS) (Xevo QToF, Waters, USA). Before and after treatment, the samples were filtered through a 0.45 μm syringe filter and injected into HRLC-MS for analysis. An electrospray ionisation source was used with a C18 column (50 mm x 2.1 mm, 1.7 μm). LC conditions used for the analysis are as follows, mobile phase A: Water and 20 mM ammonium acetate adjusted (pH 4 using acetic acid), mobile phase B: Acetonitrile, the flow rate of the mobile phase was 0.3 mL/min with an injection volume of 5 μL , column temperature of 40°C, capillary voltage: 2.5kV. The following gradient method is used for all analyses: 70% (A) for Initial time, 50% (A) from 0 to 0.25 min, 5-70% (A) from 0.25 to 2.68 min, and 70% (A) from 2.68 to 6 min (Cleland et al. 2015).

3.6 Utilisation of NSS lignin-based catalyst for dye degradation

This study discusses the in-situ preparation of magnetised silver particles bonded with lignin for the photocatalytic degradation of anionic, cationic and zwitterionic dyes.

3.6.1 Preparation of alkali-soluble lignin-based catalysts

3.6.1.1 Preparation of alkali-soluble lignin

Alkali soluble lignin is prepared by treating extractive-free NSS with 12% NaOH for two hours and precipitating with 1 N HCl (pH 2). Then the sample is centrifuged at 10000 rpm for 5 min and washed several times with distilled water to get the purest

form of alkali lignin. Lignin samples obtained are washed with Deionized water and dried at 50°C in a hot air oven for 12 hours and stored.

3.6.1.2 Preparation of magnetic iron oxide nanoparticles (Fe_3O_4)

One gram of $FeCl_3 \cdot 6H_2O$ and three gram of $FeCl_2 \cdot 4H_2O$ is dissolved in 100 ml of double distilled water at 70°C at 500 rpm for 1 hour. 5 mL of NSS extract is added to this solution and stirred the whole solution at 70°C at 500 rpm for 2 hours then NaOH solution is added to make the pH to 10. The precipitated nanoparticles are separated by a magnet and dried at 70°C up to constant weight.

3.6.1.3 Preparation of magnetised lignin (Fe/Lignin)

Two grams of lignin is dissolved in 100 mL of water by making the pH to 10. One gram of $FeCl_3 \cdot 6H_2O$ and three grams of $FeCl_2 \cdot 4H_2O$ are dissolved in 100 ml of double distilled water at 70°C at 500 rpm for 3 hours. After cooling the mixture to room temperature, Fe/Lignin precipitated by adding diluted HCl, separated by a magnet, and dried at 70°C.

3.6.1.4 Preparation of silver-coated lignin (Ag/Lignin)

Two grams of lignin is dissolved in 100 mL of water by adjusting the pH to 10 by adding sodium hydroxide. The solution is then added to 100 mL of 15 mM silver nitrate and stirred for 3 hours at 70°C. After cooling the mixture to room temperature, Ag/Fe/Lignin precipitated by adding 30% HCl, separated by a magnet, and dried at 70°C.

3.6.1.5 Preparation of magnetised silver-lignin composite (Ag/Fe/Lignin)

Two grams of lignin is dissolved in 100 mL of water by making the pH 10. One gram of $FeCl_3 \cdot 6H_2O$ and 3 g of $FeCl_2 \cdot 4H_2O$ are dissolved in 100 ml of double distilled water at 70°C at 500 rpm for 10 min. The obtained solution was added to the previous solution with 100 mL of 15 mM silver nitrate and stirred for 3 hours at 70°C. After cooling the mixture to room temperature, Ag/Fe/Lignin precipitated by adding 30% HCl, separated by a magnet, and dried at 70°C.

3.6.2 Characterisation of composites

The characterisation of Ag/Fe/Lignin composite by different techniques is listed in Table 3.3 (S. No: 5-9). And some other additional characterisation was also done as

follows: the potential of zero charges (pH_{pzc}) of nanocomposites was measured by the salt addition technique, Raman spectroscopy measurements were obtained using a Compact-Raman Spectrometer (Renishaw, UK), Vibrating sample magnetometer (VSM) is used to determine the magnetic properties of samples, photoluminescence (PL) spectroscopy is used to determine recombination effect of electron-hole pairs in materials, and after degradation of dyes the degraded products are analysed using HRLC-MS.

3.6.3 Preparation of dye solutions

To prepare 100 mg/L RBBR, RhB and MV, 0.1 g of dye was dissolved in 1L double distilled water. Then, 100 mg/L of each of the RBBR, RhB, and MV dyes are thoroughly mixed to prepare a solution with a 1:1:1 mixture of all three dyes.

3.6.4 Photocatalytic degradation of dyes using catalysts

Using synthesised composites, preliminary experiments were carried out to determine the best material for optimal dye degradation, and experiments were conducted under UV light sources after samples were kept under the dark condition to give sufficient time for adsorption; later, the experiments were continued to check the photocatalytic ability of the composites. The photocatalytic degradation study for RhB, RBBR and MV dye is done in the presence of UV light installed in a chamber setup (Figure 3.3). Dye degradation capacity is achieved by adding lignin composite into RhB dye, RBBR dye and MV with an initial concentration of 100 mg/L aqueous solutions. A magnet removes the catalyst, and the supernatant solution is analysed periodically in a UV-visible double-beam spectrophotometer at 250-800 nm. A photocatalytic degradation study was also done for a mixture of dye solutions, which was taken to analyse the effect of a mixture of dyes in textile industries with a combination of these three dyes in 1:1:1 proportion (100 mg/L each).

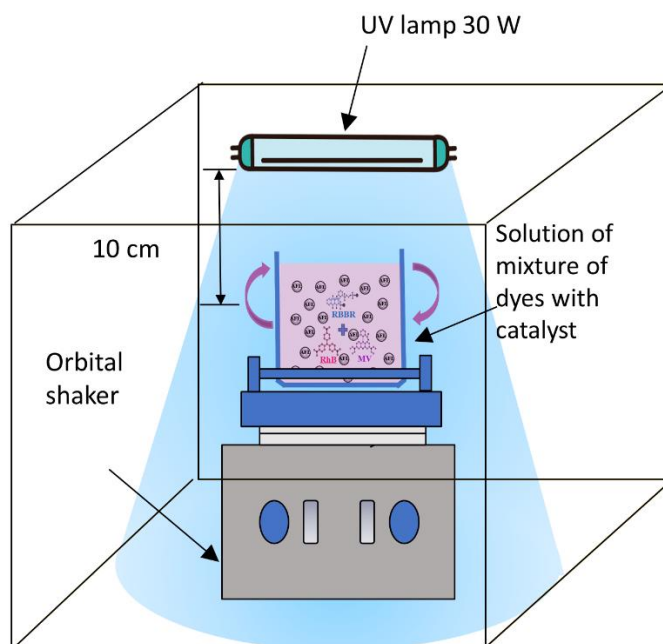


Figure 3.3: Photocatalytic experimental setup used for Ag/Fe/Lignin as the catalyst

3.6.5 Kinetic study and isotherm study for degradation of dyes using Ag/Fe/Lignin composite

In this study, the Langmuir, Freundlich and Temkin isotherm models (Eq. (3.3 -3.5) selected for fitting the experimental data for isotherm analysis. The kinetic study for the photocatalytic removal of dyes is analysed with different models such as pseudo-first-order, pseudo-second-order, interparticle diffusion model and Elovich kinetic model (Eq. (3.7 – 3.10)).

3.6.6 Reusability study for Ag/Fe/Lignin composite

A set of degradation-regeneration cycles, a study was performed to investigate the reusability of the catalyst. After each degradation process, the catalyst was recovered from treated water using an external magnet. The catalyst regeneration is done by washing with ethanol and drying it before the next experiment cycle.

CHAPTER 4

RESULTS AND DISCUSSIONS

4.1 General

The main substrate in the present study is NSS. This work investigates the effectiveness of textile dye removal utilising NSS-based materials.

4.2 Characterisation of biomass

As explained in section 3.3 (Table 3.2), Biomass characterisation is carried out. Proximate analysis test results show that the total solid content of NSS comprises fixed solids (38%) and volatile matter (50.03%). The fixed carbon yield for NSS is approximately the same as the coconut shell reported by Rout et al., (2016). Higher ash content for NSS indicates higher inorganic matter content (Silva et al. 2016). The ultimate analysis for the substrate is carried out using CHNS elemental analyser ELEMENTAR Vario EL III. The sample is exposed to a strongly oxidising environment to produce and detect the amount of N₂, C, H₂ and S. Table 4.1 lists the quantitative analysis of solids and ultimate analysis results for NSS. Carbon content (43.09%) in NSS is higher. The difference resulted in higher oxygen content, indicating the presence of other inorganic elements (Kabir Ahmad et al. 2021). Biochar prepared from dried NSS by 4 hours of treatment in a muffle furnace at 500°C resulted in 27.97% Biochar yield (based on the dry weight of NSS).

Biomass composition is determined by quantifying cellulose, hemicellulose, and lignin based on National Renewable Energy Laboratory (NREL) characterisation standards for different bio-samples of lignocellulose biomasses. NSS contains fewer extractives and high content of lignin, so this can be utilised for lignin-based studies. Table 4.2 lists the biomass composition of NSS. Another characterisation (XRD, TGA, FESEM and FTIR) of NSS is given in this report as a comparative study along with modified materials synthesised based on NSS.

Table 4.1 Quantitative analysis of solids in NSS

Parameter		NSS
Analysis of solids	Total solids (%)	88.03
	Moisture content (%)	11.97
	Fixed solids (%)	38
	Volatile solids (%)	50.03
	Ash content (%)	1.5
	Fixed carbon (%)	23
Ultimate analysis	N (%)	1.92
	C (%)	43.09
	S (%)	Not detected
	H (%)	4.87
	O (%)	50.12

Table 4.2 Biomass composition of NSS

Extraction	Extractives	Weight Percentage
Water extraction	starches, water-soluble such as simple sugars and some protein and ash, and dirt	1.6%
Ethanol extraction	Waxes and chlorophyll	1.2%
Acetone extraction	extractive-free biomass	0.8%
	Hemicellulose	9.78%
	Lignin content (extractive-free biomass)	60.75%

4.3 NSS biochar as an adsorbent for the removal of dyes

NSS and the biochar prepared from NSS are analysed with different techniques, as mentioned in section 3.4.1, Table 3.2. NSS biochar is used for the removal of three different dyes RBBR, RhB, and MV.

4.3.1 NSS biochar as an adsorbent for the removal of RBBR dye

NSS biochar is utilised for the RBBR dye removal, and its optimisation is carried out by Response Surface Methodology (RSM). Kinetic, isotherm and thermodynamic studies were conducted to determine the mechanism behind the adsorption process.

4.3.2 Characterisation of NSS and NSS biochar

Proximate analysis is carried out for NSS biochar; results show a total solid content of 92% with less moisture content of 8%. NSS biochar comprises fixed solids (66.5%) and volatile matter (33.5%). The characterisation of NSS and NSS biochar (before and after adsorption) is done to understand the effect of the adsorption phenomenon.

a) **FESEM analysis:** The morphology of the NSS powder and NSS biochar were investigated by FESEM microscopy. The image of the whole NSS is shown in Figure 4.1a. FESEM image of dried NSS powder used for the study with 200 magnification is shown in Figure 4.1b, and 200 K magnification is shown in Figure 4.1c. It is evident from the FESEM micrograph that the grain size of NSS (Figure 4.1 b) and NSS biochar (Figure 4.1d) is estimated to be 10-100 μm size. NSS biochar holds micropores of size ranging from 1.559- 8.887 μm (Figure 4.1e) and even nanopores of 238 nm (Figure 4.1 f). Carbonation of material makes more surface area and pore size to the material; in that sense, NSS will be an effective material for various applications in the form of biochar (Waheeb et al. 2020). The FESEM micrographs of the NSS biochar (Figure 4.1 f) and NSS biochar after adsorption (Figure 4.2 g) show micro-level changes to the surface.

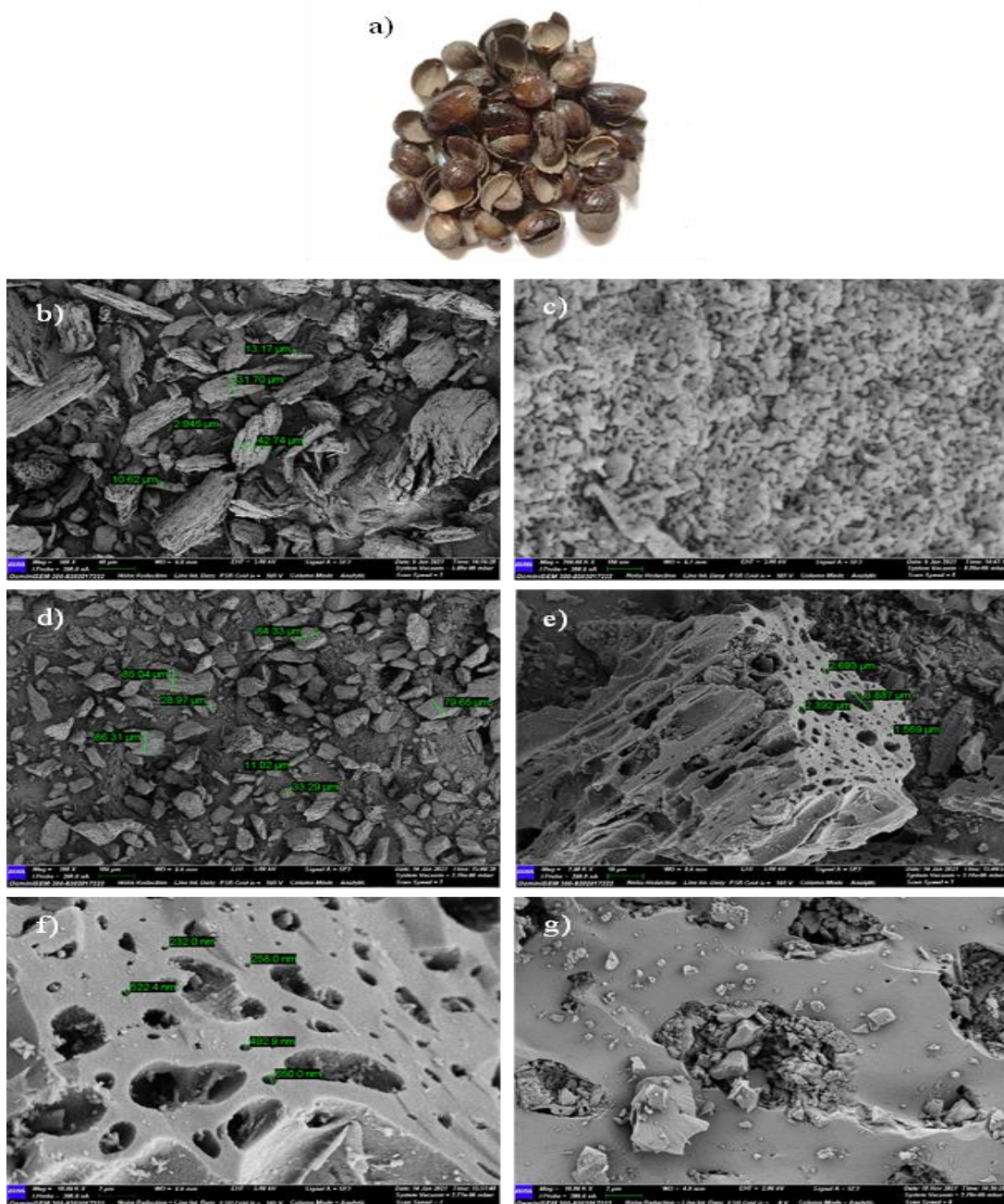


Figure 4.1 a) Dried NSS b) FESEM image of dried (105°C) NSS powder c) NSS powder with 200 K magnification d) FESEM image for NSS biochar e) NSS biochar with micropores (2 K magnification) f) NSS biochar with nanopores (10 K magnification) g) NSS biochar after adsorption

b) **TGA analysis:** TGA analyses thermal stability and degradation of NSS under a nitrogen atmosphere. The TGA analysis graph indicates the weight loss percentage with the temperature rise. DTG graph shows derivative thermogravimetric analysis with

respect to the temperature. Thermal degradation of NSS has a higher rate of weight reduction than NSS biochar, indicating the higher stability of NSS biochar from the TGA graph. NSS biochar had a weight reduction of 10%, whereas NSS reduced approximately 10% of weight within the temperature range of 30- 800 °C. DTG curve shows the stages of thermal degradation for NSS degradation, which happened mainly in a temperature range of 30- 115°C and 200- 335°C (Figure 4.2 a). An elevated temperature of more than 500°C changes the biomass into biochar (Vannarath and Thalla 2021). In the case of NSS biochar, about 10% weight loss was taken place at the initial temperature range of 30- 400°C, and then a gradual decrease in weight happened up to 630°C (Figure 4.2 b). From the temperature range of 673°C – 800°C, a sudden reduction of 4.23% in weight took place in the case of NSS biochar.

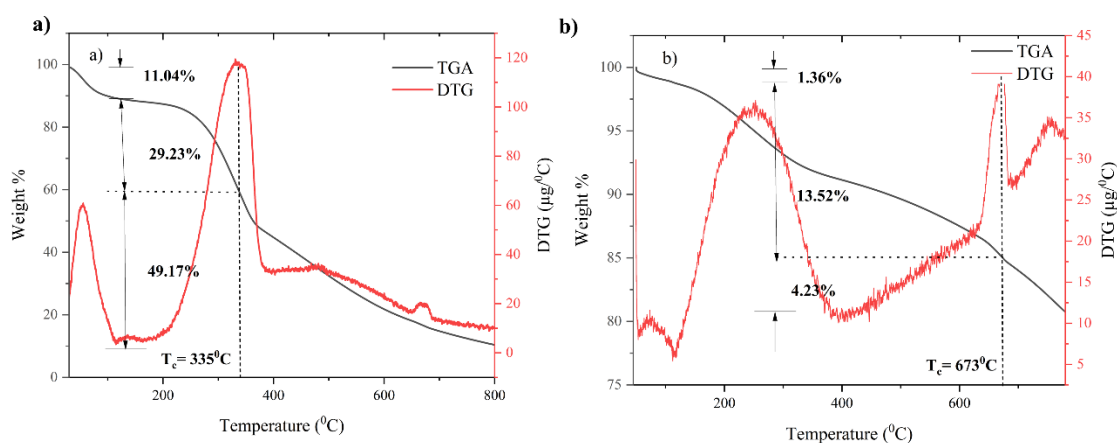


Figure 4.2 DTG and TGA curve for a) NSS and b) NSS biochar

c) **XRD analysis:** XRD peak analysis of NSS by expert high-score software suggested the presence of major crystalline peaks at $2\theta = 26.507^\circ$ (020 plane), which represents vanillin's ($C_8H_8O_3$) presence (Amal et al. 2017; Mustikasari et al. 2015) (Figure 4.3a). The peak at $2\theta = 26.543^\circ$ (002) indicates the presence of graphite in the NSS (Suzuki et al. 2020). In the case of NSS biochar, the XRD pattern has a shift in some of the peaks, and in that $2\theta = 29.369^\circ$ which is assigned to lattice plane of 104, which indicates the presence of $Ca_6C_6O_{18}$ which is calcite (Ahmad et al. 2020b) (Figure 4.3b). The effect of RBBR adsorption on NSS biochar is indicated by peak shifts and variations in peak intensities (Figure 4.3c).

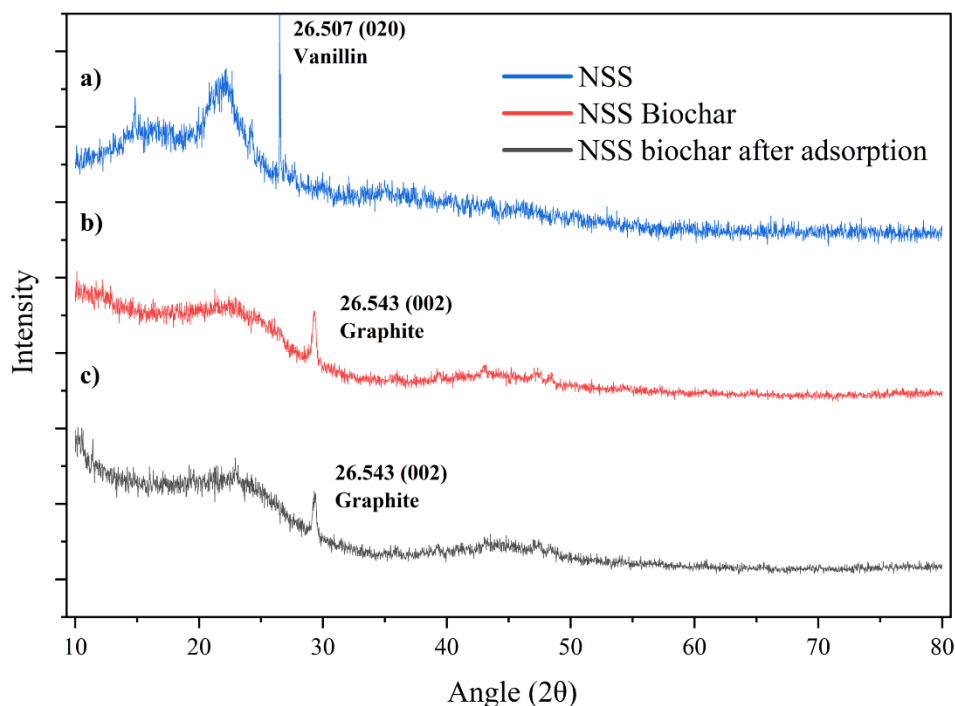


Figure 4.3 XRD pattern for a) NSS b) NSS biochar c) NSS biochar after adsorption

d) **FTIR analysis:** FTIR spectrum for NSS powder and NSS biochar (before and after adsorption) were analysed by FTIR (PerkinElmer Spectrum Version 10.4.2) using the KBr method (Figure 4.4) to determine the nature of functional groups. The functional groups present in NSS powder, and NSS biochar (before and after adsorption) are listed in Table 4.3. FTIR spectra for NSS powder (Figure 4.4a) show peaks for hydroxyl, amide, ester, aldehydes, ketones, and aromatic C-H groups. O-H functional group indicates a wavenumber of 3639 cm^{-1} for NSS powder and 3698 cm^{-1} for NSS biochar after adsorption (Figure 4.4c). The peaks at wavenumbers 2870 cm^{-1} , 2644 cm^{-1} , and 3019 cm^{-1} indicate alkyl groups, C-H bonding in NSS powder, NSS biochar and NSS biochar after adsorption. Peaks at $1500\text{--}900\text{ cm}^{-1}$ indicate a functional group with C-O bonding due to the presence of a non-ionic carboxylic group (Barka et al. 2013; Lewis et al. 2019). The existence of an aromatic ring with C=C stretching shows peaks at 1488 cm^{-1} , showing the characteristic of quinone presence in NSS biochar (Figure 4.4 b) (Wang et al. 2016). The shift in the peaks for NSS biochar from NSS powder shows the changes due to the carbonation for the preparation of biochar. A strong C - H bending appeared after the adsorption of

RBBR on NSS biochar at wavenumber 833 cm^{-1} . The shift in the peaks for NSS biochar (before and after adsorption) indicates the changes accrued by the adsorption of RBBR dye on the biochar surface (Table 4.3).

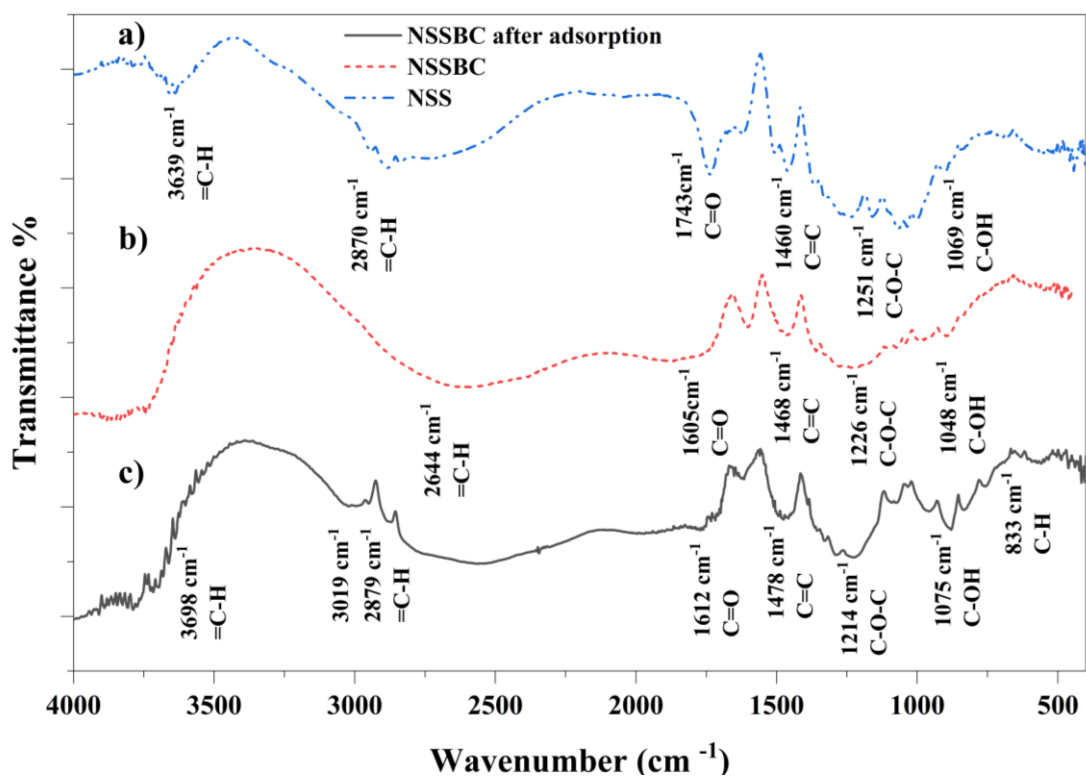


Figure 4.4 FTIR spectra of a) NSS b) NSS biochar c) NSS biochar after adsorption

Table 4.3 FTIR spectra bands for NSS, NSS biochar and NSS biochar after adsorption

Assignment	Band position (cm^{-1})		
	NSS	NSS biochar	NSS biochar after adsorption
O –H stretching of the hydroxyl group	3639	-	3698
= C – H stretching	2870	2644	3019
C = O stretching of amide ester, ketones and aldehydes group	1743	1605	1612

C=C aromatic	1460	1488	1478
C-O-C stretch	1251	1226	1214
C-OH stretch	1069	1048	1075
Strong C – H bending	-	-	833

4.3.3 Response surface methodology-based optimisation of RBBR dye removal using NSS biochar

The Response Surface Methodology (RSM) optimization is done with the help of software, design expert- 13. Box-Behnken Design (BBD) is utilised for the determination of optimum removal efficiency in RSM. The influence of each parameter on the adsorption characteristics of dye by NSS biochar was analysed by different initial RBBR concentrations (range 5 – 100 mg/L) at varying dosages of 0.5- 3 g/L, room temperature, solution pH varied 2- 12, and for a contact time of 10- 120 min with a solution volume taken was 100 mL. The list of experiments done with the help of design expert software and its set experimental values are listed in Table 4.4.

Table 4.4 The experimental data for RBBR dye removal

	Factor 1	Factor 2	Factor 3	Factor 4	Response 1
Run	A: Concentration	B: Contact time	C: pH	D: Dosage	Percentage removal
	mg/L	min		g/L	%
1	52.5	65	7	1.75	84.680
2	52.5	10	2	1.75	81.369
3	100	65	7	0.5	70.325
4	52.5	65	7	1.75	84.690
5	52.5	120	2	1.75	83.050
6	52.5	65	2	0.5	75.044
7	52.5	65	12	3	93.689
8	100	65	12	1.75	82.000
9	52.5	120	7	3	91.448
10	5	120	7	1.75	84.480

11	52.5	65	7	1.75	84.680
12	52.5	65	7	1.75	84.684
13	52.5	65	2	3	85.698
14	52.5	120	12	1.75	88.720
15	52.5	10	7	0.5	74.810
16	5	65	12	1.75	90.200
17	100	65	2	1.75	75.698
18	52.5	120	7	0.5	75.000
19	52.5	10	7	3	83.207
20	5	65	7	0.5	77.950
21	100	120	7	1.75	85.639
22	52.5	65	12	0.5	78.387
23	5	65	7	3	86.939
24	5	65	2	1.75	89.568
25	5	10	7	1.75	87.750
26	52.5	10	12	1.75	83.050
27	100	10	7	1.75	76.570
28	100	65	7	3	85.634
29	52.5	65	7	1.75	84.690

4.3.3.1 Analysis of variance for RBBR dye removal

The effect of the parameters and their interaction influencing RBBR removal efficiency was determined using the quadratic model by analysis of variance (ANOVA). ANOVA results (Table 4.5) of the RBBR dye removal show a model with an F value of 22.83, and a p-value < 0.0001 indicates a 0.01% chance of noise. P-value < 0.0500 indicates that the terms of the model are significant. The sum of squares indicates the importance of terms in the model. Thus, the adsorbent dosage has higher importance (sum of squares= 469.99) followed by concentration, pH, and contact time (Zhang et al. 2011). The correlation coefficient (R^2) for the model is 0.958, showing 95.8% of this process and predicted and experimental values have a higher correlation (Leal et al. 2010). Thus the equation can be utilised to predict the RBBR efficiency (Eq. (4.1)).

$$\begin{aligned} \text{Percentage removal} = & 84.11174 - 0.190170 A - 0.075176 B - 0.843548 C + 6.775644 \\ & D + 0.001181AB + 0.005968 AC + 0.026611 AD + 0.003626 BC + 0.0029276 BD - \\ & 1.85920 CD - 0.000447 A^2 - 0.000236 B^2 + 0.028294 C^2 - 1.81466 D^2 \end{aligned} \quad (4.1)$$

Table 4.5 ANOVA table for RBBR dye removal

Source	Sum of Squares	df	Mean Square	F-value	p-value	Remarks
Model	851.61	14	60.83	22.83	< 0.0001	Significant
A-Concentration	140.23	1	140.23	52.63	< 0.0001	Significant
B-Contact time	38.81	1	38.81	14.57	0.0019	Significant
C-pH	54.69	1	54.69	20.53	0.0005	Significant
D-Dosage	469.99	1	469.99	176.4	< 0.0001	Significant
AB	38.06	1	38.06	14.29	0.0020	Significant
AC	8.04	1	8.04	3.02	0.1044	Not significant
AD	9.99	1	9.99	3.75	0.0733	Not significant
BC	3.98	1	3.98	1.49	0.2419	Not significant
BD	16.20	1	16.20	6.08	0.0272	Significant
CD	5.40	1	5.40	2.03	0.1764	Not significant
A ²	6.59	1	6.59	2.47	0.1382	Not significant
B ²	3.32	1	3.32	1.25	0.2833	Not significant
C ²	3.25	1	3.25	1.22	0.2883	Not significant
D ²	52.15	1	52.15	19.57	0.0006	Significant
Residual	37.30	14	2.66			
Cor Total	888.91	28				

Figure 4.5a shows actual and predicted values by the model. Based on the fitted mathematical model, the predicted-actual curve in RSM depicts the connection between the independent variables and the response variable. Figure 4.5b represents the normal probability versus externally studentized residuals, which shows whether

the residuals follow a normal distribution (Jawad et al. 2021). According to Figure 4.5b, the points lie along a straight line. As a result, it can be stated that they are normally distributed, indicating the independence of the residuals and the accuracy of the assumptions (Reghioua et al. 2021b).

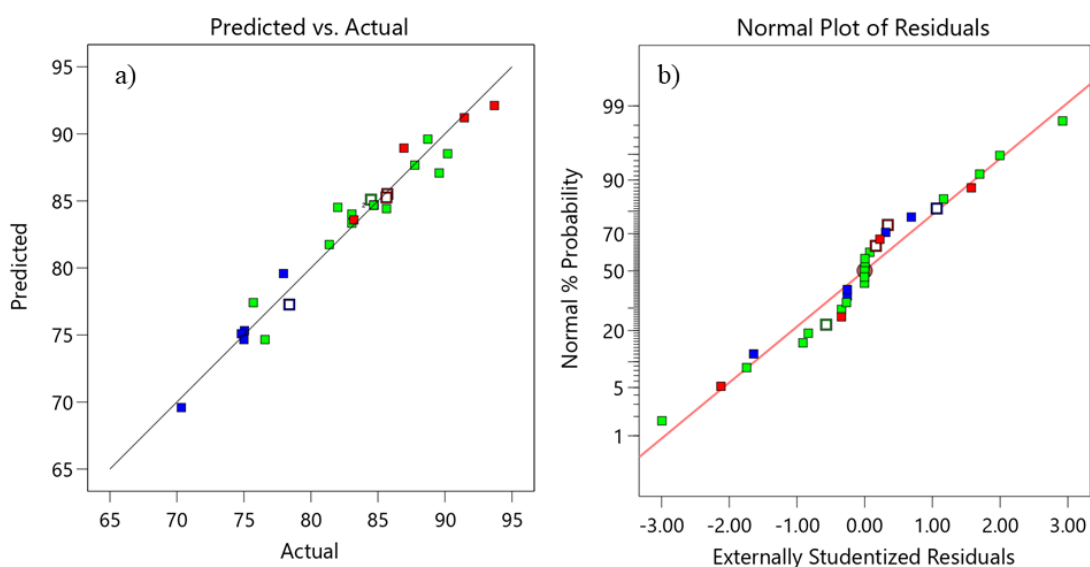


Figure 4.5 Graphs of a) Actual and predicted values b) Normal probability of the residuals

4.3.3.2 Effect of independent variables on adsorption

The contact time provided for the adsorption studies has a role in removal efficiency. Until it reaches equilibrium, the removal efficiency increase as the contact time increases. The analysis was done by keeping other parameters constant (initial concentration of 50 mg/L, pH of 7 and adsorbent dosage of 1.5 g/L), resulting in 84% removal efficiency at 120 min of contact time. The result revealed that adsorption occurs initially and then slightly increases with time. Electrostatic interactions with the active sites resulted in the fast adsorption of dye at less contact time (Lai 2021). A similar effect of the adsorption process is reported in Raj et al., (2021). The adsorption efficiency increases at the initial stage to get the active binding sites saturated, and a further increase in adsorption efficiency was negligible.

The effect of pH on the RBBR dye removal efficiency was analysed by varying pH values from 2 to 12. The experiment was conducted by keeping other parameters constant (initial concentration of 50 mg/L; 60 min contact time and adsorbent dosage

of 1.5 g/L). It shows that the pH of the solution influenced the binding sites and interaction between the RBBR dye molecules and NSS biochar. Adsorption capacity varies due to the modification of the surface charge of the adsorbent with respect to the pH (Zahoor and Ali Khan 2018). In an acidic medium, the binding sites of the adsorbent get saturated with protons. Thus, the dye molecules cannot attach to the binding sites, thus resulting in a lower efficiency of 82.3% (Saha 2010).

The initial concentration of RBBR dye significantly impacts the final removal efficiency of RBBR dye using NSS biochar. For 1.5 g/L adsorbent dosages, neutral pH, and 60 min contact time, the efficiency was found to be 89.5% at 5 mg/L of initial concentration, whereas it was 78.2% at 100 mg/L. A given mass of adsorbent can only remove a specific quantity of adsorbate from the solution (Gautam et al. 2015). The results specify that if the initial concentration is high, the efficiency will be less due to the saturation of the active sites with the adsorbates (Hii 2021). At low initial concentrations, the ratio of active sites on adsorbent with respect to dye molecule is high, which promotes all the dye molecules to interact with biochar and results in higher removal efficiency. The rapid adsorption of dye occurred in the initial stage due to its electrostatic interactions with active sites and a stronger mass transfer driving force. (Jiang et al. 2019).

The effect of the adsorbent dosage on the removal efficiency of RBBR dye was investigated by keeping other parameters constant (Initial concentration: 50 mg/L, pH: 7, Contact time: 60 min). The adsorbent dosage should be provided according to the initial dye concentration in the solution (Barka et al. 2013). The minimum efficiency (75.89%) was observed at less dosage of 0.5 g/L, and the maximum removal efficiency (87.86%) was at a higher dosage of 3 g/L. The increased efficiency with the adsorbent dosage is due to more active sites (Mary Ealias and Saravanakumar 2018). RBBR dye removal efficiency at an adsorbent dosage of 2 g/L was about 85.87%, and further increment with dosage has not resulted in a significant increase in removal efficiency. A similar trend of removal efficiency with respect to the adsorbent dosage is also observed in Rahmat et al., (2016). The negligible change in removal efficiency with adsorbent dosage (> 2 g/L) is due to the insufficient amount of dye in the solution with respect to the adsorbent dosage. The removal efficiency can also reduce due to the

unsaturation of available sites due to the agglomeration of adsorbent (Morosanu et al. 2019; Saha 2010).

Figure 4.6 shows the variations in efficiency with respect to AB (Figure 4.6 a), and DB (Figure 4.6 b) interactions represented by 3D and contour plots are shown in Figure 4.6. The graph shows the adsorbent successfully removed RBBR dye. Adsorption efficiency increases with adsorbent dosage. Interactions show that a higher concentration of dye negatively impacts the removal efficiency. The same pattern is shown in similar previous studies of RBBR removal (Yonten et al. 2016). The optimum conditions for RBBR adsorption were an initial concentration of 100 mg/L, pH of 10, an adsorbent dosage of 2.85 g and a contact time of 110 min with RBBR removal efficiency (93.41%).

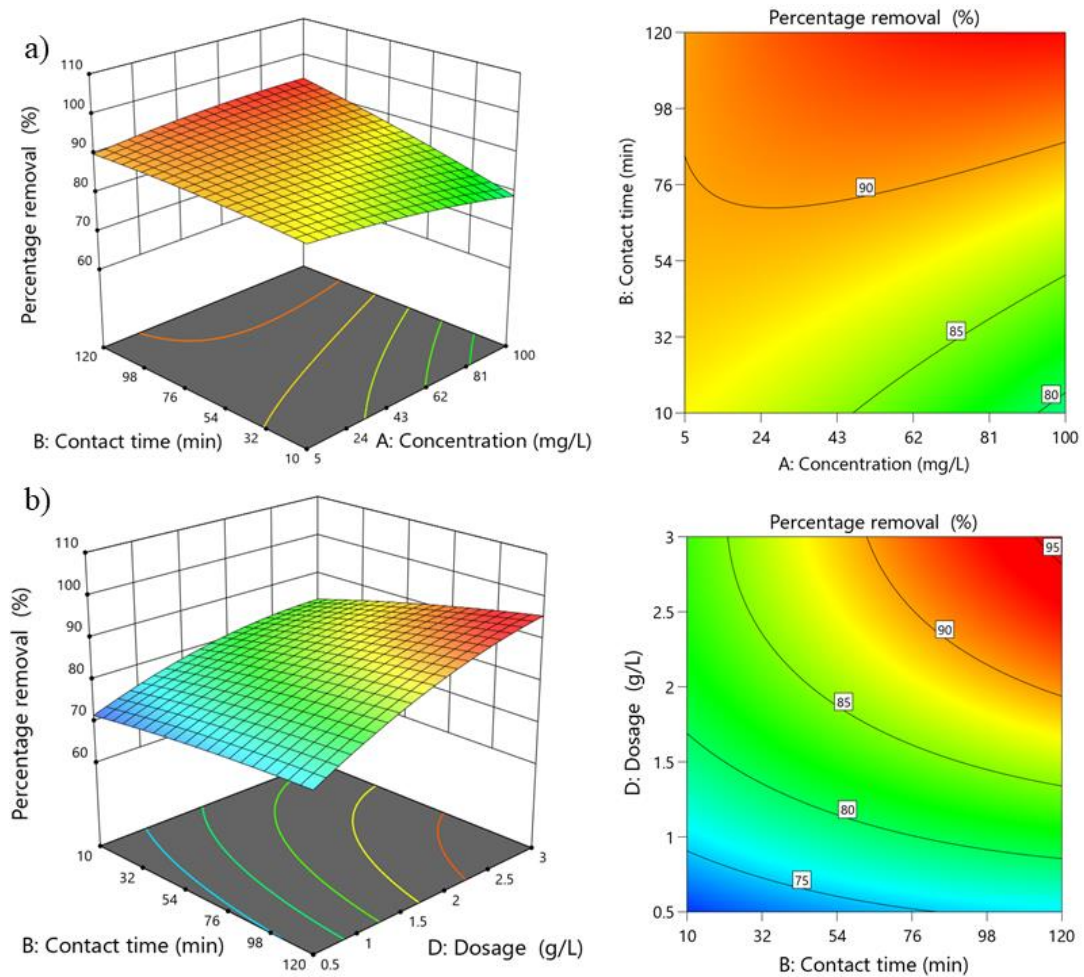


Figure 4.6 3D and contour plots of a) AB interactions on RBBR removal b) DB interactions on RBBR removal

4.3.4 Adsorption isotherm for RBBR dye removal using NSS biochar

The dye removal efficiency at varying initial concentrations (10 mg/L- 100 mg/L), and 0.1 g of adsorbent dosage were determined at pH 7 to conduct an isotherm study. The adsorption isotherm shows that initially, adsorption sites can capture the RBBR dye due to the availability of unsaturated active sites (Figure 4.7a). This is due to the availability of sites on the adsorbent (Gokulan et al. 2019). The Langmuir isotherm model shows a higher correlation coefficient ($R^2 > 0.999$) compared to the Freundlich isotherm ($R^2 > 0.992$) and Temkin isotherm ($R^2 > 0.949$), which confirms that the absorption process is fit with the Langmuir isotherm model, and it follows monolayer adsorption (Barka et al. 2013; Silva et al. 2016) (Table 4.6).

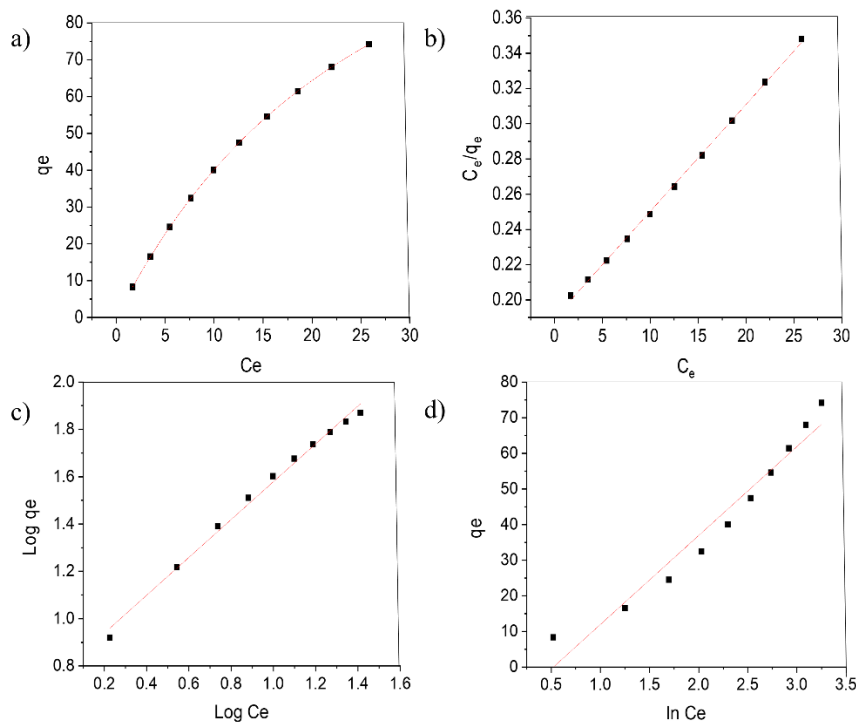


Figure 4.7 a) Adsorption isotherm of RBBR onto NSS biochar b) Langmuir adsorption isotherm model c) Freundlich adsorption isotherm model d) Temkin adsorption isotherm model

From the isotherm graphs, it is evident that Langmuir isotherm (Figure 4.7b) values are closer to the line than Freundlich isotherm (Figure 4.7c) and Temkin isotherm (Figure 4.7d). Langmuir isotherm model shows a maximum monolayer adsorption capacity of 173.31 mg/g, much more than RBBR removal using activated carbon derived from coconut shells. The R_L values in Table 4.7 indicate that the

adsorption process is favourable and spontaneous ($0 < R_L < 1$). The lowest value of R_L at a higher concentration shows that Langmuir adsorption isotherm is better at a higher concentration (Hii 2021).

Table 4.6 Parameters of the isotherm models for RBBR dye adsorption onto NSS biochar

Adsorption isotherm	Parameter	Value
Langmuir	q_{\max} (mg/g)	173.310
	K_L (L/mg)	0.030
	R^2	0.999
Freundlich	K_F (L/mg)	6.018
	n	1.250
	R^2	0.992
Temkin	K_T (L/mg)	0.593
	B_T (J/mol)	24.991
	R^2	0.949

Table 4.7 R_L values for adsorption of RBBR on NSS biochar based on the Langmuir model

Concentration (C_0) (mg/L)	10	20	30	40	50	60	70	80	90	100
R_L	0.77	0.62	0.53	0.45	0.40	0.34	0.32	0.29	0.27	0.25

4.3.5 Adsorption kinetics for RBBR dye removal using NSS biochar

The current kinetic study of the adsorption process was conducted with 0.1 g of NSS biochar to 100 mL RBBR solution (75 mg/L) with different time periods (10 - 120 min). The graph of adsorption capacity and time in Figure 4.8a shows that at the initial time, the adsorption rate was more due to the abundant active sites; with time, the adsorption gradually increased (Gokulan et al. 2019).

The adsorption process was analysed using kinetic models like intraparticle diffusion, pseudo-first-order, pseudo-second-order and Elovich kinetic models. The correlation coefficient (R^2) shows that the adsorption process is more fit to the pseudo-second-order model ($R^2 = 0.999$). From the isotherm graphs, it is evident that pseudo-second-order (Figure 4.8c) values are in line with than pseudo-first-order (Figure 4.8b), intraparticle diffusion model (Figure 4.8d) and Elovich kinetic model (Figure 4.8 e). The findings indicate that the process is chemisorption in nature (Table 4.8) (Reghioua et al. 2021b).

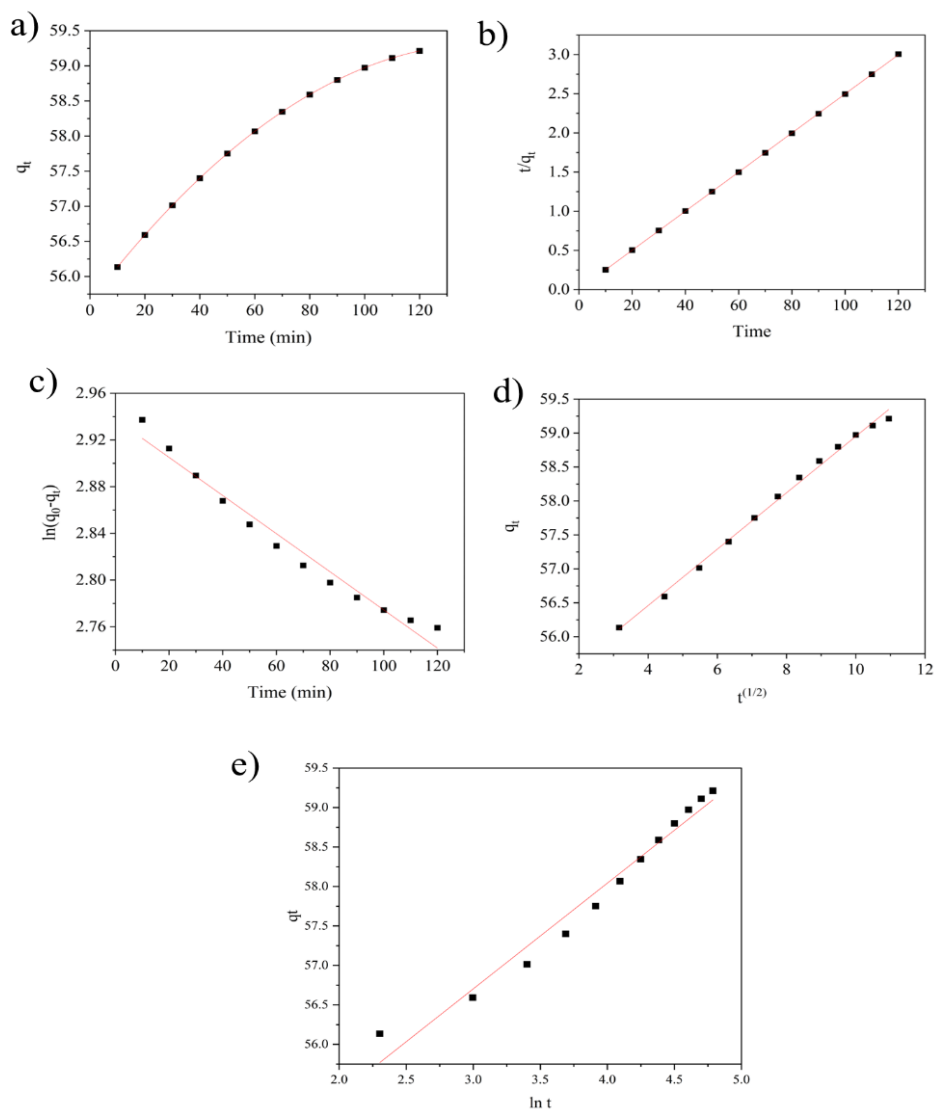


Figure 4.8 Kinetic plots of a) adsorption kinetics b) Pseudo-first-order model c) Pseudo-second-order model d) Intraparticle diffusion model e) Elovich kinetic model

Table 4.8 Parameter values of kinetic models

Kinetic model	Parameter	Value
	$q_{e, exp}$ (mg/g)	59.213
Pseudo-first-order model	$q_{e, cal}$ (mg/g)	18.873
	k_1 (min ⁻¹)	0.002
	R^2	0.969
Pseudo-second-order model	$q_{e, cal}$ (mg/g)	59.666
	K_2 (g/mg·min)	0.012
	R^2	0.999
Intraparticle diffusion model	k_{diff} (mg/g·min ^{1/2})	0.415
	C (mg/g)	54.798
	R^2	0.996
Elovich Kinetic model	α (mg/g/min)	0.120
	B (g/mg)	0.740
	R^2	0.960

4.3.6 Thermodynamic study for RBBR dye removal using NSS biochar

Adsorption tests with varying temperatures from 30°C to 45°C by keeping other experimental conditions constant were conducted to determine the influence of temperature on RBBR dye removal (adsorbent dosage: 1.5 g/L, initial concentration: 50 mg/L, contact time: 60 min and pH: 7). The dye removal efficiency does not significantly increase even at higher temperatures. Adsorption can be performed even at normal room temperature, which will be more feasible than the adsorption process at higher temperatures. The influence of adsorption temperature on dye removal capacity was examined using the thermodynamic parameters (Table 4.9).

The spontaneous nature of the dye adsorption process is represented by ΔG value at different temperatures. The increase in the negative values of ΔG with respect to the rise in temperature shows that the adsorption process can occur even at lower

temperatures (Raj et al. 2021). The graph between the natural log of K_d ($\ln K_d$) and $1/T$ resulted in the calculation of entropy and enthalpy values for the thermodynamic study (Figure 4.9). A positive value for the ΔH^0 indicates that the adsorption process is endothermic (Gautam et al. 2015). The entropy value indicates the increase in disorder in the adsorption process. A positive value of ΔS^0 (34.696 kJ/molK) in this study indicates the randomness and higher degree of freedom of adsorbate (Suteu et al. 2010).

Table 4.9 Thermodynamic parameters for RBBR dye adsorption on NSS biochar

$T(K)$	ΔG (kJ/mol)	ΔH^0 (kJ/mol)	ΔS^0 (kJ/molK)
303	-3.769	6.702	34.696
308	-4.064		
313	-4.129		
318	-4.323		

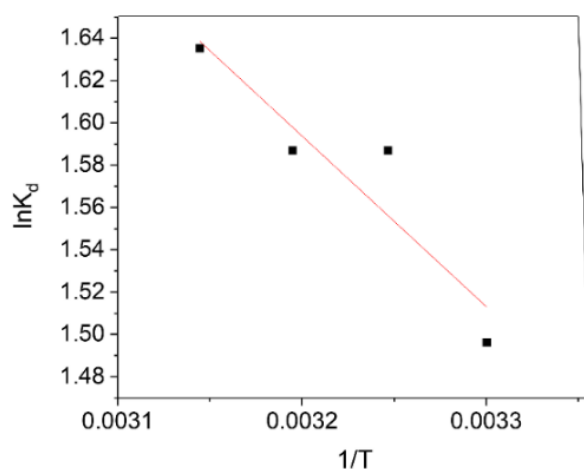


Figure 4.9 Von't Hoff plot for thermodynamic studies

4.3.7 Performance evaluation of NSS biochar as an adsorbent for the removal of dyes

NSS biochar is also analysed for other dyes like RhB and MV. The efficiency obtained in the case of RBBR dye is not reflected in the case of the other two dyes, even at lower initial dye concentrations. The effect of parameters like dosage (Figure 4.10a), time (Figure 4.10b), concentration (Figure 4.10c), and pH (Figure 4.10d) are analysed for all three dyes in the case of NSS biochar-based adsorption.

For RBBR dye removal using NSS biochar, the increase in the dosage (up to 2g/L) resulted in up to 91% removal efficiency (Initial concentration of 50 mg/L) in three hours, but in the case of MV dye (Initial concentration of 50 mg/L) resulted in 32% and for RhB, even for lower concentration as 10mg/L resulted in 55% (Figure 4.10a). A contact time of 3 hours has not resulted in a better adsorption efficiency, especially for RhB and MV dyes (Figure 4.10b). Studies on the effect of initial concentration show that RhB and MV are not effectively removed even for a very low initial concentration of 10 mg/L, whereas in the case of RBBR dye resulted in comparatively better removal efficiency using NSS biochar (Figure 4.10c). The effect of pH on dye removal shows that RBBR dye removal is more efficient at neutral pH. But in the case of MV dye, due to the presence of positively charged sites of NSS biochar in an acidic medium, it resulted in lower removal efficiency at lower pH, but in an alkaline medium, it resulted in comparatively higher removal efficiency (Figure 4.10d) (Saha 2010). As a result, RBBR dye removal is better than the other two dyes in NSS biochar-based adsorption.

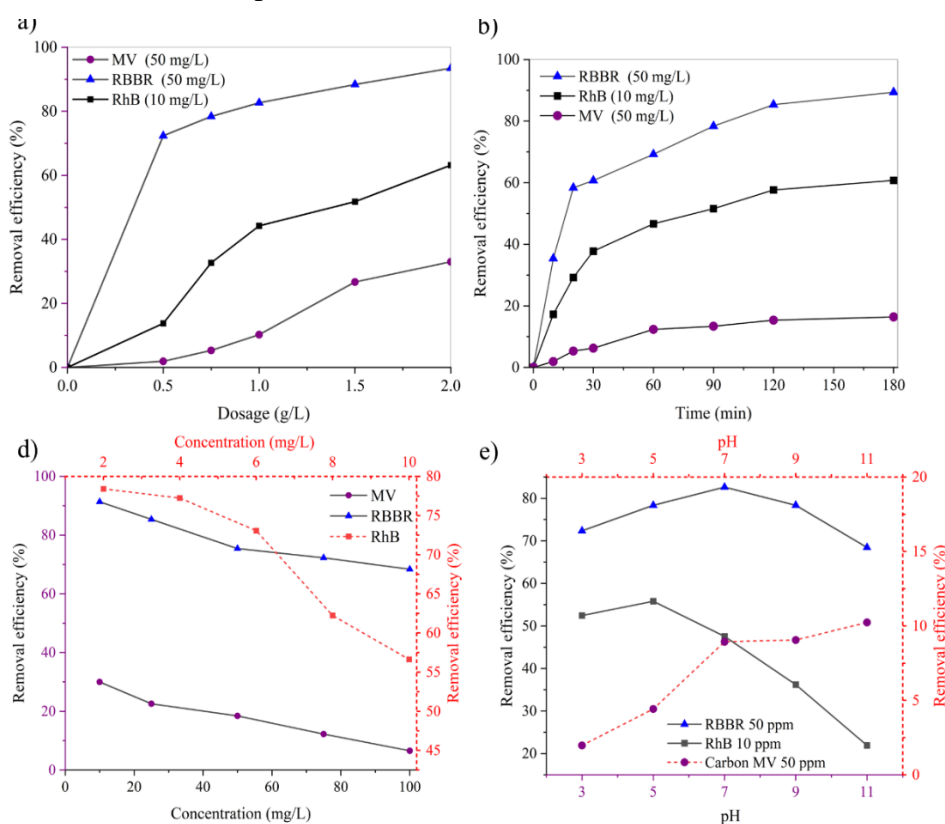


Figure 4.10 The effect of a) time b) pH c) Dosage and d) Initial dye concentration on RhB dye, RBBR dye and MV dye degradation

4.4 Synthesis of AgNPs using NSS extract: its characterisation and application in photocatalysis-based dye removal

4.4.1 Characterisation of NSS aqueous extract

Tests for phytochemical compounds in aqueous extract of NSS show the presence of alkaloids, saponins, flavonoids, polyphenols, phlobatannins, tannins, and terpenoids and the absence of quinones and steroids in the extract (Table 4.10). Alkaloids, phenols, flavonoids, and tannins act as biological antioxidants, which form anionic radicals and reduce the salts to their nano size (Mukunthan and Balaji 2012). The total phenolic content in the NSS extract was 17.89 mg GAE/g. Phenolic, alkaloids and flavonoid contents in extracts can act as the reducing and capping agents in nanoparticle synthesis (Sasidharan et al. 2020).

Table 4.10 Phytochemical analysis of NSS extract

Phytochemical compound	Name of test	Response	Reference
Alkaloids	Wagner's test	Positive	(Widjanarko et al. 2014)
Saponins	Frothing Test	Positive	(Saxena 2012)
Flavonoids	Ammonia test	Positive	(Velsankar et al. 2020b)
Polyphenols	Ferric cyanide test	Positive	(Velsankar et al. 2020b)
Phlobatannins	HCl test	Positive	(Auwal et al. 2014)
Tannins	Ferric chloride test	Positive	(Auwal et al. 2014)
Terpenoids	Salkowki's test	Positive	(Velsankar et al. 2020b)
Quinones	Alcoholic KOH test	Negative	(Rizwan et al. 2020)
Steroids	Sulfuric acid test	Negative	(Saxena 2012)

4.4.2 Synthesis of AgNPs

NSS extract (Figure 4.11a), when added to 1 mM silver nitrate solution (5% v/v) (Figure 4.11b) and kept under sunlight, the formation of AgNPs is visually confirmed by the colour change from pale brown to dark brown (figure 4.11c). The increment in colour intensity represents the synthesis of AgNPs (Malini et al. 2019). The formation of AgNPs is confirmed by checking the surface plasmon peak using a UV-visible double-beam spectrophotometer using a quartz cell of 10 mm path length and a spectral range of 200–800 nm. The reduction of silver from Ag⁺ ions to the Ag⁰

state was subjected to spectral analysis. The surface plasmon band of the reaction mixture was obtained at 470 nm (visible region) for AgNPs (Figure 4.11d).

Different amounts of the NSS extract (1%, 3%, 5%, 7% and 10%) in 1 mM $\text{Ag}(\text{NO}_3)_2$ solution under sunlight are tested to determine the effect of NSS extract amount in the synthesis of AgNPs by bio-reduction and stabilisation process. The samples are analysed by UV- visible spectrophotometer after 30 minutes (Figure 4.11e). UV-visible spectrophotometer analysis showed an intense peak for 5% of the extract in silver nitrate solution indicating the formation of a higher quantity of AgNPs.

The impact of silver nitrate concentration was studied by synthesising AgNPs with 5 mL extract with 100 mL of different concentrations of silver nitrate solution (1 mM, 5 mM, 10 mM, 15 mM and 20 mM) for 30 min (Figure 4.11f). The results show that as the concentration of silver nitrate increases, the peak intensity increases. The effect of pH on AgNP synthesis is studied by varying pH (2-11) with constant silver nitrate concentration (1 mM), contact time (30 min) and 5mL NSS extract (Figure 4.11g). The UV spectrum results show that the peak intensity increases with pH. This can be due to the change in the reducing ability of biomolecules with the pH variations (Mosaviniya et al. 2019) and thus affects the size of synthesised nanoparticles. The increase in the peak intensity indicates the formation of more nanoparticles with time. Thus alkaline range shows a better quantity of nanoparticles (Khalil et al. 2014).

The effect of contact time on the bio-reduction and stabilisation of nanoparticles was studied at different contact times (5 min -2 hours) with constant pH of 8, 100 mL of 1 mM of silver nitrate and 5 mL of the extract (Figure 4.11h). With the increment in the incubation time, the intensity of the peak increases, which means the quantity of AgNPs synthesised increases over time (Khalil et al. 2014). As a result, the green production of AgNPs using NSS extract is stable and produces more nanoparticles as an increase in incubation time in an alkaline state.

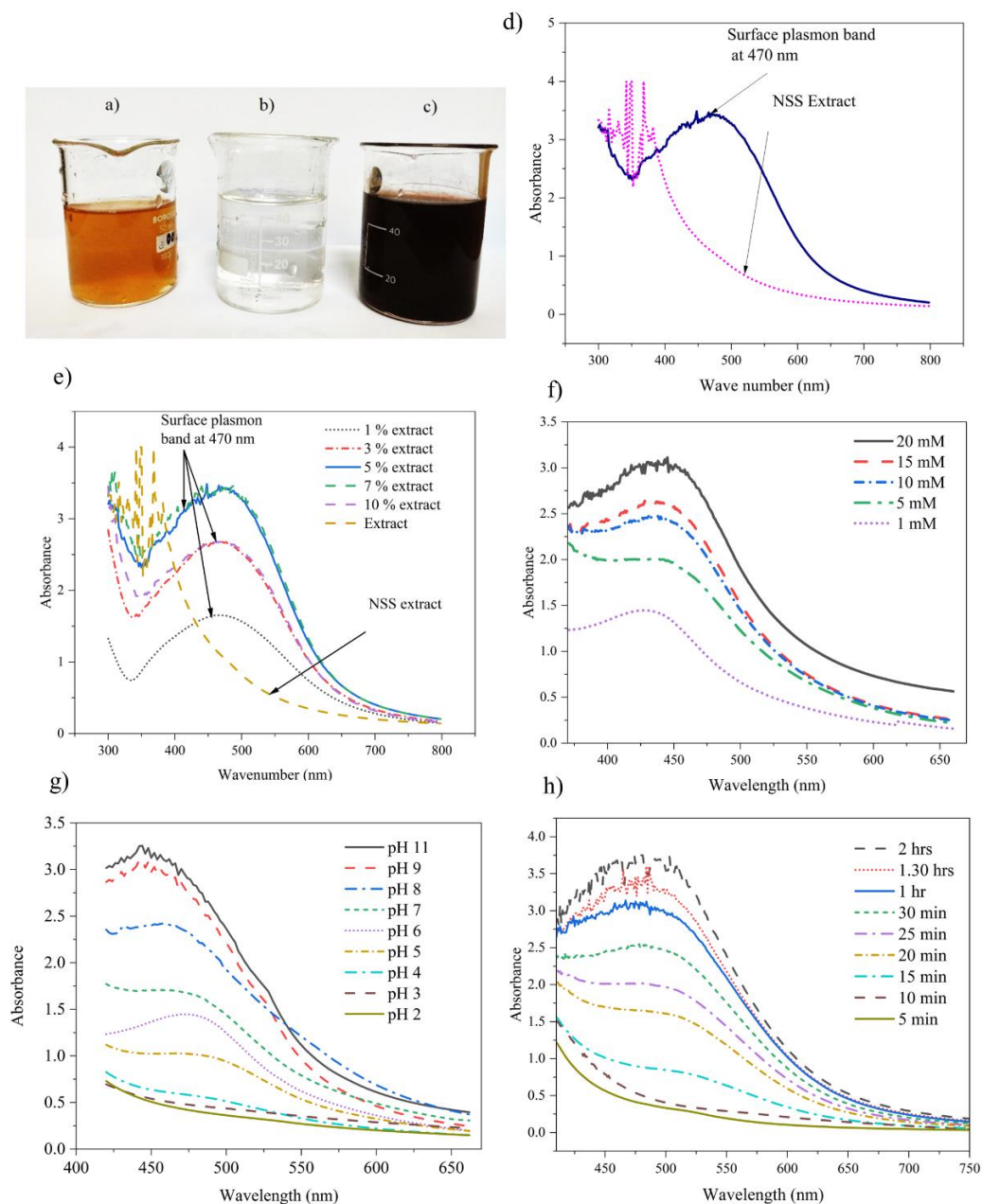


Figure 4.11 AgNP synthesis using NSS extract: a) NSS extract b) silver nitrate solution c) Colour change due to the formation of nanoparticles d) UV visible spectrum for AgNPs and NSS extract e) Effect of amount of extract f) Effect of concentration silver nitrate solution g) Effect of pH h)Effect of contact time

4.4.3 Characterisation of AgNPs

Small-angle x-ray scattering (SAXS) for the reaction mixture is done to confirm the formation of AgNPs in the aqueous solution and the particle size distribution. SAXS analysis is done for synthesised nanoparticles in extract and background as NSS extract.

The EasySAXS software can analyse the particle size distribution of synthesised AgNPs. The data is processed by subtracting the effect of extract from the solution so that the AgNP analysis can be done by fitting the data using the software. The graph plot against the amplitude of the scattering vector ($q = (4\pi\sin\theta)/\lambda$, where λ = wavelength of x-ray; 2θ = scattering angle) and intensity (figure 4.12 a) is processed and fitted using software to get the particle size distribution curve of synthesised nanoparticles (Figure 4.12 b). The synthesised nanoparticle has an average size of 23.5 nm from the results.

XRD patterns for green synthesised AgNPs are analysed by Malvern Panalytical's HighScore plus software. The peaks were observed at the 2θ range of 27.840° , 32.853° , 37.733° , 46.264° , 57.520° , 63.748° and 76.515° , corresponding to the Bragg's reflection planes 112, 020, 111, 022, 222, and 131, which represent AgNPs in the cubic crystal lattice (JCPDS No: 96-901-3047) (Aravind et al. 2021) (Figure 4.12c). The mean particle size of synthesised AgNPs was determined using Debye–Scherrer formula (eq. 4.2),

$$D = \frac{K\lambda}{\beta\cos\theta} \quad (4.2)$$

Where, K is Scherrer's constant taken as 0.94; λ is X-ray wavelength; β is halfwidth of the diffraction peak; θ is the diffraction angle. The particle size was found to be about 38 nm which matches the size range of synthesised nanoparticles determined by FESEM and a particle size analyser.

FTIR for AgNPs was conducted to analyse the possible biomolecules, resulting in nanoparticle synthesis by bioreduction and stabilisation (Figure 4.12d). Peaks at 1491 cm^{-1} , 1390 cm^{-1} and 950 cm^{-1} represent C-H and =C–H bonds, resulting in alkynes and aromatic rings. Bands at 3790 cm^{-1} , 3023 cm^{-1} , 2884 cm^{-1} represent O-H bonds, indicating monomeric alcohols, phenols and flavonoids, which act as reducing and capping agents for nanoparticle synthesis (Singh and Dhaliwal 2020). The peak at 1390 cm^{-1} representing the C=C indicates the presence of aromatic rings peaks at 1213 cm^{-1} indicate the C-O bond of esters, carboxylic acids, alcohols, and ethers. The peak analysis of FTIR spectra shows that NSS extract can reduce and stabilise the salt into its nano-size due to the occurrence of phenols, carboxylic group and flavonoids, which is also proved in the phytochemical test of NSS extract.

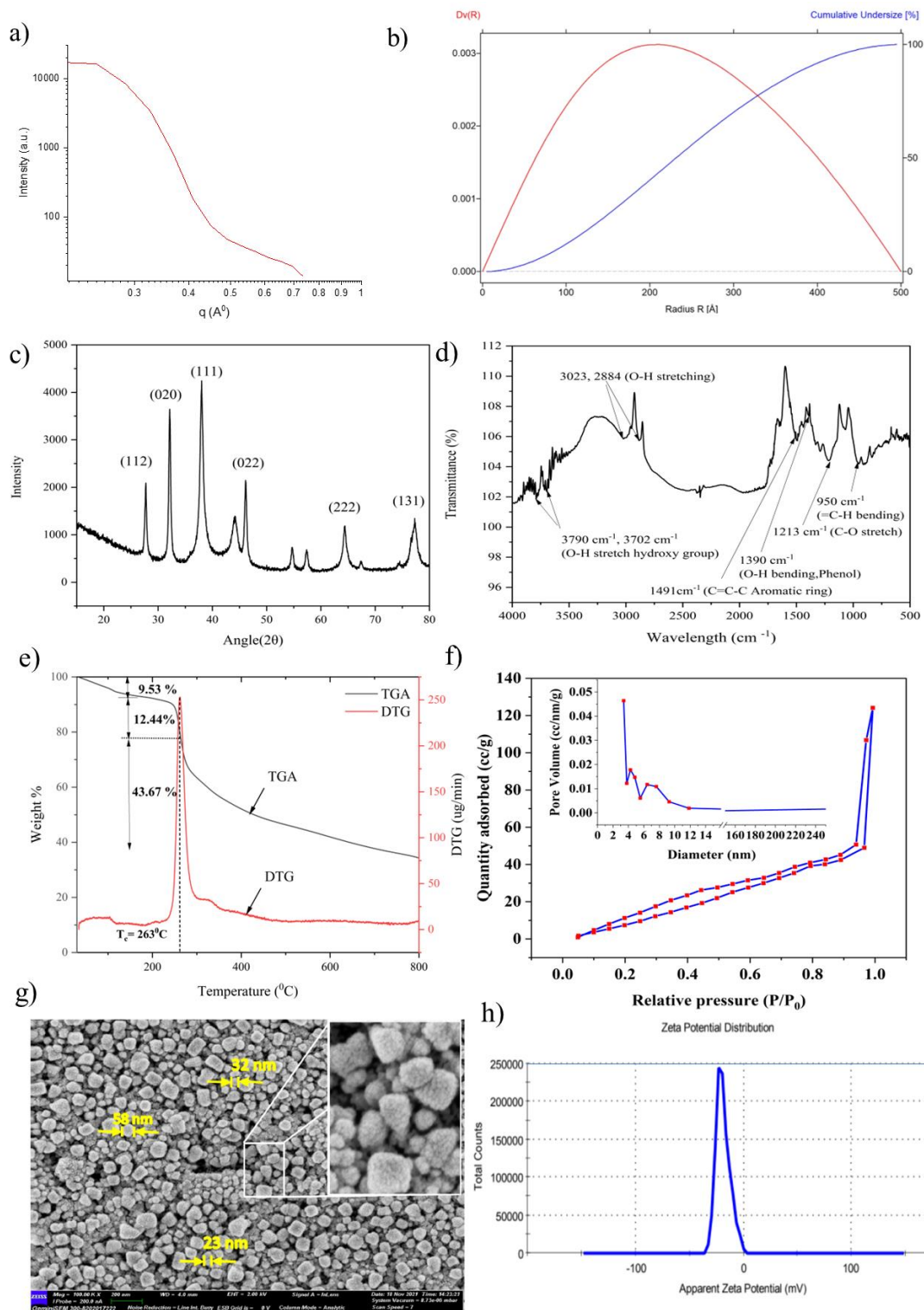


Figure 4.12 a) SAXS curve for an aqueous solution of AgNPs b) Particle size distribution c) XRD pattern for dried AgNPs d) FTIR e) DTG and TGA curve f) N₂ adsorption/desorption isotherm plot and pore size distribution g) FESEM image h) Zeta potential analysis

Hitachi EXstar TGA analyses (Figure 4.12e) the thermal stability of green synthesised AgNPs at a temperature range of 30- 800°C. The weight loss due to the desorption of biomolecules from the AgNPs is about 65%. The initial weight loss was approximately 10.2% due to the water molecules absorbed on the surface of AgNPs (30 - 260°C). Further decrement of weight is due to the degradation of biomolecules like phenols, flavonoids and proteins responsible for the bio-reduction and stabilisation of nanoparticles (260- 450°C). The results are similar to the green synthesised AgNPs studies using stem extract of *Nepeta leucophylla* (Singh and Dhaliwal 2020). At the higher temperature range of 450-800°C, a gradual reduction in the weight of nanoparticles is happening due to the metallic property of AgNPs.

The BET surface area of the prepared AgNPs was recorded as 88.16 m²/g, which is more than that reported by Chand et al., 2021, (30.881 m²/g). The nitrogen gas interaction with nanoparticles in BET analysis shows that it follows type IV isotherm according to the classification of IUPAC (International Union of Pure and Applied Chemistry) (Thommes et al. 2015). This indicates the possibility of mono-multi-layer formation in the case of synthesised AgNPs. The presence of an H3 hysteresis loop in the N₂ adsorption-desorption graph with relative pressure demonstrates the porous nature of the nanoparticle (figure 4.12f) and its pore volume reported as 0.192 cm³/g. The pore size distribution curve shows that pores range in mesoporous size. The porous nature of synthesised AgNPs is due to the formation of clusters which produce voids between atoms/molecules. The nanoparticle synthesis process includes reducing charged atoms/molecules in the precursor to form a cluster by nucleation (rearrangement of atoms/molecules). The cluster then grew into nanosized particles by the action of reducing agents in NSS extracts. Then the nanosized particles will retain their size through the action of stabilising agents present in extracts (Devatha et al. 2016).

Surface morphology analysis is done by FESEM imaging to determine the shape and size of synthesised nanoparticles. The image produced by backscattering electrons at 10K magnification shows that the particles are almost spherical and have a size range of 10 nm to 60 nm (Figure 4.12g).

The particle size analysis is also conducted using Horiba nano partica SZ-100 particle size analysed by dispersing the AgNPs in water and sonicating for 20 min. The results show that the nanoparticle size belongs to 10 - 60 nm size. The colloidal stability of nanoparticles was determined by zeta potential analysis, and it was observed as -19 mV, which is anionic (Figure 4.12h). The functional groups existing in the extract that caused the reduction and stabilisation of nanoparticles can induce a negative charge on the particles as a result of the zeta potential value (Faisal et al. 2021).

4.4.3.1 Antioxidant activity of AgNPs

Free radicals or unpaired electrons formed in the living body as a part of metabolic reactions can be suppressed by antioxidants. The presence of free radicals creates health issues like cardiovascular diseases, neurodegenerative diseases (progressive death of nerve cells), and cancer (Losada-Barreiro and Bravo-Díaz 2017). The effects of free radicals, which result in oxidative stress and nephrotoxicity, are treated with the help of antioxidants like AgNPs, as in the previous studies (Velsankar et al. 2020a). Synthesised AgNPs are analysed to determine the antioxidant property to analyse their applicability in medical and food packaging fields (Ansar et al. 2020). The antioxidant capacity was analysed by conducting two separate assays, DPPH radical scavenging and Hydroxyl scavenging.

DPPH is a free radical that an electron donor as an antioxidant can reduce. Synthesised AgNPs are compared with ascorbic acid (Vitamin C), a standard antioxidant. An antioxidant will change the stable purple colour of DPPH radical to yellow colour (non-radical). This conforms by analysing absorbance using double-beamed spectrophotometrically at 515 nm (Ansar et al. 2020). The AgNP, synthesised by the NSS aqueous extract, resulted in a comparable antioxidant property against DPPH radicals. Maximum scavenging efficiency on DPPH free radicals was 85.38% at 200 mg/mL for AgNPs, which is comparable to the DPPH free radical scavenging activity of positive control ascorbic acid. According to the increase in the concentration of AgNPs, DPPH radical scavenging activity also increases, which indicates that AgNPs affect DPPH free radical scavenging as ascorbic acid (Figure 4.13a).

Hydroxyl radicals are the most reactive radicals, which result in protein, lipid and DNA damage (Vilas et al. 2014). The hydroxyl radical-scavenging activity of nanoparticles shows a comparatively similar increment as in the case of ascorbic acid

(Figure 4.13b). With the increment in the concentration, the hydroxyl radical-scavenging activity also increased up to 85%, which is 89% in the case of ascorbic acid at a concentration of 200 $\mu\text{g/mL}$. The antioxidant property of nanoparticles is due to the presence of phenolic compounds in the NSS extract, which is used to synthesise AgNPs (Widjanarko et al. 2014).

4.4.3.2 Antibacterial properties of AgNPs

In the present study, the antibacterial property of AgNPs (25 $\mu\text{g/mL}$, 50 $\mu\text{g/mL}$) compared with positive control of ampicillin (50 $\mu\text{g/mL}$) was analysed along with silver nitrate solution and NSS aqueous extract (Figure 4.13c-f). The antibacterial property is determined for gram-negative bacteria named *E. coli rosetta* (Figure 4.13c) and *Pseudomonas aeruginosa* (Figure 4.13 d) and for gram-positive bacteria called *Bacillus haynesii* (Figure 4.13 e) and *Bacillus subtilis* (Figure 4.13 f).

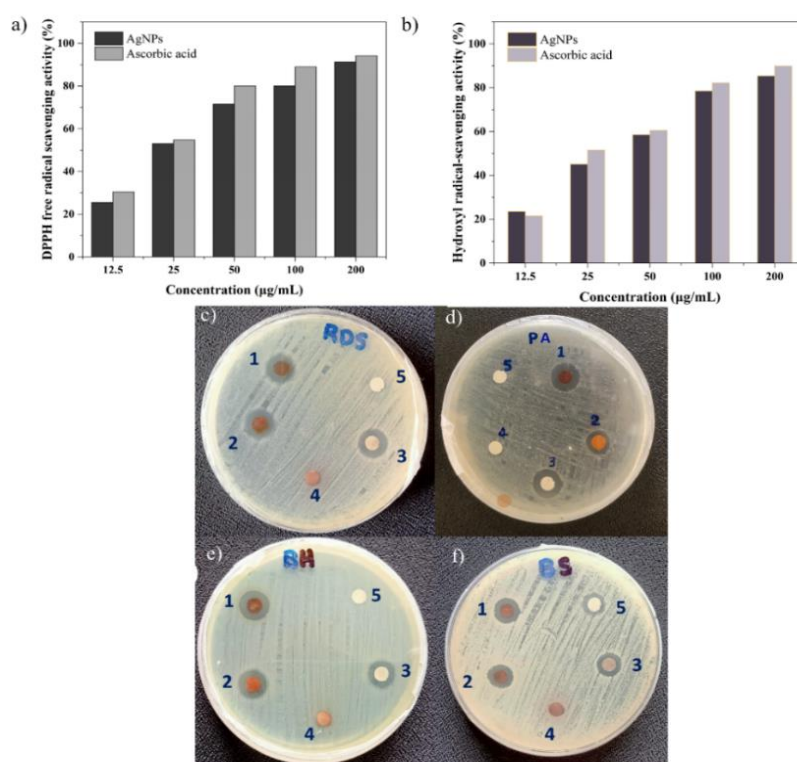


Figure 4.13 Antioxidant activity of AgNPs: a) DPPH free radical scavenging activity b) Hydroxyl radical-scavenging activity, Antibacterial activity of AgNPs against pathogenic microorganisms: c) *E. coli rosetta* (RDS) d) *Pseudomonas aeruginosa* (PA) e) *Bacillus subtilis* (BS) f) *Bacillus haynesii* (BH) (1. AgNPs: 50 $\mu\text{g/mL}$, 2. AgNPs: 25 $\mu\text{g/mL}$, 3. NSS aqueous extract 4. Ampicillin 50 $\mu\text{g/mL}$, 5. Silver nitrate)

NSS extract and silver nitrate solution have less or no antibacterial properties. But the combined effect of extract and silver nitrate solution resulted in the formation of AgNPs, resulting in higher inhibition towards almost all the gram-positive and gram-negative bacteria. Compared to the positive control, AgNPs show a better antibacterial properties. Comparing the concentration of AgNPs higher concentration (50 µg/mL) indicates slightly higher inhibition activity on microbial growth. In the case of *Pseudomonas aeruginosa*, AgNP with a concentration of 50 µg/mL has an evident antibacterial property compared to 25 µg/mL of AgNP and positive control. With the same concentration, synthesised AgNPs show better results than ampicillin for antibacterial properties in the case of gram-positive and gram-negative bacteria (Table 4.11). The inhibition of cell growth of microorganisms is due to the distortion of cytoplasm by AgNPs (Rizwan et al. 2020). Two mechanisms can attain the distortion of the microbe: it will attach to the proteins that contain sulphur and result in the cell malfunctioning. The other mechanism is attachment or penetration through the cell wall, resulting in cell degradation (Ansar et al. 2020).

Table 4.11 Inhibition zone diameter for AgNPs against bacterial strains

Microbes	Inhibition zone (mm)				
	AgNP (50 µg/mL)	AgNP (25 µg/mL)	NSS extract	Ampicillin (50 µg/mL)	1 mM silver nitrate
<i>E. coli rosetta</i> (RDS)	16	15	6	13	6
<i>Pseudomonas aeruginosa</i> (PA)	15	12	0	13	0
<i>Bacillus haynesii</i> (BH.)	15	14	6	12	0
<i>Bacillus subtilis</i> (BS)	15	14	6	9	7

4.4.4 Preliminary studies on dye degradation

The experimental setup used for the photocatalytic degradation is shown in Figure 3.2 (section 3.5.7). Degradation of dyes is determined using a UV-visible spectrophotometer based on peaks at 553 nm, 590 nm and 582 nm for RhB, RBBR and MV dyes, respectively. For preliminary studies, the concentration of dyes is selected on the basis of the literature study. The initial concentration of RhB dye was kept lower

than the other two dyes due to its zwitterionic nature, more stable structure, and highly fluorescent colour property, making it less degradable in higher concentrations (Islam 2020; Lee et al. 2020). Dye removal using AgNPs by adsorption (dark) condition resulted in a removal percentage of less than 20% for all the dyes. Light sources other than UV light did not result in much degradation, even after a reaction time of three hours. RhB dye degradation was less than 30% (initial concentration of 10 mg/L), RBBR dye (initial concentration of 100 mg/L) was less than 50%, and MV dye was about 46% (initial concentration of 100 mg/L) with a dosage of 1g/L of AgNPs (Figure 4.14). Compared to these results, the degradation of dyes using synthesised catalyst under UV light resulted in more than 75% for RhB, RBBR and MV dyes.

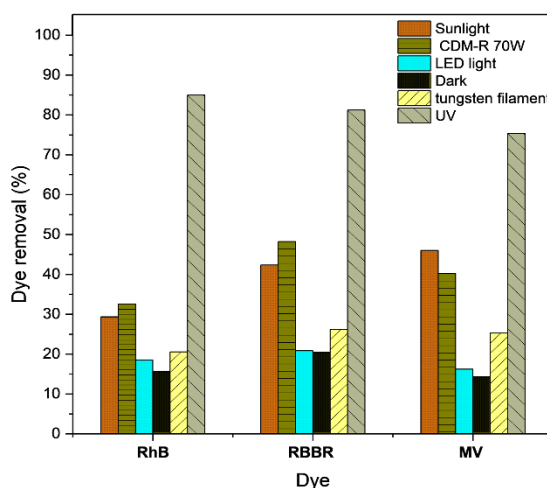


Figure 4.14 Dye removal using AgNPs under different light sources

4.4.5 Photocatalytic degradation of dyes- Optimisation of parameters

Photocatalytic degradation of RhB dye, RBBR dye, and MV dye using synthesised AgNPs was evaluated in a closed chamber under a UV light source (30 W). It showed better results than the other above-mentioned light sources. The photocatalytic degradation will happen efficiently if the pollutant is attached to the catalyst or available near the active sites. To attain this condition, the samples are kept under dark conditions for 30 min (150 rpm) to achieve dye adsorption on the catalyst (Zhang and Jaroniec 2020). In order to understand the effect of pH, contact time, catalyst dosage, and dye concentration, the studies are carried out by varying the respective parameter and keeping other parameters constant.

Initial trials are conducted to screen the pollutant concentrations that synthesised nanoparticles can degrade. RhB being a fluorescent dye has a higher intensity, and its removal at higher concentrations is a challenge in Industries. Therefore, studies are conducted with the initial concentration range of 25 to 200 mg/L for MV and RBBR, whereas for RhB dye, the studies were conducted with the initial concentration range of 2 to 100 mg/L (Lower level) with a constant catalyst dosage of 1 g/L. Table 4.12 shows the results obtained from preliminary studies. It is evident that MV and RBBR removal is considerably good in the initial concentration range of 25 to 200 mg/L. However, in the case of RhB, the efficiency drastically drops at higher concentrations and performs better only in the initial concentration range of 2 to 20 mg/L. So, secondary trials were conducted for MV and RBBR by varying the initial concentration ranges between 25 to 200 (25, 50, 100, 150 and 200 mg/L) and for RhB variations being between 2 to 20 mg/L (2, 5, 10, 15 and 20 mg/L).

Table 4.12 Preliminary study on degradation efficiency of dyes

	Dye concentration	Degradation efficiency
RBBR	25 mg/L	95%
	100 mg/L	88%
	200 mg/L	50%
MV	25 mg/L	92%
	100 mg/L	86%
	200 mg/L	66%
RhB	2 mg/L	98%
	20 mg/L	68%
	100 mg/L	36%

a) Effect of contact time: The influence of contact time on the photodegradation extent of RhB (10 mg/L), RBBR (100 mg/L) and MV dye (100 mg/L) was studied at different interval times (0-180 min) using the 1 g/L adsorbent (Figure 4.15a). According to the findings, the percentage removal of dye increased as the reaction time increased. An extended irradiation time produces more excited electrons and holes which will react with OH⁻ to form OH radicals (Ashiq et al. 2022). Until it reaches the equilibrium, the

dye molecules have more opportunities for adsorption on the adsorbent surface and radical oxidation by UV irradiation. After a certain period, the slope of the curves decreased, and the dye degradation did not alter much. This finding shows that the saturation of active sites after a certain amount of time reduces the degradation capacity of the catalyst.

b) Effect of pH: pH of the solution affects the release of hydroxyl groups as a result of photocatalytic action (Shaikh et al. 2020). Analysing the pH effect on photocatalytic degradation of RhB, RBBR, and MV dye is essential to determine the mechanism behind the dye removal. Initial concentration (RhB- 10 mg/L, RBBR- 100 mg/L, and MV- 100 mg/L) and other parameters were held constant while the pH values were altered across the range of 2-11 using 0.1 M NaOH and HCl solutions for analysing the effect of pH on dye degradation. The results are exhibited in Figure 4.15b. RhB dye can exist in two different forms; in the acidic state, it acts as a cationic dye (RhB^+), and in the alkaline state, it acts as zwitterionic (RhB^\pm) (Suguna 2013). Acidic nature results in the protonation of the catalyst. It results in repulsion between the positive charges of the dye (RhB^+), thus reducing degradation capacity due to the electrostatic repulsion (Alipour and Lakouarj 2019). The efficiency of the degradation of RhB improves up to 23% as the pH value increases to 10, and it was observed up to 97% removal at 10 mg/L of initial dye concentration. The cationic RhB gets deprotonated at a higher pH value, forming its zwitterion. In addition, basic pH production of OH radicals promotes a radical oxidation mechanism which will enhance the degradation. Above a pH of 10, the amount of OH^- ions would be high and cover the catalyst surface to make it negatively charged and replenished with enough active sites. But due to the zwitterionic nature of RhB, it will not get protonated at a pH higher than 10 and will be electrostatically kept away by the negatively charged photocatalysis. Thus, the effect of the degradation process decreases when pH exceeds the value of 10 (Al-Kahtani 2017).

Regarding the photocatalytic degradation of RBBR dye (anionic dye), the impact was investigated by altering the pH of RBBR dye solutions from 2 to 11 while maintaining a constant initial concentration (100 mg/L) and other parameters (Figure 4.15b). Silver atoms excite their electrons when exposed to UV light, creating holes in the valence band. The surface becomes positively charged, and the excitation is

amplified in acidic environments (Suprihatin et al. 2020). Thus, in a highly acidic medium, the action of protonated sites on the nanoparticles increases the degradation of anionic RBBR dye. In addition, in the acidic state perhydroxyl radical produces hydrogen peroxide, further leading to the creation of hydroxyl radicals, thus improving the photocatalytic action. In disparity, radical scavenging will occur at an alkaline state and thus reduce the rate of degradation (Alipour and Lakouarj 2019). In an alkaline medium, the surface of the photocatalyst is negatively charged and thus reduces the effect of degradation due to the repulsion of opposite charges (Mathiarasu et al. 2021).

In the case of MV (cationic dye), the protonated catalyst in the acidic state reduces the dye degradation efficiency due to the electrostatic repulsion. In an alkaline state, the catalyst got deprotonated, and the degradation efficiency got increased to its maximum (pH 9) due to electrostatic attraction among dye and photocatalyst (Figure 4.15b) (Krishnan et al. 2021).

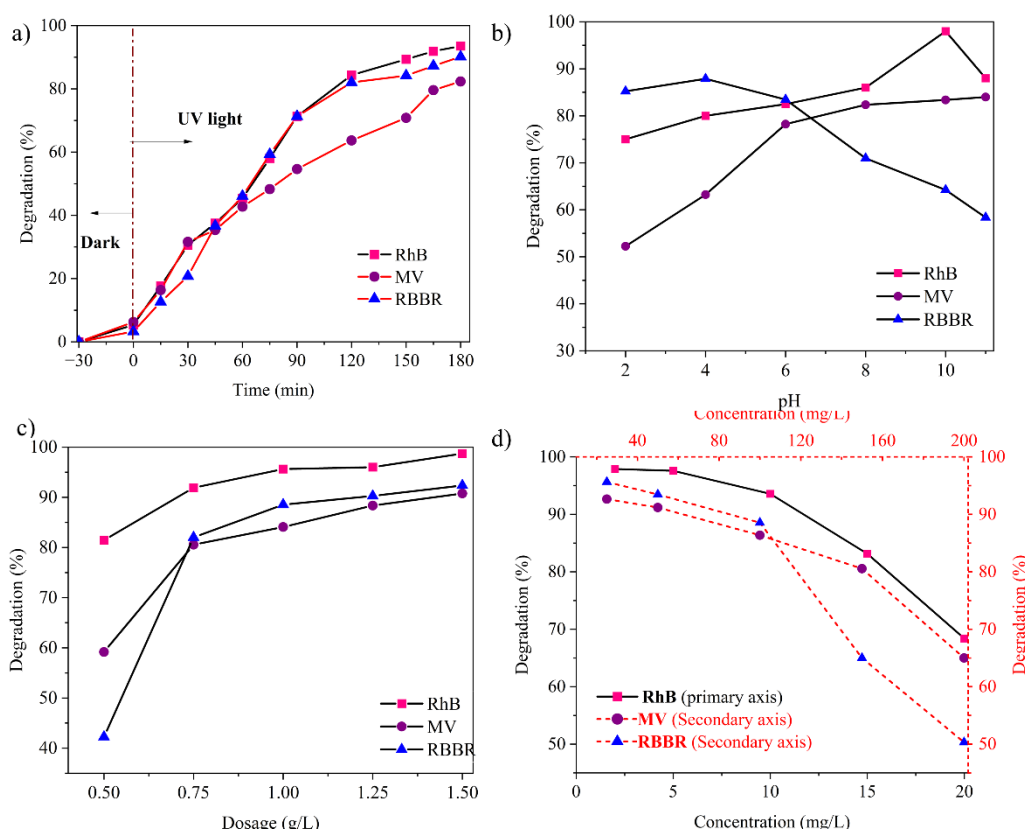


Figure 4.15 The effect of a) time b) pH c) adsorbent dose and d) Initial dye concentration on RhB dye, RBBR dye and MV dye degradation

c) Effect of adsorbent dose: The experiments were carried out using different dosages (0.5 g/L to 1.5 g/L) of AgNP catalyst constant dye concentration (RhB – 10 mg/L) and other parameters. The experiments were conducted for 180 min under UV irradiation (30 W). The plots of the dye degradation of the RhB dye are shown in Figure 4.15c. The dye degradation rose when the adsorbent dosage increased, owing to a rise in the active sites accessible on the catalyst surface (Abebe et al. 2018). Thus with a higher dosage of 1.5 g/L, RhB dye degraded up to 98.7% with a 10 mg/L initial concentration. The same experiments are done with RBBR dye and MV dye (100 mg/L for 180 min under UV irradiation) versus AgNPs as a photocatalyst (0.5 g/L to 1.5 g/L). Photocatalytic degradation of RBBR dye and MV dye also shows a similar variation of degradation efficiency as RhB dye degradation, i.e., with the increment in the dosage of catalyst, the degradation efficiency is also enhanced (with the dosage: 1.5 g/L, RBBR: 92.36% and MV: 90.76%). After a certain limit of catalyst dosage, the gradual increase in degradation does not influence the degradation rate. It is due to the action of radicals as scavengers at higher catalyst dosages (Ashiq et al. 2022).

d) Effect of Initial dye concentration: The impact of initial dye concentration on photocatalytic processes was investigated by increasing the RhB concentration from 2 mg/L to 20 mg/L while keeping the rest of the parameters constant (Dosage 1 g/L and pH 7). In the presence of UV irradiation, the catalyst was activated, generating OH radicals on the surface. A number of active sites and radicals to degrade the dye at a lower concentration (2- 7.5 mg/L) was adequate and thus resulted in better degradation efficiency. When it comes to higher concentrations gradually, the efficiency got reduced (Lee et al. 2020). At higher dye concentrations, light shading was established by more intensely coloured RhB, which prevented photons from making contact with the catalyst, resulting in insufficient production of electron-hole pairs. Consequently, the photochemical degradation efficiency reduced as RhB concentration increased (Figure 4.15d) (Shaikh et al. 2020). In Figure 4.15d primary x-axis (solid black colour) is for RhB dye, and the secondary x-axis (Dotted red colour) is for the other two dyes (RBBR and MV), which is distinguished by a different colour.

The same trend happened in RBBR dye and MV dye degradation using synthesised AgNPs as a photocatalyst. A range of 25 mg/L to 200 mg/L of initial dye concentration is selected for the initial concentration study of RBBR dye and MV dye.

For a lesser initial concentration of dye (25 mg/L to 100 mg/L), the photocatalytic degradation was more satisfying (more than 85%). Still, when it reached the case of a higher initial concentration, the photocatalytic degradation was decreased (Figure 4.15d). This occurs because the photochemical action on the catalyst surface is less than the dye concentration, which is constant for a given dosage (Shaikh et al. 2020).

4.4.5.1 Kinetic study for RhB, RBBR and MV dye

The rate of adsorption depends on physicochemical conditions, and it has complicated kinetics in the case of adsorption on solids in liquid media (Bameri et al. 2022). The photocatalytic degradation process is a time-dependent process that kinetic parameters should analyse to determine the degradation mechanism. The kinetic study for dyes revealed that according to time, the degradation efficiency is increasing (Figure 4.16a).

The degradation kinetics was assessed by considering the pseudo-first-order kinetic model (Figure 4.16b), pseudo-second-order kinetic model (Figure 4.16c), Inter-particle diffusion model (Figure 4.16d) and Elovich kinetic model (Figure 4.16e). The slope and intercept interpret the kinetic parameters of each model. The regression correlation coefficient (R^2) will assess which kinetic model is more suitable for the particular degradation process (Shaikh et al. 2020). In case an approximately equal R^2 value creates complexity in determining the best-fit model, the residual sum of squares (RSS) is considered. RSS should be near zero for the best-fit model. The R^2 value of the Pseudo-first-order kinetic model, inter-particle diffusion model and Elovich Kinetic model are much closer to each other, so the RSS value is considered (Table 4.13). RSS value is much low for pseudo-first-order kinetics; thus, the dye degradation is related to the pseudo-first-order mechanism. It shows that adsorption is monolayer, and the degradation efficiency will increase if the catalyst dosage increases.

Photocatalytic activity is the major part of degradation, so the efficiency also depends on the presence of dyes particles near the catalyst (Mosaviniya et al. 2019). Removal will be taken as an adsorption process in the case of degradation under dark conditions. Then under UV light, the degradation follows with Pseudo-first-order kinetics, a typical characteristic of photocatalytic degradation (Rahmat et al. 2019). The dosage of AgNPs as a photocatalyst is more related to the degradation mechanism.

Well-distributed catalysts will enhance the creation of excited electrons and holes, enhancing the degradation of dyes (Mosaviniya et al. 2019).

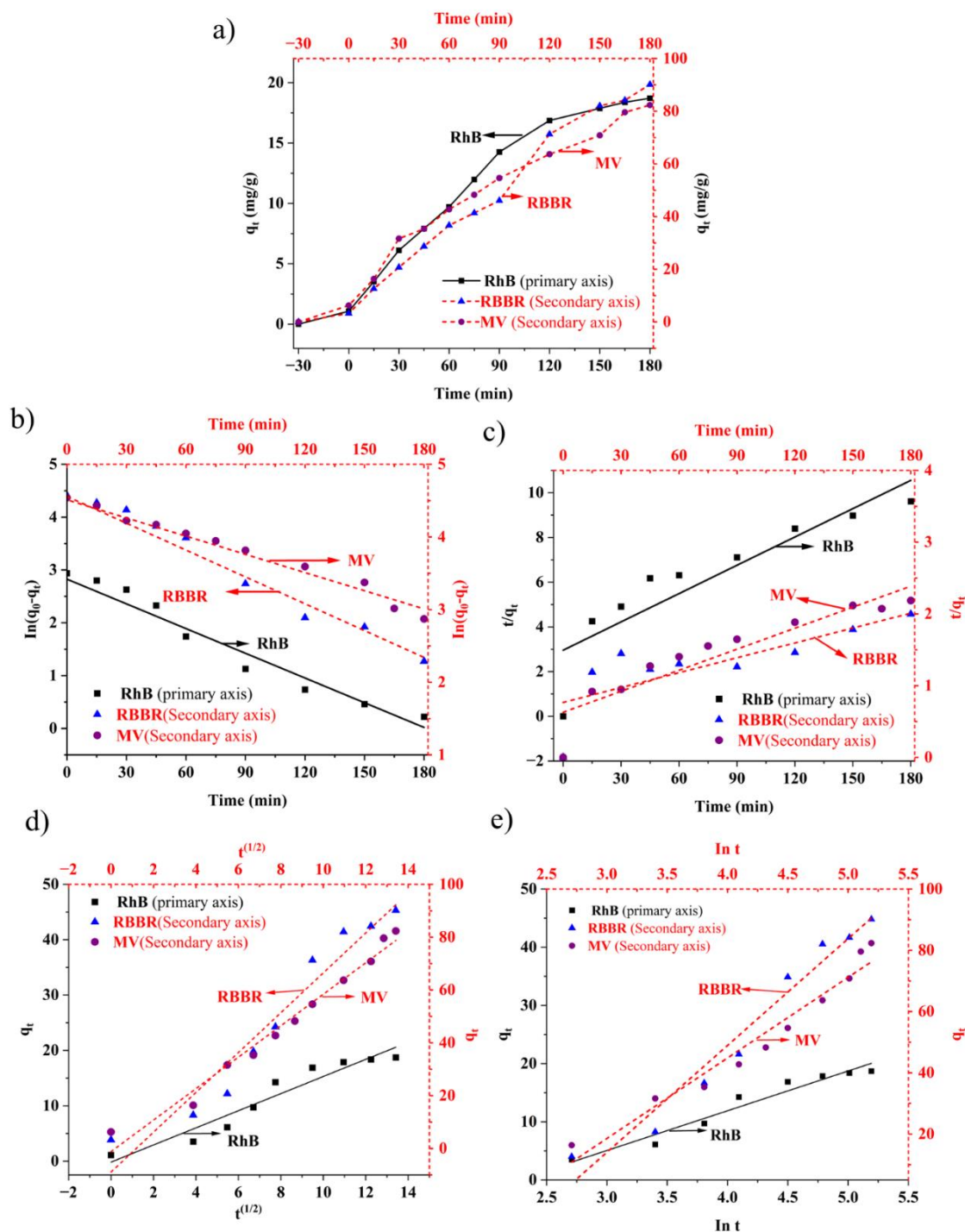


Figure 4.16 a) Adsorption kinetics b) Pseudo-first-order kinetic model c) Pseudo-second-order kinetic model d) Interparticle diffusion kinetic model e) Elovich kinetic model for degradation of RhB dye, RBBR dye and MV dye

4.4.5.2 Isotherm study for RhB, RBBR and MV dye

Dye solutions (10 mL) at varying concentrations (RhB: 2 mg/L to 20 mg/L, RBBR and MV: 25 mg/L to 200 mg/L) with 10 mg of AgNP are analysed to determine the effect of initial concentration on the RBBR dye removal efficiency by the isotherm study (Figure 4.17a). The isotherm study indicated that with a lower initial concentration of dye, degradation is more due to the availability of unsaturated active sites on the catalyst (Abebe et al. 2018; Thomas and Thalla 2022). Langmuir isotherm model (Figure 4.17b) resulted in a higher correlation coefficient ($R^2 > 0.99$) compared to the Freundlich isotherm (Figure 4.17c) and Temkin isotherm (Figure 4.17d) in the case of all the dyes, which confirms that the absorption follows homogenous-monolayer adsorption (Bameri et al. 2022) (Table 4.13). The adsorption capacity determined by the model was 27.78 mg/g, 109.89 mg/g and 128.20 mg/g, which is nearer to experimental data, i.e., 15 mg/g, 101 mg/g and 124 mg/g for RhB, RBBR and MV dye respectively.

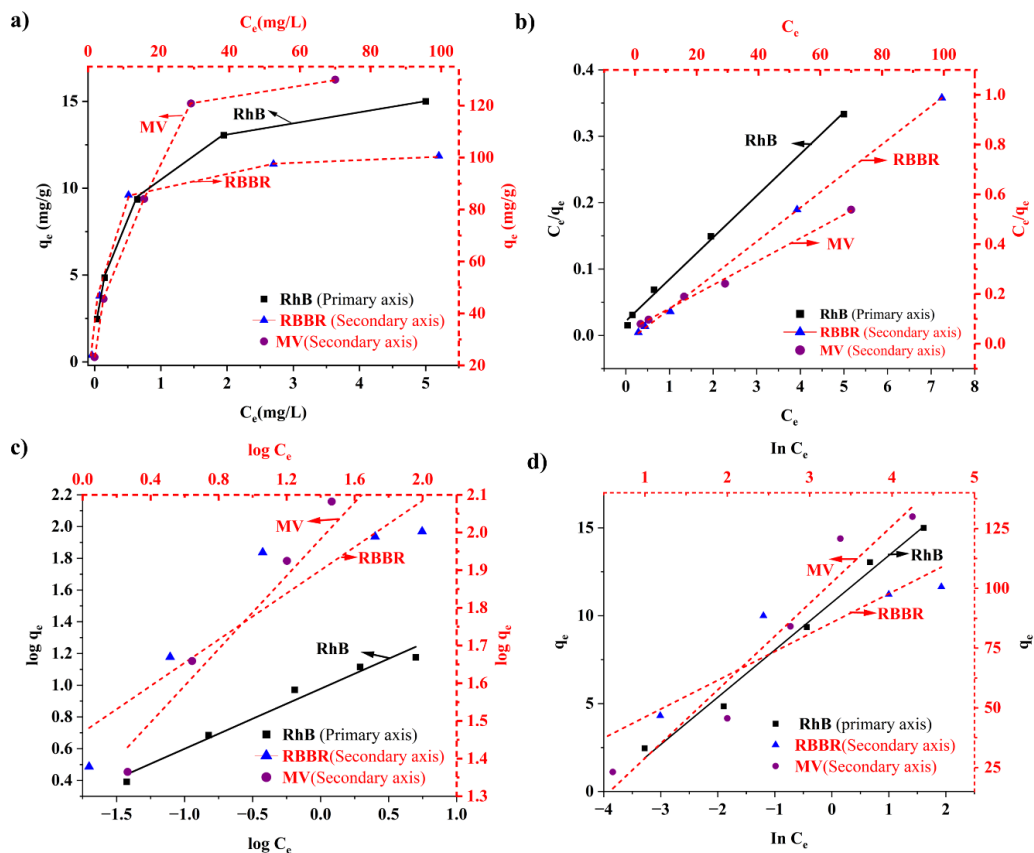


Figure 4.17 The plots of a) Adsorption isotherm b) Langmuir isotherm c) Freundlich isotherm d) Temkin isotherm of RhB dye, RBBR dye and MV dye

Table 4.13 Parameters of kinetic and isotherm study for RhB, RBBR and MV dyes

		Parameter	RhB	RBBR	MV	
Kinetics models	Pseudo first order	q_e (mg/g)	19.37	95.29	91.07	
		K_1 (1/min)	0.02	0.02	0.01	
		R^2	0.98	0.97	0.98	
		RSS	0.716	0.24	0.089	
	Pseudo second order	q_e (mg/g)	25.49	144.72	102.354	
		K_2				
		(g/mg/min)	0.01	0.01	0.001	
		R^2	0.84	0.80	0.85	
	Interparticle diffusion	RSS	10.71	0.98	0.62	
		c	0.51	3.91	1.18	
		k_d	1.48	7.54	5.96	
		r_2	0.96	0.94	0.97	
	Elovich Kinetic model	RSS	11.59	52.9	13.9	
		α (mg/g/min)	0.15	0.03	0.04	
		B (g/mg)	0.62	2.59	2.65	
		R^2	0.97	0.96	0.96	
Isotherm models	Langmuir	RSS	6.03	25.4	18.5	
		q_{max} (mg/g)	27.78	109.89	128.20	
		k_l (L/mg)	0.57	0.60	0.60	
		R^2	0.99	0.99	0.99	
	Freundlich	RSS	0.001	0.002	0.001	
		k_f (L/mg)	9.50	4.34	3.72	
		n	2.64	3.25	2.19	
		R^2	0.94	0.85	0.93	
	Temkin	RSS	0.01	0.04	0.02	
		k_t (L/mg)	54.27	5.18	0.99	
		b_t (J/mol)	2.689	17.43	29.57	
		R^2	0.95	0.91	0.93	
			RSS	1.24	41.4	31.1

4.4.6 Degradation mechanism

The mechanism behind the photocatalytic degradation of dyes (RhB, RBBR, MV) using synthesised AgNPs is represented schematically in Figure 4.18. The initial dark condition of 30 minutes will result in the adsorption of dye onto the nanoparticle's surface. When the dye solution is exposed to UV light, the electrons in its valance band get excited to enter the conduction band, releasing a photon with energy more than the band gap. This creates holes in the valance band (Bameri et al. 2022). Holes formed in the valance band will react with water and forms $\text{OH}\cdot$ radicals which act as a strong oxidising agent, and electrons in the conduction band react with O_2 and form $\text{O}_2\cdot$ radical, which is a superoxidase agent, which will prevent the recombination and neutrality of the system. Thus, the system will generate enough $\text{OH}\cdot$ radicals, which will help to degrade the dyes and result in smaller organic compounds (water, CO_2 and residues) by further mineralisation of degraded products.

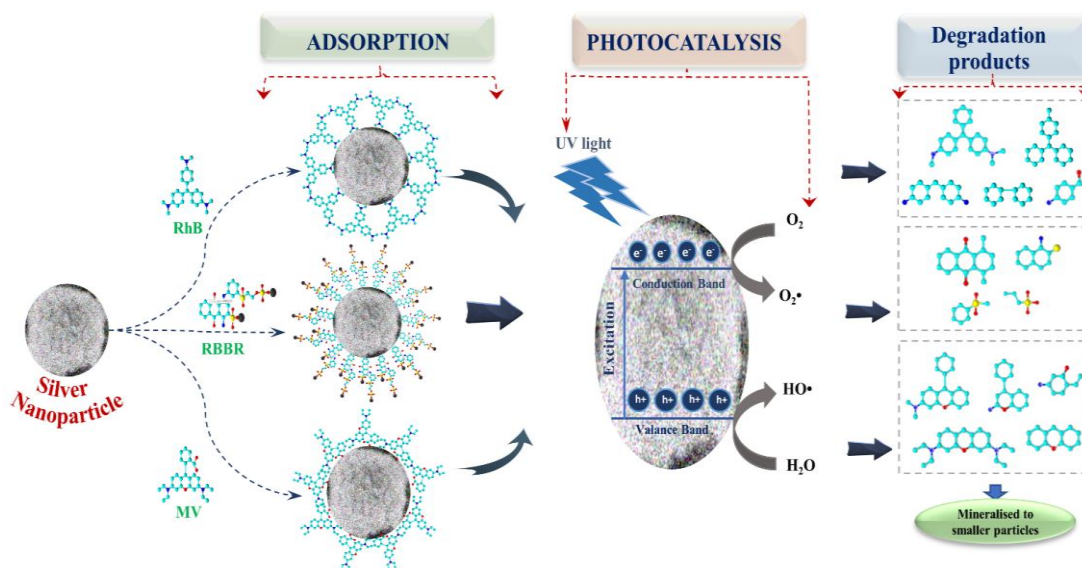


Figure 4.18 Degradation mechanism of dyes using AgNPs

4.4.7 By-products of photocatalytic dye degradation using AgNPs

The UPLC–MS system detected mass/charge (m/z) values of 443, 501, and 374 for RhB, RBBR, and MV dye, respectively. HRLC-MS analysed the degradation products by photocatalytic degradation. The fragmentation pattern obtained by HRLC-MS analysis is shown in Figure 4.19. Deamination, dihydroxylation, deamination and cleavage of quinone structure by the action of OH radicals formed in the photocatalytic

process are the main mechanisms involved in the degradation of dyes. The degradation process of dye resulted in organic intermediate products and further mineralised into CO₂ and water. The degradation of RhB dye (Figure 4.19a) resulted in the formation of N,N-dimethyl-9-phenyl-3H-xanthen-6-amine (m/z = 301) by C-N group cleavage. Similar products are also reported in the literature of other works (Tu et al. 2022). Further degradation products like N₃,N₃,N₆,N₆-tetraethyl-3H-xanthene-3,6-diamine (m/z = 323), 4-phenyl-2H-1-benzopyran-2-imine (m/z = 220), 2,6-dihydro-1H-xanthene (m/z = 184), 3-amino-6-ethylcyclohexa-1,5-dien-1-ol (m/z = 140) are resulted by dihydroxylation and deamination.

In the case of RBBR degradation, products formed as shown in Figure 4.19b. The degradation first occurs by deamination and then propagated by the degradation of quinone structure, resulting in sulphonic acid derivatives and ending with simple organic compounds (Bilal et al. 2018)(Bilal et al. 2018). In the proposed pathway, the degradation initiated with the elimination of amino and sulphonic groups from the dye structure and resulted in the products with m/z value of 233 (1,4-dimethylidene-1,4-dihydroanthracene-9,10-dione). Further degradation occurred by the breaking of the aromatic group and resulted in smaller products like 1-amino-1,2-dihydronaphthalene-2-thiol (m/z = 177), (methanesulfonyl)benzene (m/z=157) and propane-1-sulfonic acid (m/z=125).

MV dye degradation takes place by demethylation and deamination under UV light and radicals created in the presence of a photocatalytic process (Favaro et al. 2012). The degradation by the deamination resulted in the formation of products (Figure 4.19c) like 4-((cyclohexa-2,4-dien-1-ylidene)[4-(methylamino)-phenyl]methyl)-N,N-dimethylaniline (m/z= 316) and 1,1'-[(4-methylidenecyclohexa-2,5-dien-1-ylidene)methylene]dibenzene (m/z= 256). OH radicals formed in the photocatalytic process are responsible for degrading dye structure by cleavage action of bonds and result in simple organic compounds by ring opening mechanism (Chandra Pragada and Thalla 2021). Cleavage of the aromatic ring further resulted in the formation of organic compounds like 4,4'-methylenedibenzaminium (m/z = 200), 1,1'-bi(cyclohexa-2,4-diene) (m/z= 158) and 1-(4-aminocyclohexa-2,4-dien-1-yl)ethanol (m/z = 139). These products are then mineralised to form simple organic compounds.

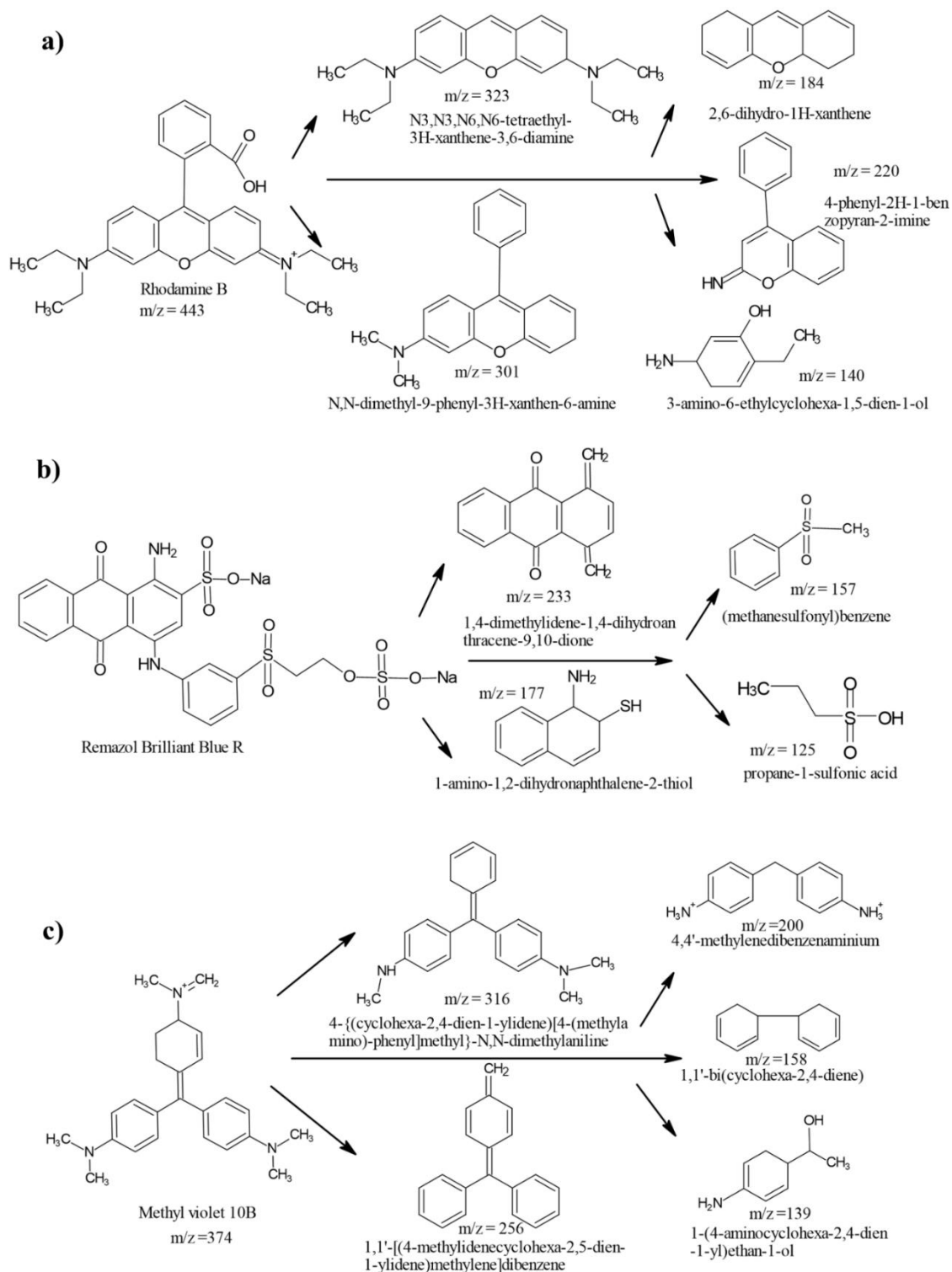


Figure 4.19 Possible degradation pathway of a) RhB dye b) RBBR dye c) MV dye based on HRLC-MS analysis

Compared to the other parts of nutmeg, the NSS, which is an agricultural waste, has reducing and capping agents to produce nanoparticles which have antibacterial, antioxidant, and photocatalytic properties to degrade especially stable dyes like RhB, RBBR and MV dye (Table 4.14).

Table 4.14 AgNP synthesis from Nutmeg

Material	Extract	AgNP size	UV- range	Application
Nutmeg seed	Ethanol extract	~10 nm	400-450nm (0.1 mM of silver nitrate)	Antibacterial activities (Malini et al. 2019)
	Hydro-ethanolic Extract	50-60 nm	430nm (1 mM silver nitrate)	Anti-Diabetic activity (Ramya P 2022)
	Aqueous extract	-	460 nm (1 mM silver nitrate)	Medicine and related fields due to antibacterial properties (Jelin et al. 2015)
Nutmeg bark	Aqueous extract	-	460 nm (1 mM silver nitrate)	Medicine and related fields due to antibacterial properties (Jelin et al. 2015)
Nutmeg pericarp	pericarp Aqueous extract	13 ±0.63 nm	478 nm (silver nitrate (10 mmol)	Antimicrobial and catalytic applications (Sasidharan et al. 2020)
Nutmeg oleoresin	-	spherical-shaped, 20–50 nm	450 nm (1 mM aqueous silver nitrate)	Antibacterial, cytotoxicity, drug delivery, and biosensor applications (Madhumithaa et al. 2019)

	-		434 nm (1 mM silver nitrate)	Application as drugs against oral pathogens (Pranati et al. 2019)
Nutmeg oil	-	33.2- 39.7 nm	420 nm (1 mM silver nitrate)	Antibacterial (<i>S. aureus</i>) and anti-fungal agent (<i>A. niger</i>) (Pauline et al. 2019)
NSS	Aqueous extract	5- 60 nm	470 nm (1mM silver nitrate)	Antibacterial property, photocatalytic activity, antioxidant activity (present study)

The photocatalytic degradation of RhB, RBBR and MV dyes with AgNPs synthesised by different plant extracts compared with NSS-based AgNPs are listed in Table 4.15. Titanium dioxide nanoparticles are less expensive since the raw salt of the nanoparticle has a low cost (Salomatina et al. 2021). The studies on titanium oxide compared to AgNPs composite with Fe₂O₃ resulted in better RhB dye degradation with silver-based composite than TiO₂-based composite under higher intensity UV light (61.8 W/m²) with high catalyst dosage (Muraro et al. 2020). In the case of MV dye (10 mg/L), green synthesised TiO₂ nanoparticles (1 g/L) resulted in 93.1% degradation after 6 hours of sunlight exposure (Ramasamy et al. 2021). RBBR dye (156.5 mg/L) is also studied for degradation using Mo, Mn and La-doped TiO₂ (10 g/L) with a light source of a halogen lamp (500 W) resulted in 70% degradation efficiency in 3 hours (Umar et al. 2013).

Table 4.15 Synthesis of AgNPs using various plant extracts and their dye degradation efficiency

Dye	Nanoparticle synthesis	Dye concentration	Light source	Dose	Time	dye degradation	Reference
CV dye	Ruellia tuberosa water extract	-	sunlight	0.5 g/L	180 min	87%	(Seerangaraj et al. 2021)
	<i>Sanguisorba officinalis</i> water extract	10 mg/L	UV	1 g/L (10–50 nm)	180 min	90%	(Baker et al. 2020)
	NSS extract	100 mg/L 25 mg/L	UV.	1 g/L	180 min	88% 94%	This study
RhB dye	Shorea robusta water extract	20 mg/L	UV.	6 mL colloidal Ag NPs in 25 mL dye	90 min	90.41%	(Shaikh et al. 2020)
	Matricaria chamomilla L water extract	4.8 mg/L	UV	50 g/L	130 min	93.9%	(Alshehri and Malik 2020)
	NSS extract	10 mg/L	UV.	10 mg/L	180 min	97%	This work
RBB R dye	Methanolic extract of C. intybus extracts	41.4 mg/L	Sunlight	18.57 g/L	30 min	58.15%	(Sidorowicz et al. 2021)
	NSS extract	100 mg/L	UV.	1 g/L	180 min	92%	This work

4.5 Utilisation of Ag/Fe/Lignin composite for dye degradation

The effect of dye degradation using a composite synthesised by silver and NSS-based alkali lignin with induced magnetic property (Ag/Fe/Lignin) is analysed for single dyes and a mixture of anionic, cationic and zwitterionic dyes. The effect of degradation was also analysed by adding an activator (hydrogen peroxide) along with the composite (Ag/Fe/Lignin).

4.5.1 Lignin extraction and characterisation

Lignin from NSS waste got extracted by adopting different extraction methods with different combinations of solvents. The yield of lignin obtained after extraction is listed in Table 4.16. Alkali soluble lignin is selected for further studies due to the higher extraction yield by NaOH (Table 4.17). Alkali lignin extraction is then optimised with varying NaOH concentrations. The optimum lignin yield of 33% is obtained by using a 12% NaOH solution. Further increment of NaOH concentration doesn't increase lignin yield much. Thus, by alkali extraction (12% of NaOH), 20% of the total lignin present in NSS got extracted. This shows that extraction of lignin from NSS can be taken place by alkali extraction with 12% NaOH concentration and a 1:10 w/v ratio of NSS and NaOH solution (Figure 4.20).

Table 4.16 Lignin yield from NSS

Type of lignin	Weight percentage
Total lignin	60.75%
Alkali lignin yield	33%
Acid-soluble lignin yield	5%
Organosolve lignin yield	3%



Figure 4.20 Alkali lignin obtained from NSS

Table 4.17 Lignin yield with different concentrations of sodium hydroxide

NaOH concentration	Lignin yield
2% (w/v)	5.98%
5% (w/v)	15.58%
8% (w/v)	21%
10% (w/v)	30.36%
12% (w/v)	33.65%
15% (w/v)	33.89%

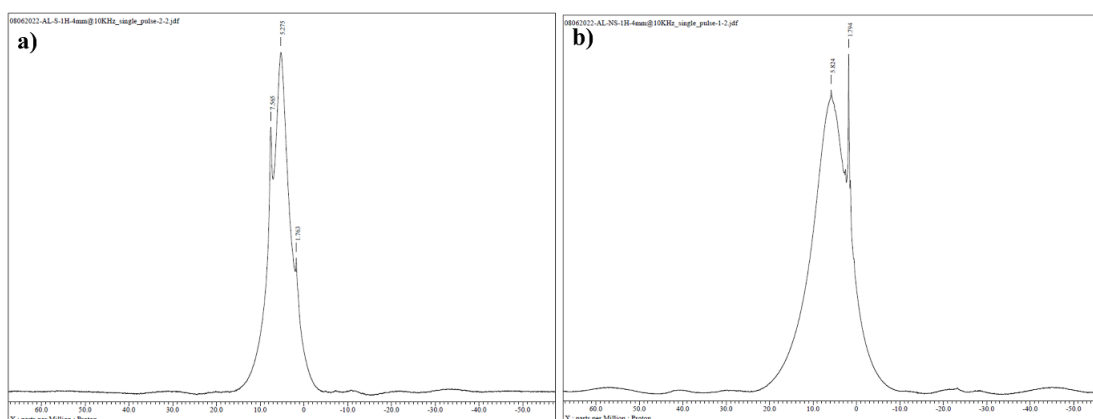


Figure 4.21 ¹H NMR spectra for a) Commercially available alkali lignin and b) alkali lignin extracted from NSS

Due to the complex structure of lignin, which makes it insoluble in most of the solutions used in liquid state analysis, detailed analysis is difficult. Due to this reason, lignin is analysed with solid phase NMR ¹H and compared with commercially available alkali lignin (Sigma Aldrich). Figure 4.21 shows the solid-state ¹H NMR spectrum of synthesised commercially available lignin (Figure 4.21a) and NSS-based lignin (Figure 4.21 b). The proton spectrum in commercial lignin reveals signals at 7.59, 5.275, and 1.76 mg/L, attributed to aromatic, methoxy, and aliphatic protons, respectively (Budnyak et al. 2021). But lignin separated from NSS resulted in a wider coupled peak. The wider peak shows an aromatic group (6 mg/L -8.7 mg/L) in monolignols from lignin. In this sample, 5.82 and 1.79 mg/L shows the presence of phenols/alkenes/vanillic and aliphatic group, respectively.

4.5.2 Synthesis and characterisation of Ag/Fe/Lignin

Ag/Fe/Lignin is synthesised as explained in section 3.6.1.5. The characterisation of the composite is done as explained in section 3.6.2.

a) **Surface morphology analysis:** Ag/Fe/Lignin is analysed using FESEM images, which shows the composite is in the size range of 50-200 nm (Figure 4.22a). Figure 4.22 a,b,c shows Ag/Fe/Lignin composite in different magnifications of 25K (Figure 4.22 a), 50K (Figure 4.22 b) and 100K magnification (Figure 4.22c). EDX mapping of the composite shows the presence of carbon, oxygen, nitrogen and sodium, as shown in Figure 4.22 d,e,f,g, respectively. And the studies confirmed the presence of iron particles (Figure 4.22h) and silver (Figure 4.22i) attached to the lignin particles. EDX spectrum (Figure 4.22j) also emphasises that the composite contains silver and iron content.

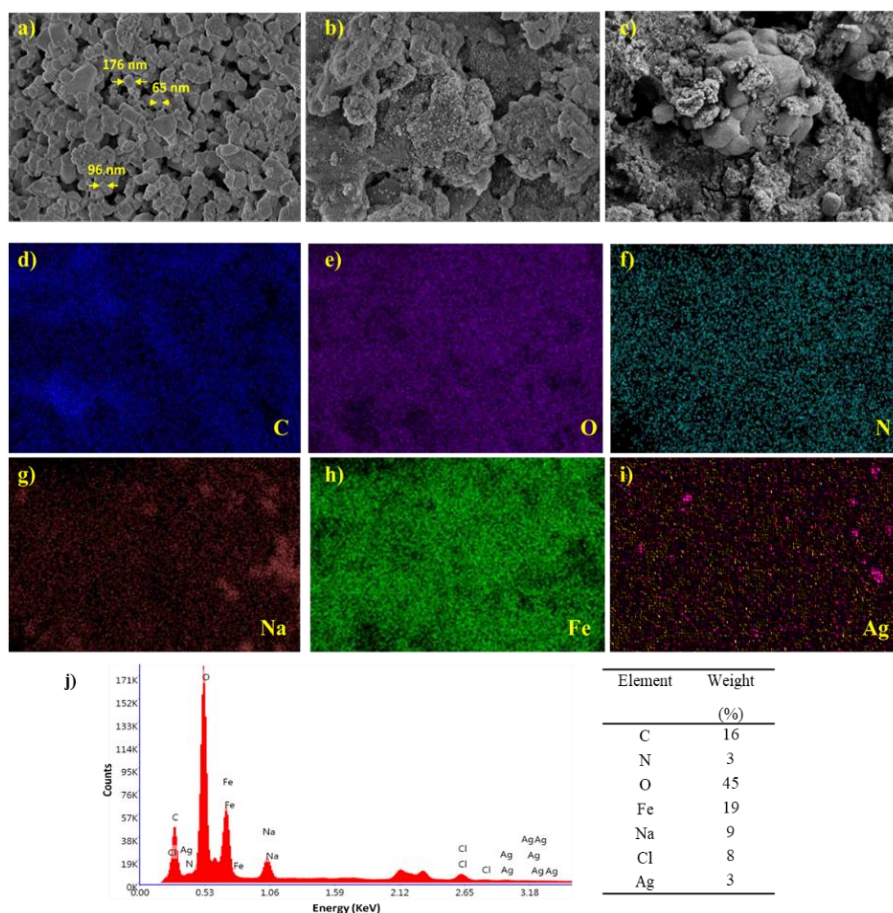


Figure 4.22 SEM images of a) 25 K b) 50 K c) 100 K magnification, elemental mapping images of Ag/Fe/Lignin: d) Carbon e) Oxygen f) Nitrogen g) Sodium h) Iron i) Silver and j) EDX spectrum

b) FTIR analysis: FTIR spectra of NSS, AgNPs, lignin, Fe/Lignin and Ag/Fe/Lignin are shown in Figure 4.23. NSS showed peaks of hydroxyl, amide, ester, aldehydes, ketones, and aromatic C-H groups. Peaks at 1500 – 900 cm^{-1} indicate C–O bonding, which shows a non-ionic carboxylic group (Figure 4.23a) (Barka et al. 2013; Lewis et al. 2019). FTIR spectra for AgNPs assisted in analysing the possible biomolecules responsible for nanoparticle synthesis by bioreduction and stabilisation (Figure 4.23b). Peaks at 1491 cm^{-1} , 1390 cm^{-1} and 950 cm^{-1} represent C-H and =C–H bonds, showing the presence of alkynes and aromatic rings. Peaks at 3790 cm^{-1} , 3023 cm^{-1} , 2884 cm^{-1} represent O-H bonds, indicating the presence of monomeric alcohols, phenols and flavonoids, which act as reducing and capping agents for nanoparticle synthesis (Singh and Dhaliwal 2020). The peak at 1390 cm^{-1} representing the C=C indicates the presence of aromatic rings, and the peak at 1213 cm^{-1} indicates the C-O bond of esters, carboxylic acids, alcohols, and ethers. The peak analysis of FTIR spectra shows that the biomolecules (phenols, carboxylic group and flavonoids) present in NSS extract are responsible for the reduction and stabilisation of AgNPs, which is also proved by the phytochemical test conducted for the NSS extract. FTIR spectra of lignin show peaks at 1618 cm^{-1} , which represents the presence of aldehydes, and peaks at 1052 cm^{-1} , representing ethers, ester and carboxylic acids (Jiang et al. 2022). Phenol and alcohols are also present in lignin, indicated by the peak at 3564 cm^{-1} (Figure 4.23c). In the case of Fe/Lignin, the lignin presence is indicated by the peaks of 1129 cm^{-1} and 3088 cm^{-1} (aromatic rings). The presence of magnetic iron particles is also evidently reflected in the FTIR spectra of Fe/Lignin by the peak at 488 cm^{-1} (Figure 4.23d).

The combination of magnetic iron and silver with lignin (Ag/Fe/Lignin) resulted in a shift of peaks, but the presence of magnetic iron particles is represented by the peaks at 480 cm^{-1} and the presence of lignin by the peaks at 1537 cm^{-1} , 1297 cm^{-1} and 1095 cm^{-1} which represents the presence of esters, ethers and carboxylic acids (Figure 4.23e).

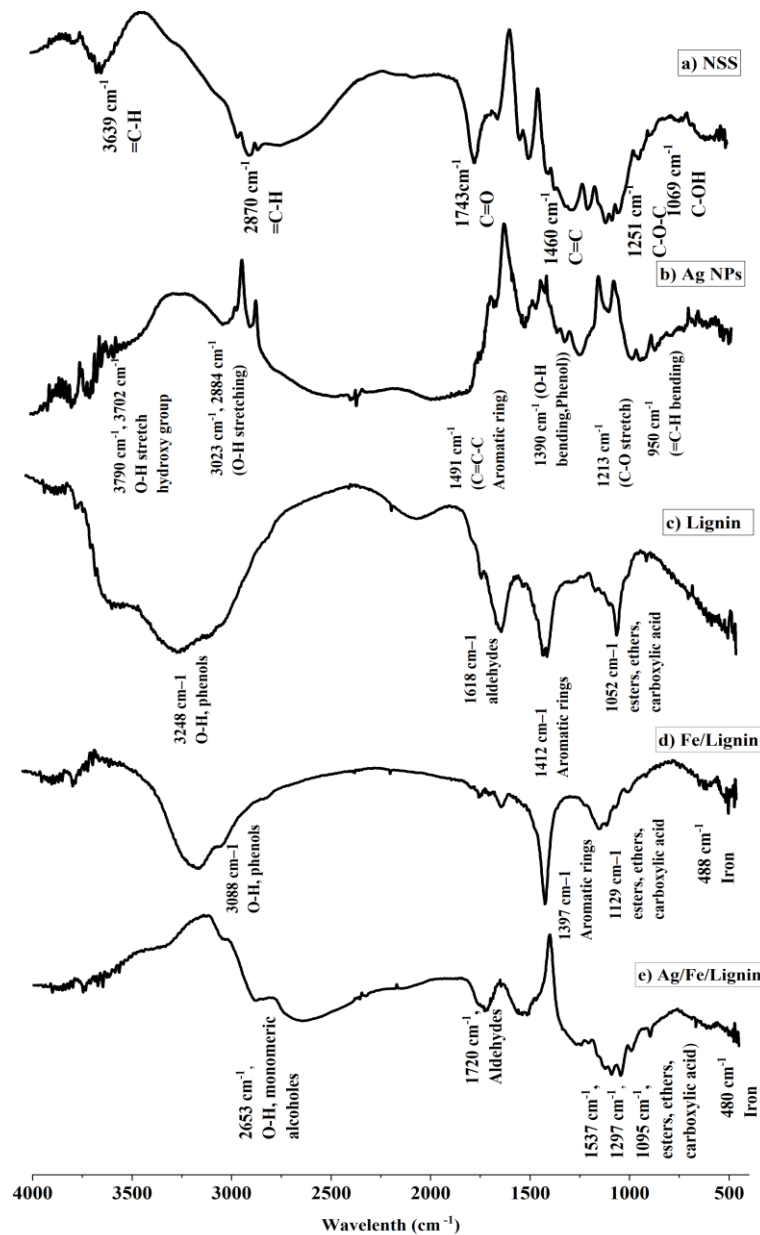


Figure 4.23 FTIR results for a)NSS b) AgNPs c) Lignin d) Fe/Lignin e)Ag/Fe/Lignin

c) **XRD analysis:** Powder XRD patterns for Ag/Fe/Lignin and other composites are analysed and shown in Figure 4.24. XRD pattern for NSS powder shows a peak of vanillin at $2\theta = 26.507^\circ$ (figure 4.24a). XRD spectra of alkali lignin extracted from NSS show it is amorphous (Figure 4.24b) with two broad peaks at 17° and 22° . The peaks were observed for AgNPs (Figure 4.24 c) at the 2θ range of 27.84° , 32.85° , 37.73° , 46.26° , 57.52° , 63.748° and 76.515° , corresponding to the Bragg's reflection planes 112, 020, 111, 022, 222, and 131, which represent AgNPs in the cubic crystal lattice

(JCPDS No: 96-901-3047). The peaks observed in Fe_3O_4 (Figure 4.24d) in the 2θ range of 30.31° , 35.71° and 63.056° represents correspond to the lattice plane (022), (131) and (044) magnetised iron. Hashemi et al. (2020) and Shagholani et al. (2015) show similar results for magnetised iron particles. The XRD spectrum of Ag/Lignin (Figure 4.24e) evidenced a crystalline nature by the value of the peaks 2θ at 38.42° , 44.36° , 64.40° and 77.49° related to the lattice planes (111), (020), (002), and (131) respectively which represents the presence of silver. In the case of Fe/Lignin (Figure 4.24f), the peaks at 35.71° and 63.05° are related to the lattice planes (131) and (044) representing Fe_3O_4 . In the case of silver presence in Ag/Fe/Lignin (Figure 4.24g) is shown as peaks like 27.84° , 32.85° , 37.73° , 46.26° , 57.52° , and 76.515° , corresponding to the lattice planes 112, 020, 111, 022 and 131. XRD peaks of Ag/Fe/Lignin show silver and magnetised iron particles in the composite.

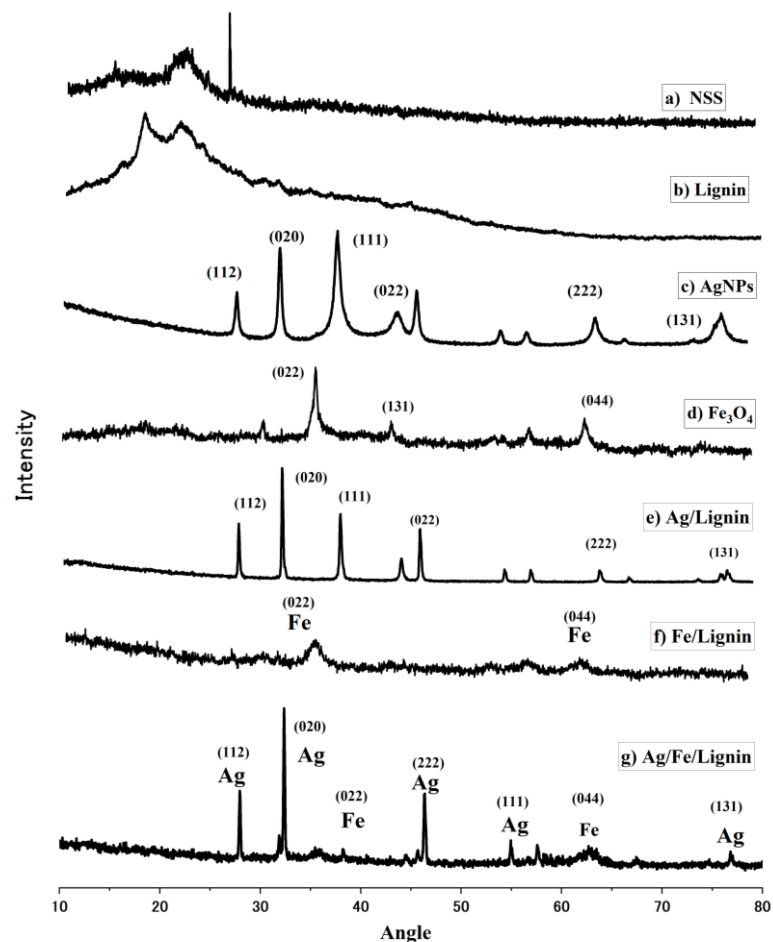


Figure 4.24 XRD analysis for a) NSS b) Lignin c) AgNPs d) Fe_3O_4 e) Ag/Lignin f) Fe/Lignin g) Ag/Fe/Lignin

d) Raman spectra analysis: The Raman spectra peaks in lignin, especially in the range of $1620\text{-}1745\text{ cm}^{-1}$, represent amide, phenolic ketone, aldehyde, and ester (Figure 4.25a) (Agarwal et al. 2011). These peaks are also present in sample AgNPs, showing that the silver converted to nanoparticles with the help of these components is also present in NSS extract (Figure 4.25 b). The peak at 240 cm^{-1} in sample AgNPs shows the synthesised AgNPs and similar results reported by Luis López-Miranda et al. (2016). And this peak is also present in Ag/Lignin (Figure 4.25c) and Ag/Fe/Lignin (Figure 4.25f) samples revealing the presence of silver. Sample Fe_3O_4 shows peaks at 218 cm^{-1} , 281 cm^{-1} , 392 cm^{-1} , 590 cm^{-1} and 1290 cm^{-1} (Figure 4.25d), and these peaks are reflected in Fe/Lignin (Figure 4.25e) and Ag/Fe/Lignin showing the presence of magnetic iron particles in the composite. Raman spectra for Fe_3O_4 , Fe/Lignin and Ag/Fe/Lignin show similarity peaks as the results of a character study carried out for magnetite particles by Slavov et al. (2010). Raman spectra peaks of Ag/Fe/Lignin reveal that the composite contains the peaks specifically for silver and magnetised iron and component peaks for lignin.

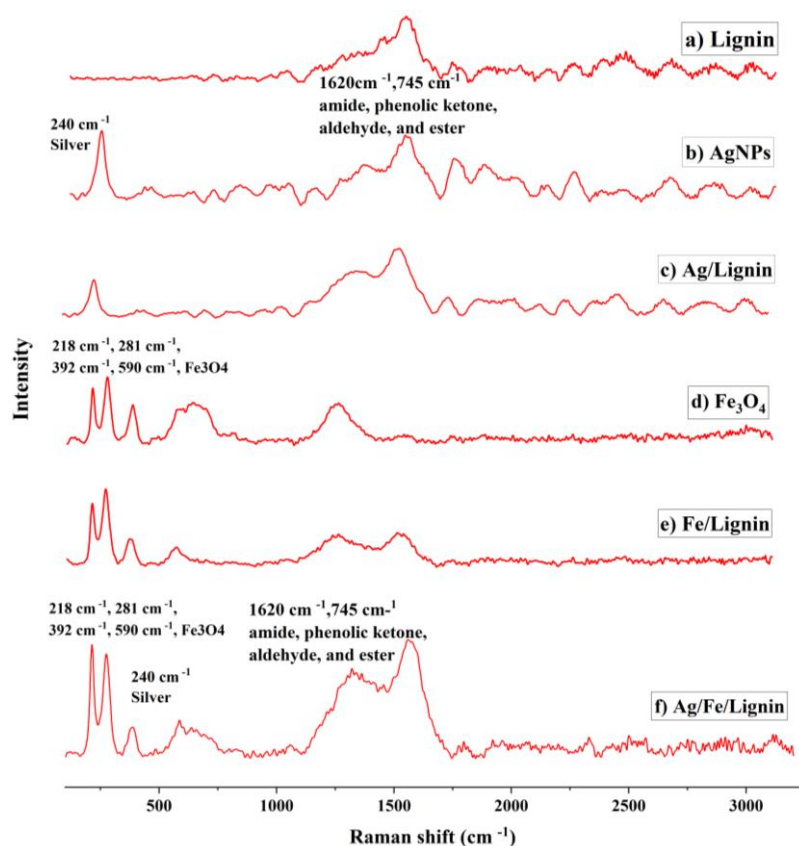


Figure 4.25 Raman spectra for a) Lignin b) AgNPs c) Ag/Lignin d) Fe_3O_4 e)Fe/Lignin f) Ag/Fe/Lignin

e) **Surface area analysis:** Nitrogen adsorption and desorption studies were carried out to analyse the properties of the pores and specific surface areas of Ag/Fe/Lignin (Figure 4.26a). The inset displays the Barrett Joyner Halenda pore-size distributions (Figure 4.26a-inset). According to the IUPAC classification, the isotherm is classified as a type IV with a type H3 hysteresis loop (Thommes et al. 2015). Ag/Fe/Lignin had a mesoporous structure, as evidenced by the BJH curve of the pore-size distribution with an average pore radius of around 2.1 nm and a pore volume of 1.519 cc/g with a surface area of 48.21 cm²/g.

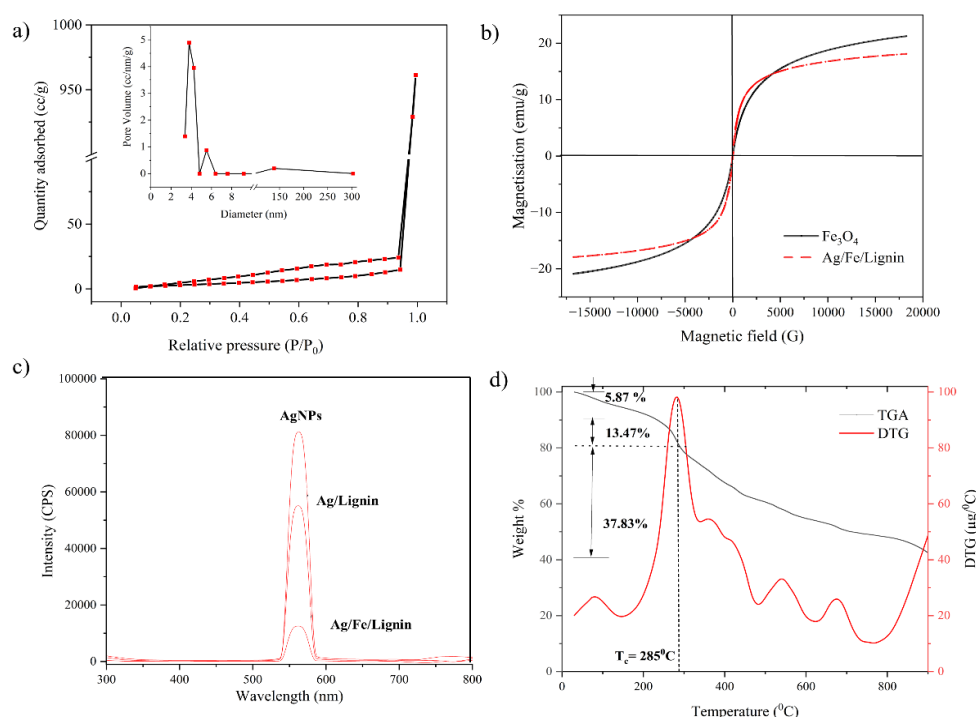


Figure 4.26 a) N₂ adsorption/desorption isotherm plot and pore size distribution for Ag/Fe/Lignin b) VSM spectra for Ag/Fe/Lignin and Fe₃O₄ c) PL spectra for AgNPs, Ag/Lignin and Ag/Fe/Lignin d) TGA graph analysis for Ag/Fe/Lignin

f) **VSM analysis:** When a magnetic field is present, superparamagnetic particles are strongly magnetised and not magnetised when the field is absent. The main characteristic of a superparamagnetic particle is the lack of a hysteresis loop in the VSM profile of the particles. The alignment of all magnetic spin in a sample is used to calculate the saturation magnetization, which decreases with nanoparticle size. The VSM was used to examine the composite's superparamagnetic characteristics by analysing the magnetic properties of Ag/Fe/Lignin and Fe₃O₄. Figure 4.26b depicts the

magnetization hysteresis loops of Ag/Fe/Lignin. These particles are superparamagnetic at room temperature, and hysteresis loops show no hysteresis. The saturation magnetisation (M_s) values of Ag/Fe/Lignin and Fe_3O_4 are 22.5 and 17.5 emu/g, respectively, at 25 °C. The reduction in the M_s value is due to the presence of the lignin and silver content. The M_s values are appropriate for water treatment applications where the M_s values range between 7 and 22 emu.g⁻¹ (Shagholani et al. 2015).

g) Photoluminescence (PL) spectroscopy: PL analysis is a useful tool for analysing the excitation, transfer and recombination of holes and electrons in semiconductors which are generated by light irradiation. The room-temperature PL spectra of the AgNPs, Ag/Lignin, and Ag/Fe/Lignin prepared are shown in Figure 4.26c. The PL spectra of the Ag/Fe/Lignin had only a strong UV emission peak around 585 nm. Lower peak intensity shows the lower recombination effect of formed holes and electrons. The weaker point in the catalyst used for photocatalysis is its recombination effect; thus, this should be less for a better photocatalyst (Zhao et al. 2017). Figure 4.26c represents the PL spectra of AgNPs, Ag/Lignin and Ag/Fe/Lignin at a wavelength of 355 nm. The PL intensity reduces as: AgNPs > Ag/Lignin > Ag/Fe/Lignin shows that the recombination effect of Ag/Fe/Lignin is reduced compared to AgNPs and Ag/Lignin thus, the effect of photocatalysis is more effective in the case of the composite than AgNP and silver with lignin composite. Thus, the photogenerated electrons and holes will be more in the case of Ag/Fe/Lignin and thus improves the photocatalytic effect. Thus the photo generation rate will be in the order of Ag/Fe/Lignin > Ag/Lignin > L. A similar type of PL spectra behaviour was reported by Zhao et al., (2017).

h) TGA analysis: The TGA thermogram of the composite is shown in Figure 4.26d. TGA curves give the reduction in weight showing multi-step thermal degradation. Initial stage of thermal degradation happened at 150°C, which was attributed to the evaporation of moisture present in the catalyst (Shankar and Rhim 2017). Ag/Fe/Lignin was thermally stable (<20% weight loss) up to 285°C. The highest thermal degradation was observed between 285 °C and 330 °C due to the decomposition of lignin. The increased thermal stability of the composite was especially due to the thermally stable silver and magnetic iron particles on lignin.

i) **Zero-point charge (ZPC):** The concept known as zero-point charge (ZPC) refers to the adsorption of charged materials on the adsorbate in a given solution under specific conditions where the density of electrical charge of the surface is zero. ZPC is, in other words, the pH at which a substance has a net charge of zero. Understanding how charged species interact at a material's surface due to electrostatic attraction requires knowledge of this crucial characteristic. It is confirmed that the surface acquires a net anionic charge at $\text{pH} > \text{pH}_{\text{ZPC}}$ and attracts cationic or positively charged materials. Anionic species are drawn to the surface when $\text{pH} < \text{pH}_{\text{ZPC}}$ and acquires a net positive charge. The graph of final pH vs initial pH and the pH for ZPC (pH_{ZPC}) was determined at the intersection point. pH_{ZPC} for Ag/Fe/Lignin was found to be ≈ 6.8 , shown in Figure 4.27. The previously mentioned observation shows that the Ag/Fe/Lignin surface structure acquires a net negative charge at neutral ($\text{pH} = 7$) or alkali ($\text{pH} = 10$), attracts the cationic dye due to electrostatic attraction, and efficiently degrades the dyes in the presence of H_2O_2 and sunlight due to the presence of more hydroxyl radicals ($\text{OH}\cdot$). Ag/Fe/Lignin has a zero-point charge of 6.8, and its surface behaves as positively charged in acidic solutions ($\text{pH} < 6.8$) and negatively charged in media with pH above 6.8.

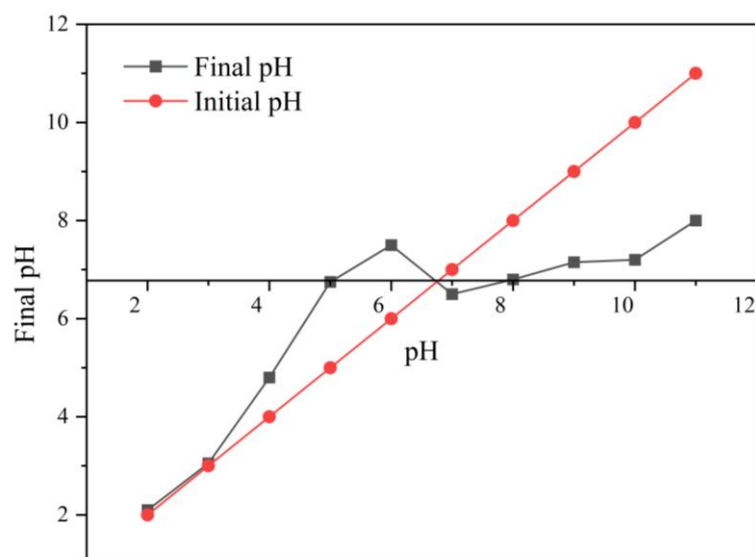


Figure 4.27 Zero-point charge of Ag/Fe/Lignin

4.5.3 Photocatalytic degradation of dyes using Ag/Fe/Lignin

Ag/Fe/Lignin is used for the degradation analysis of the anionic (RBBR), cationic (MV) and zwitterionic (RhB) dyes.

a) Effect of pH: The major issue of AgNPs for dye degradation was found in the case of a high concentration of zwitterionic dye RhB. Thus, to rectify this, further analyses were carried out with alkali lignin derived from NSS, lignin and silver composite and the magnetised silver lignin composite. Photocatalytic degradation of dyes with lignin was comparably improved in the acidic range, but the overall efficiency was less; thus, the combination of silver and lignin was analysed, enhancing the degradation from 68% to 80% in the case of RhB dye with an initial concentration of 100 mg/L (Figure 4.28b). To make the catalyst simple to remove with the help of a magnet, the composite is prepared with a combination of magnetised iron, silver and alkali lignin (Ag/Fe/Lignin). This resulted in the removal of the catalyst with a magnet, and the efficiency also improved to 83%. For different pH, dyes with a concentration of 100 mg/L with a dosage of 1g/L of catalyst for three hours are kept under UV light for analysing the effect of pH in case of different catalysts such as AgNPs, lignin, lignin silver composite (Ag/Lignin) and magnetised silver-lignin composite (Ag/Fe/Lignin). In cationic dye MV, compared to AgNPs, Lignin and Ag/Lignin, Ag/Fe/Lignin showed better results, resulting in >90% degradation irrespective of pH (Figure 4.28a). The photocatalytic effect of AgNPs was more sensitive to pH, but in the case of L and Ag/Lignin, the variation of degradation efficiency with respect to pH was comparably less. But in the case of anionic dye, RBBR (Figure 4.28c), the effect of pH was similar in all types of catalysts. However, Ag/Fe/Lignin showed better efficiency compared to the others. The improved efficiency of the Ag/Fe/Lignin composite is due to the better radical formation capacity in the presence of UV light compared to other catalysts (Jana et al. 2020).

b) Effect of Contact time: The photocatalytic degradation of anionic, cationic and zwitterionic dyes by using Ag/Fe/Lignin catalysts is shown in Figure 4.28d. The experimental conditions are catalyst dosage: 1.5 g/l, initial dye concentration: 100 mg/L, and pH: 7. In dark conditions, adsorption of dyes on the catalyst happened and resulted in the removal efficiency in the initial phase, then when it kept under UV

irradiation degradation of dyes was taken place. The degradation efficiency reached the maximum for RBBR and MV dye within a time of 150 min. But in the case of RhB dye, the degradation rate increased at 90 min (78%) then the degradation rate was very low even at 120 min of irradiation, indicating the lower degradation capacity due to the higher intensity and stable structure of the dye compared to the other types of dyes.

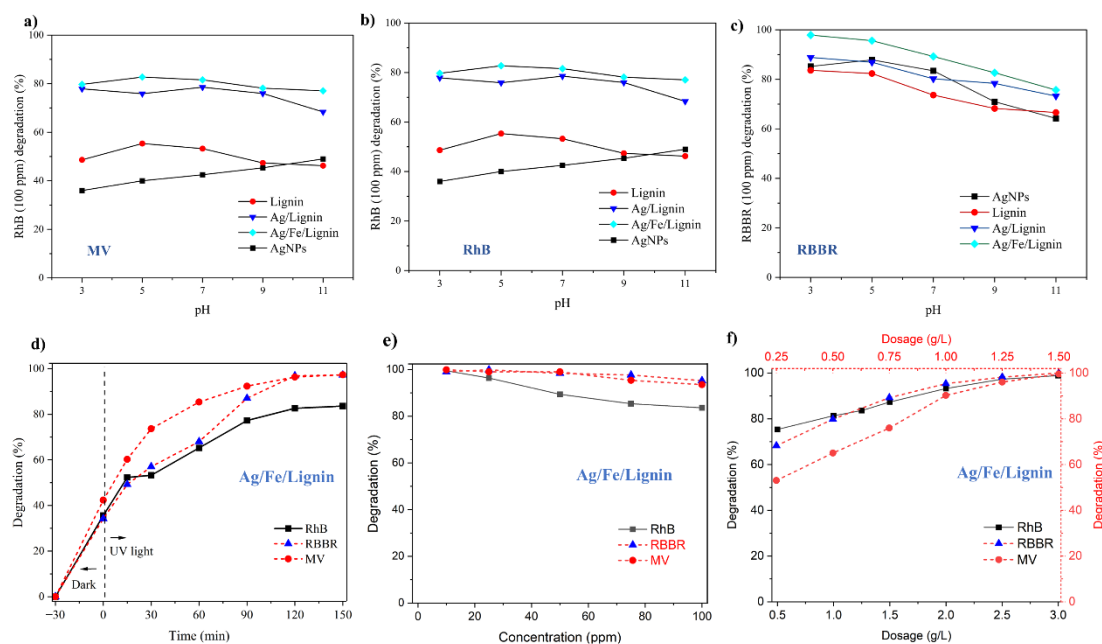


Figure 4.28 Effect of pH for a) MV dye b) RhB dye c) RBBR dye degradation Effect of d) time e) concentration f) dosage on dye degradation using Ag/Fe/Lignin

c) Effect of Concentration: The effect of initial dye concentration on the photocatalytic degradation efficiency of Ag/Fe/Lignin was investigated (Figure 4.28e). Test conducted keeping catalyst dose 1.5 g/L, initial dye concentration 10-100 mg/L and initial pH 7 for 150 min under UV irradiation. It can be observed that the dye degradation efficiency of Ag/Fe/Lignin was decreased from 99.9 - 97% for RBBR and 99.9-95% for MV, and 97-85% for RhB with respect to by increment in dye concentration from 10 to 100 mg/L, after 150 min of reaction time. The increased reduction rate of degradation efficiency with respect to the increase in initial concentration of RhB dye is due to the fluorescent nature of the dye, which results in shading and light scattering effect, thus reducing the UV light penetration through the solution. The adsorbed dye on Ag/Fe/Lignin will not be degraded due to the reduction

in radicals due to the less action of UV light, and further activation of sites on the Ag/Fe/Lignin will not happen due to the adsorbed dye (Jabbar and Ebrahim 2021; Shaikh et al. 2020).

d) Effect of Dosage: The reactive oxidising species (ROS) formation in the photocatalytic processes is mainly due to the presence of a catalyst. Thus, catalyst dosage in the photocatalytic processes plays a major role in the degradation rate (Jabbar and Ebrahim 2021). But catalyst dosage should be regulated to avoid the over usage of catalysts in the process. The experimental parameters were: set to determine the effect of dosage was, photocatalyst dose: 0.5- 3 g/l (RhB) and 0.5- 1.5 g/l (RBBR, MV), initial dye concentration: 100 mg/L, initial pH: 7. After an irradiation time of 150 min, the dye degradation efficiency the samples were analysed using UV-visible double beam spectrophotometer. The increase in the active sites results in the enhancement of dye degradation; thus, the increase in the dosage results in the enhancement of degradation efficiency. For the same RBBR and MV dye concentration, the catalyst required for photocatalytic degradation was comparatively lesser than RhB dye (Figure 4.28f). RhB requires more radicals to break the bonds due to its stable structure. RhB dye degradation enhanced from 75% to 98% with respect to the increase of dosage from 0.5-3g/L. But in the case of RBBR and MV, the degradation happened in a dosage of 1.5 g/L.

Single dye degradation using Ag/Fe/Lignin showed that even in a wide pH range, the degradation shows better response (>85% degradation) compared to other materials like NSS biochar L, Ag/Lignin and AgNPs.

4.5.4 Photocatalytic degradation of a mixture of dyes using Ag/Fe/Lignin

Photocatalytic degradation for a mixture of anionic and cationic dyes is analysed due to its practical relevance (Figure 4.29). A mixture of dyes will get ionised in water and electro-statistically attracted towards the surface of the Ag/Fe/Lignin composite. The pH effect on dye degradation shows that in all ranges of pH, the Ag/Fe/Lignin can degrade more than 80% in the case of 100 mg/L initial concentration of the mixture of dyes (Figure 4.29a). This happens due to the effect of electron-hole pair generation as an effect of UV irradiation and less electron-hole recombination in the case of Ag/Fe/Lignin (Zhao et al. 2017). In the acidic state, the degradation is more effective (Jabbar and Ebrahim 2021). Degradation of the same concentration of the

mixture of dyes is faster than single dye degradation due to the strength reduction of individual dyes by the interactions with differently charged dyes.

Contact time of one hour resulted in 83% degradation efficiency with UV irradiation, and then the degradation efficiency gradually increased up to 94% in 150 minutes (Figure 4.29b). At lower concentrations, the results showed almost complete degradation of dye, but when it comes to a higher initial concentration, the efficiency reduced up to 80% (Figure 4.29c). Lesser the initial concentration of the dye solution, the more radical formation by the Ag/Fe/Lignin and UV action will be enough to degrade the dyes. When the catalytic dosage is increased up to 3 g/L, the degradation is enhanced due to the availability of enough radical formation (Figure 4.29d). The radicals formed by the 1.5g/L of Ag/Fe/Lignin and UV irradiation are not enough to completely degrade the 100 mg/L mixture of dyes in 150 minutes of contact time. To reduce the cost of the process, the catalyst dosage should keep at a minimum value. Hydrogen peroxide can act as an activator for forming radicals by reacting with electrons and holes produced by Ag/Fe/Lignin and UV action; thus, it can improve the degradation efficiency better (Jabbar and Ebrahim 2021).

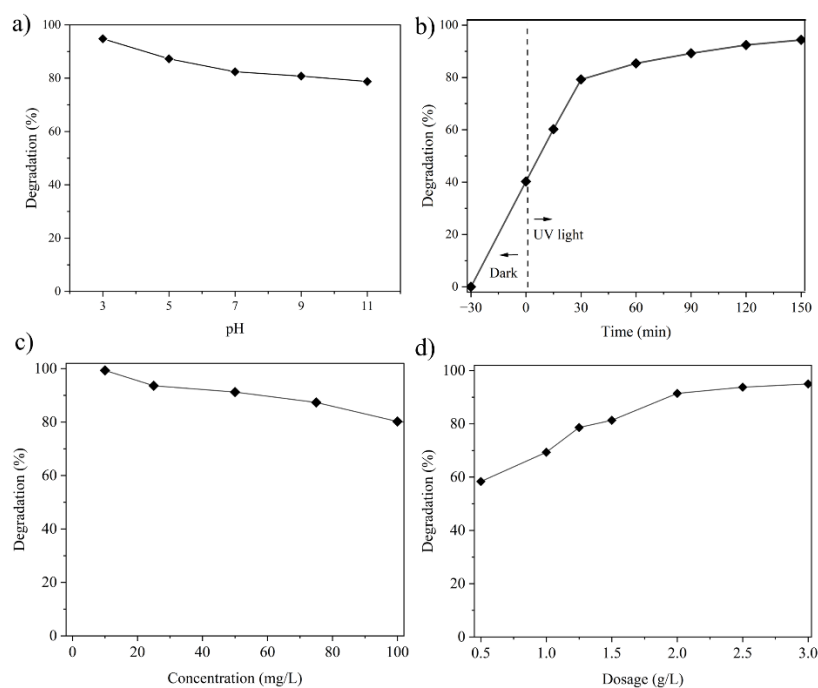


Figure 4.29 Effect of a) pH b) time c) concentration, d) dosage on the degradation of the mixture of dyes using Ag/Fe/Lignin

4.5.5 Effect of H₂O₂ on degradation of a mixture of dyes

To determine the effect of H₂O₂ as an activator on dye degradation, 100 mL mixture of dyes (100 mg/L) was subjected to a set of experiments with a catalyst dosage of 1 g/L and pH of 7. Before keeping under a light source, 1 mL of 30% H₂O₂ is added to the solution and kept for 95 min under UV light. When it is ionised in water, dyes are electrostatically attracted to the surface of the Ag/Fe/Lignin composite. When UV light irradiation happens, the excitation of electrons from the valance band to the conduction band will occur by creating a hole in the valance band. Both of these electrons and holes will react with water and oxygen to form OH •, and these radicals cause the bond breakage of dyes and result in degradation (Figure 4.30a).

In the case of the addition of hydrogen peroxide, an oxidising agent, these electrons and holes will also react with H₂O₂ to form radicals (Rahmat et al. 2019). Thus, the additional radical formation will happen due to the action of H₂O₂ and Ag/Fe/Lignin /UV effect (Jabbar and Ebrahim 2021). Thus, the dye degradation reaches a maximum and is faster in the presence of H₂O₂ and UV light. Due to the increased production of hydroxyl radicals by the combined action of H₂O₂ and UV radiation, the dyes are efficiently degraded in a lesser time of 95 min instead of 150 minutes, and in addition to that, it resulted in the complete degradation of a mixture of dyes of 100 mg/L concentration (Figure 4.30b). But when the study was conducted with only H₂O₂, the degradation was less than 12%. This happens as the degradation possibility is limited to forming radicals through a reaction with oxygen and H₂O₂. The degradation of a mixture of dyes only with H₂O₂ and by means of a catalyst (with and without H₂O₂) with respect to time is shown in Figure 4.30c.

This study also analysed the Ag/Fe/Lignin-UV-H₂O₂ degradation effect at higher concentrations of dyes (Figure 4.30d). From the analysis, it is evident that the combination can result in the degradation of a mixture of dyes of 250 mg/L, resulting in more than 85% degradation efficiency, whereas without H₂O₂, even at 150 mg/L, the degradation was 77%. This shows the effectiveness of combined degradation by the prepared composite and H₂O₂ under UV irradiation.

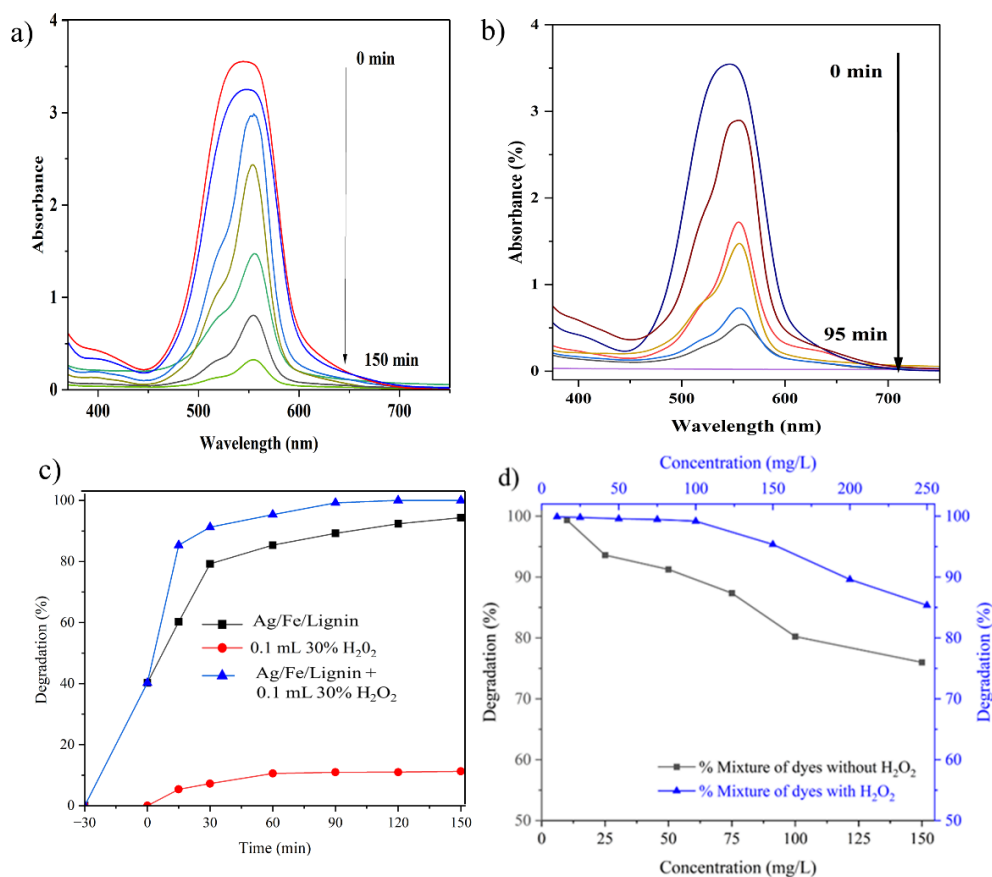


Figure 4.30 a) UV-visible spectra for the mixture of dyes degradation using Ag/Fe/Lignin b) UV-visible spectra for the mixture of dyes degradation using Ag/Fe/Lignin with H₂O₂ c) Effect of time for degradation of the mixture of dyes d) Effect of initial concentration for degradation of the mixture (catalyst and H₂O₂)

4.5.6 Kinetic and isotherm study for removal of a mixture of dyes

Photocatalytic degradation of dyes depends on the dye adsorbed onto the catalyst; higher adsorption capacity or catalytic affinity towards dye molecules leads to better photocatalytic degradation of dyes. The isotherm analysis is conducted to determine the mechanism behind the bonding of the dye to the catalyst. The mixture of dye solution at varying concentrations of 10 mg/L to 200 mg/L with 1g/L of Ag/Fe/Lignin with and without the addition of H₂O₂ (1 mL/100 mL) are analysed to conduct an isotherm study (Figure 4.31a). Langmuir isotherm (Figure 4.31b), Freundlich (Figure 4.31c) and Temkin isotherm models (Figure 4.31d) were considered for this study. Langmuir isotherm resulted in a higher correlation coefficient ($R^2=0.99$

for without H₂O₂ and 0.98 for with H₂O₂) (Table 4.18) than other isotherm models, which confirms it follows homogenous-monolayer adsorption. The degradation happens to the dyes bound on active sites by radical action. Then the other dye molecule will get adsorbed to the vacant active site, followed by the dye degradation by photocatalytic activity. The continuous reactions result in the total degradation of dyes by the photocatalyst.

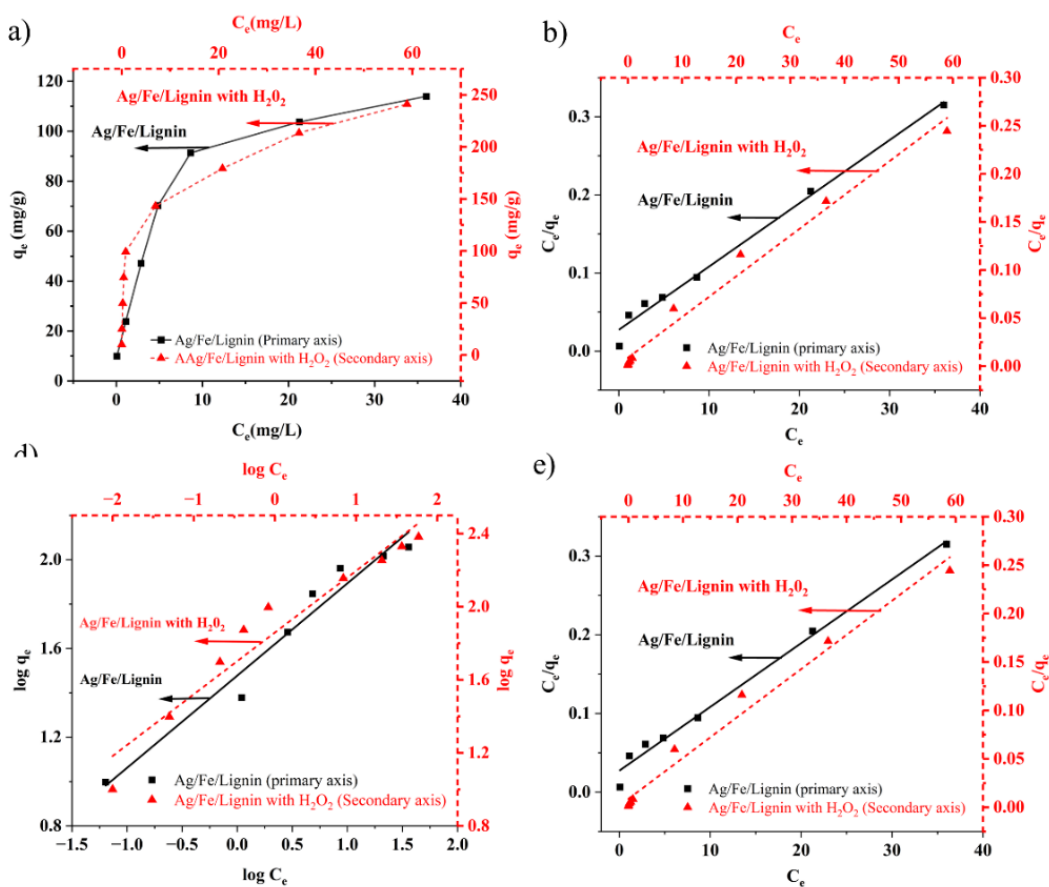


Figure 4.31 The plots of a) Adsorption isotherm b) Langmuir isotherm c) Freundlich isotherm d) Temkin isotherm of the mixture of dyes with and without H₂O₂

The degradation kinetics was assessed for both cases (without H₂O₂ and with H₂O₂) to determine how quickly the adsorption and degradation can happen and to determine how the interaction with the dye and catalyst happens and results in degradation (Figure 4.32a). Pseudo-first-order kinetic model (Figure 4.32b), Pseudo-second-order kinetic model (Figure 4.32c), Interparticle diffusion kinetic model (Figure 4.32d) and Elovich kinetic model (Figure 4.32e) are analysed for this study. The kinetic model is more

fitted to the pseudo-second-order mechanism ($R^2=0.96$ for without H_2O_2 and 0.99 for with H_2O_2) (Table 4.18). The findings indicated that the dye concentration and catalyst dosage affect the degradation process. Therefore, as the catalyst dose increases, the degradation efficiency improves (Ghorbani et al. 2023).

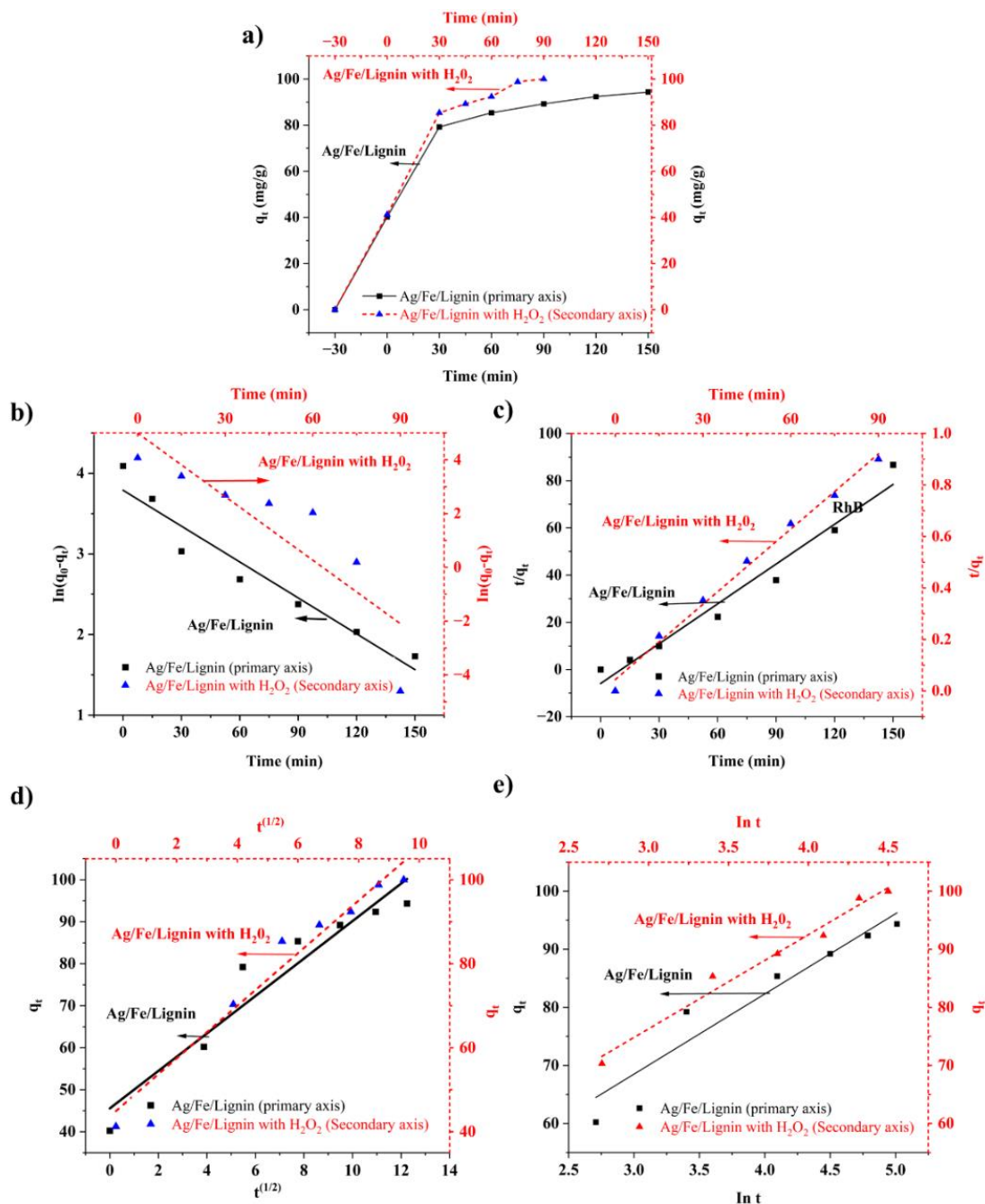


Figure 4.32 a) Adsorption kinetics b) Pseudo-first-order kinetic model c) Pseudo-second-order kinetic model d) Interparticle diffusion kinetic model e) Elovich kinetic model for degradation of mixture of dyes with and without H_2O_2

Table 4.18 Parameters of kinetic and isotherm study for the mixture of dyes with and without H₂O₂

		Parameter	Mix	Mix with H ₂ O ₂
Adsorption kinetics models	Pseudo-first-order	q_e (mg/g)	44.256	146.94
		K_1 (1/min)	0.015	0.08
		R^2	0.94	0.78
		RSS	2.80	1.25
	Pseudo-second-order	q_e (mg/g)	21.74	111.11
		K_2 (g/mg/min)	0.05	0.001
		R^2	0.96	0.99
		RSS	0.899	0.0043
	Interparticle diffusion	c	45.5	44.91
		k_d	4.45	6.2
		R^2	0.92	0.96
		RSS	18.8	77.7
	Elovich Kinetic model	α (mg/g/min)	0.07	0.06
		B (g/mg)	97.7	89.24
		R^2	0.93	0.97
		RSS	52.31	12.53
Adsorption isotherm models	Langmuir	q_{max} (mg/g)	83.33	125.00
		k_l (L/mg)	0.25	0.33
		R^2	0.99	0.98
		RSS	0.001	0.001
	Freundlich	k_f (L/mg)	4.34	6.36
		n	2.41	2.95
		R^2	0.96	0.94
		RSS	0.03	0.09
	Temkin	k_t (L/mg)	11.44	56.87
		b_t (J/mol)	17.81	26.69
		R^2	0.88	0.96
		RSS	10.90	20.61

4.5.7 Mechanism of dye degradation using Ag/Fe/Lignin composite

Initially, the dyes are adsorbed onto the Ag/Fe/Lignin composite. The degradation of dyes is then caused by photocatalytic activity, which causes electron excitation to the conduction band and forms holes in the valence band. The holes and electrons will react with oxygen and water to form $O_2^{\cdot-}$ and OH^{\cdot} ; these radicals lead to the breakage of bonds in the molecular structure of dyes by dealkylation, dihydroxylation and deamination. The degradation products are further mineralised to CO_2 , H_2O , and additional ions such as NH_4^+ , NO_3^- , SO_4^{2-} etc. (Budnyak et al. 2021). The mechanism behind the degradation of a mixture of dyes is schematically represented in Figure 4.33. The reactions that happen in Ag/Fe/Lignin under UV light are listed below (eq. 4.3-4.7):



Adding H_2O_2 will result in reactions with formed electrons and holes, resulting in additional radicals. Reactions in the presence of hydrogen peroxide (eq. 4.8-4.12):



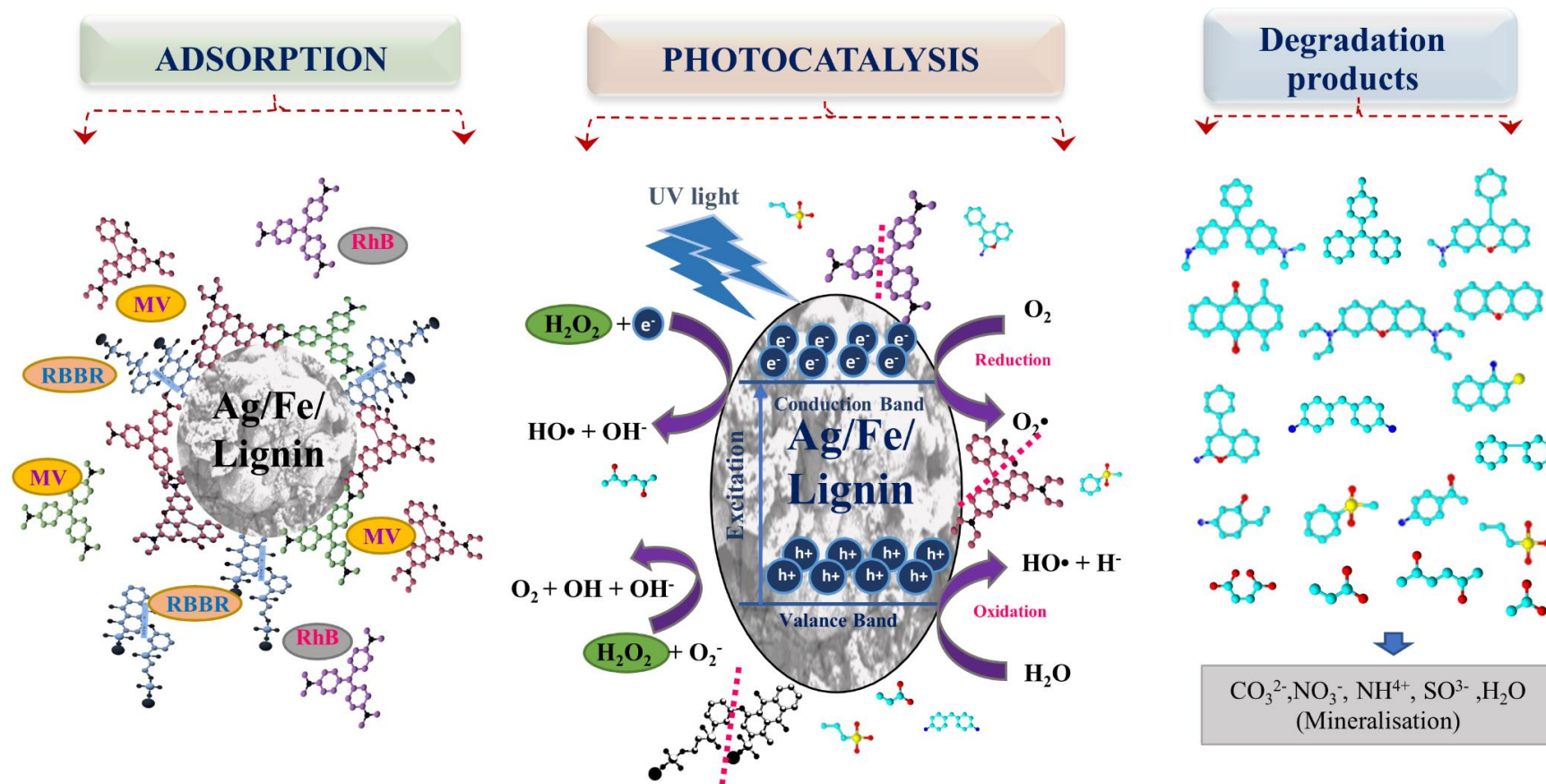


Figure 4.33 Schematic representation of possible degradation mechanism of dyes

The UPLC–MS system detected m/z values for RhB, RBBR, and MV dye mixture in different intervals of time; it determined different products by photocatalytic degradation. The fragmentation pattern obtained by HRLC-MS analysis is shown in Figure 4.34. The degradation pathway of RhB, RBBR, and MV dyes is composed of four main processes, according to previous studies and the findings of this study. This includes deamination, dihydroxylation, deamination, and cleavage of the dyes by the action of radicals produced during the photocatalytic process.

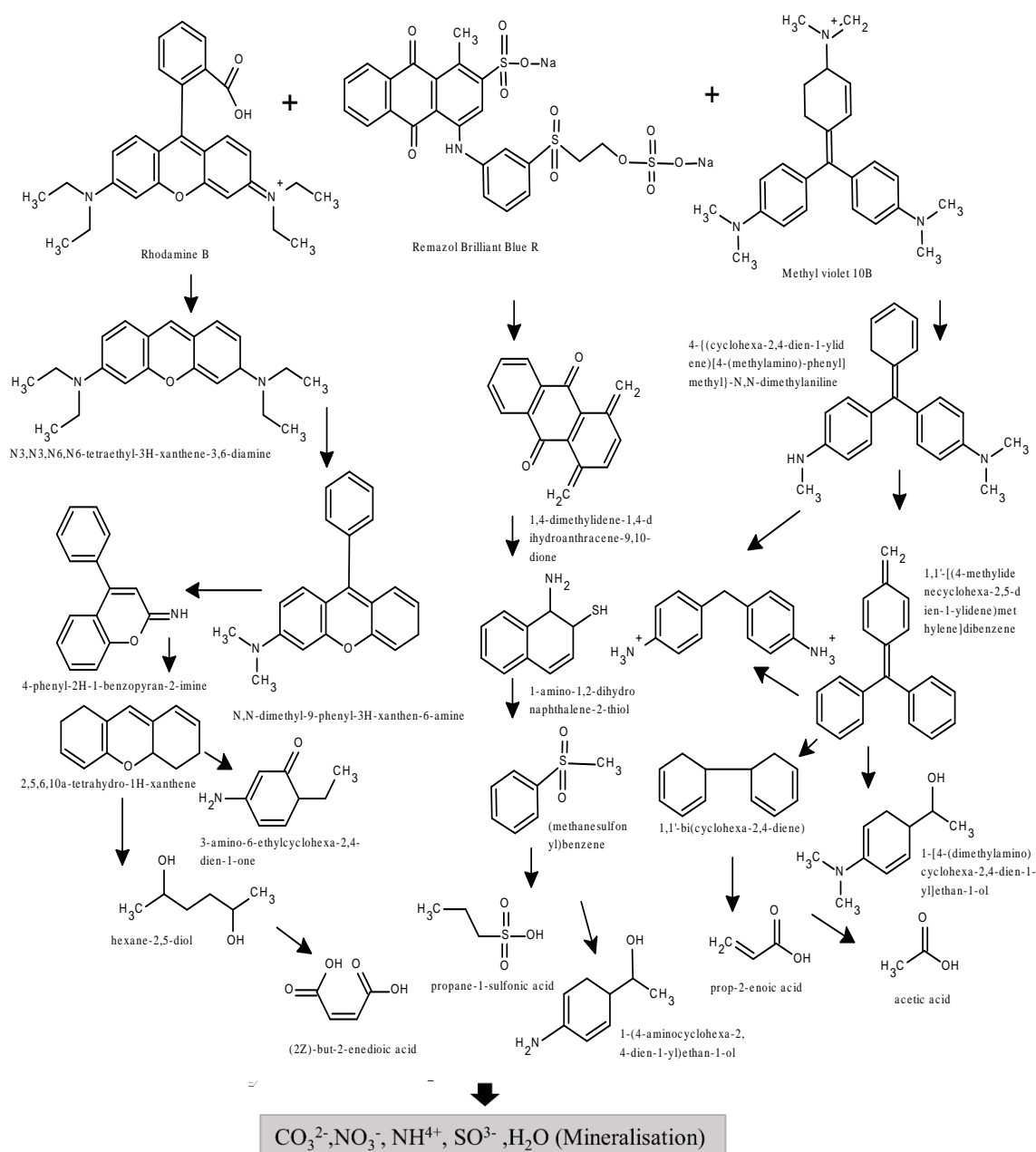


Figure 4.34 Possible pathway mechanism for the degradation of the mixture of dyes using Ag/Fe/Lignin

N,N-dimethyl-9-phenyl-3H-xanthen-6-amine ($m/z=301$) by C-N group cleavage of RhB dye, further degradation products like N3,N3,N6,N6-tetraethyl-3H-xanthene-3,6-diamine ($m/z = 323$), 4-phenyl-2H-1-benzopyran-2-imine ($m/z = 220$), 2,5,6,10a-tetrahydro-1H-xanthene ($m/z = 184$), 3-amino-6-ethylcyclohexa-1,5-dien-1-ol ($m/z = 140$), hexane-2,5-diol and hexane-2,5-diol are resulted by dihydroxylation, deamination and bond cleavage. Eliminating amino and sulphonic groups from the RBBR dye resulted in the products with m/z value of 233 (1,4-dimethylidene-1,4-dihydroanthracene-9,10-dione). Further degradation occurred by the breaking of the aromatic group and resulted in smaller products like 1-amino-1,2-dihydronaphthalene-2-thiol ($m/z = 177$), (methanesulfonyl)benzene ($m/z=157$), 1-(4-aminocyclohexa-2,4-dien-1-yl)ethan-1-ol ($m/z=139$), and propane-1-sulfonic acid ($m/z=125$). Initially the degradation of MV dye is caused by deamination (Favaro et al. 2012), which results in the formation of products like 4-((cyclohexa-2,4-dien-1-ylidene)[4-(methylamino)phenyl]methyl)-N,N-dimethylaniline ($m/z= 316$) and 1,1'-[(4-methylidenecyclohexa-2,5-dien-1-ylidene)methylene]dibenzene ($m/z= 256$). Further degradation happened by cleavage of the aromatic ring and resulted in the formation of organic compounds like 4,4'-methylenedibenzenaminium ($m/z = 200$), 1,1'-bi(cyclohexa-2,4-diene) ($m/z= 158$), 1-(4-aminocyclohexa-2,4-dien-1-yl)ethanol ($m/z = 139$), prop-2-enoic acid and acetic acid.

Thus the intermediates produced during the mixture of dyes, including sulphonic acid prop-2-enoic acid, but-2-enedioic acid and acetic acid. The organic intermediate products formed by the dye degradation were further mineralized to produce CO_3^{2-} , NO_3^- , NH_4^+ , SO_3^- , CO_2 , and water.

4.5.8 Reusability study for Ag/Fe/Lignin composite used in dye degradation

The reusability of magnetic Ag/Fe/Lignin composite was carried out to analyse its potential for the application of dye removal. 100 mL of a mixture of dye (concentration: 100 mg/L) were subjected to a set of experiments with a catalyst dosage of 1 g/L and pH of 7 with 1 mL of 30% H_2O_2 for 95 min of UV irradiation. The degradation capacity of the Ag/Fe/Lignin has tested up to five degradation cycles, as shown in Figure 4.35. The catalyst is recovered after each cycle using an external magnet. It has resulted in better degradation efficacy even without regeneration with ethanol; thus, the catalyst can directly use after removing it with a magnet and using it for the next cycle of dye

degradation. Approximately 95.5% of degradation efficiency is maintained after five degradation cycles. It suggests that the Ag/Fe/Lignin can be utilised as a recyclable catalyst with high stability to degrade the dyes.

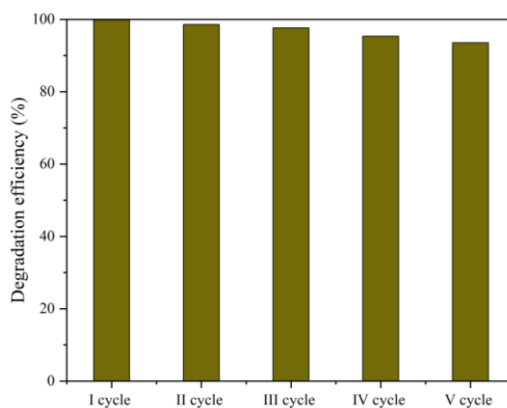


Figure 4.35 Reusability study of Ag/Fe/Lignin for degradation of the mixture of dyes

4.5.9 Comparison with other photocatalytic studies conducted for the degradation of dyes

The findings are compared with studies conducted by various researchers for dye removal using lignin-based catalysts. Table 4.19 shows that the synthesised photocatalyst has high dye degradation efficiency for a mixture of dyes with anionic cationic and zwitterionic dyes. Lignin-based catalysts, reported in previous studies, are analysed only for single dyes, resulting in a better degradation efficiency with lower initial concentration.

Unlike the Fenton process, which generates sludge and operates within a limited pH range, the catalyst can break down dyes in various ionic forms when exposed to UV light in presence of less amount of hydrogen peroxide, without producing sludge. This efficient degradation is attributed by the catalyst, with energy consumption occurring due to continuous stirring and UV light exposure. Approximately 5 units of electricity are needed for one set of photocatalytic degradation process. (You-Ji and Wei 2011). Instead of a series of treatments that contribute to a higher carbon footprint in in water treatment plants especially for textile waste water treatment, the adoption of effective photocatalytic degradation can eliminate additional pollution.

Table 4.19 Comparative study with other lignin based photocatalysts

Composite	Base material	Pollutant	Removal conditions	Reference
Lignin- BiVO ₄ -C nanocomposite	Based on Sodium lignosulphonate	oxytetracycline hydrochloride	Dosage: 0.2g/L, 60 min dark, 90 min 300 V xenon lamp, 66% degradation, Concentration: 10 mg/L	(Wang et al. 2020)
C- modified TiO ₂ using lignin as a carbon precursor	Lignin with TiO ₂	Acetaminophen	Xe-Lamp, 250 mg/L dosage for 5 mg/L concentration 1 hrs complete degradation	(Gómez-Avilés et al. 2019)
Lignin-mediated AgNP Synthesis	Lignosulphonate	Reactive Yellow 4G	1mL of 1% H ₂ O ₂ 100 ml 20 mg/L dye, 10 mg/L dosage, 4 min 100%	(Saratale et al. 2022)
Fe ₃ O ₄ @LigA/Cu	kraft lignin	methylene blue	3 mL (1 mg/mL) of catalyst to 2.5 mL dye (20 mg/L), 0.2 mL of NaBH ₄ (0.05 M), 4 MIN >99%	(Mohami et al. 2022)
Carbon-lignin/ Zinc Oxide	Lignin	methylene blue	96.272% degradation performance are pH 7, 600 °C calcination temperature, and 90 min	(Ulum et al. 2020)
TiO ₂ nanoparticle with lignin	Alkali lignin	phenol	100% in 160 min, 50 mg/L, 1g/L of catalyst 30min dark and 160 min 8 W mercury lamp	(Chen et al. 2016)
Ag/Fe/Lignin	NSS-based alkali lignin	A mixture of RBBR, RhB, MV	100% in 90 min for 100 mg/L concentration 85% for 250 mg/L concentration In 100 mL, 0.1 g of Ag/Fe/Lignin with 1 mL 30% H ₂ O ₂ under UV light	This study

4.6 Summary

The potential of NSS-based materials to remove three different classes of dyes, especially anionic (RBBR dye), cationic (MV dye), and zwitterionic (RhB dye) are analysed in this study. The NSS-based biochar resulted in better removal efficiency in the case of RBBR dye removal but less effect on the removal of cationic (MV) and zwitterionic dyes (RhB dye). Degradation results of these dyes using AgNPs synthesised with NSS extract resulted in better degradation efficiency for cationic and anionic dyes under UV light, but it resulted in better degradation efficiency for zwitterionic dye only at very low concentrations. Synthesised AgNP catalysts cannot perform better degradation in the case of RhB dye, and these adsorbents/catalysts from the solution after the treatment. Due to these issues, a composite of silver and lignin (extracted from NSS) induced by magnetic property (to remove the catalyst using a magnet) was synthesized and analyzed for the degradation of these dyes. This resulted in improved degradation efficiency in all cases of the dyes, and the degradation of a mixture of these dyes resulted in 94% degradation efficiency. Further improvement of the process is made by adding an activator (H_2O_2), which results in faster and better degradation even at higher concentrations of the mixture of dyes. The reusability study showed that the catalyst did not lose more than 5% of its degradation efficiency even after five cycles of dye degradation using the same catalyst.

CHAPTER 5

CONCLUSIONS

In the present study, to check the combined removal efficiency of anionic, cationic and zwitterionic dyes in wastewater, removing these three types of dyes with materials based on NSS is tested. The results are summarised below:

1. Biochar prepared from NSS has higher thermal stability and a surface with micropores and nanopores. While RhB and MV dyes had restricted adsorption on prepared NSS biochar, anionic RBBR dye was removed more effectively. Optimisation study for RBBR dye removal using NSS biochar showed that RBBR dye with an initial concentration of 100 mg/L is effectively treated at an adsorbent dosage of 2.85 g/L, a pH of 10, and a contact duration of 110 min; this resulted in removal efficiency of 93.41%.
2. Aqueous NSS extract, which is identified with reducing and capping agents required for nanoparticle formation, is utilised to synthesise AgNPs catalyst for degrading dyes. After optimising nanoparticle synthesis processes, spherical-shaped nanosized (10 nm to 60 nm) silver with a surface area of 88.16 m²/g was formed with NSS extract and silver salt in the presence of sunlight. DPPH and hydroxyl radical scavenging activity of synthesised AgNPs indicate its suitability as an antioxidant with a percentage scavenging activity of more than 85%. The bacterial inhibition of these AgNPs (50 µg/mL) towards gram-positive and gram-negative bacteria (IZD ≥ 15 mm) compared to ampicillin of 50 µg/mL (IZD ≤ 13 mm) promotes the applicability in antibacterial fields. The degradation efficiency for RhB dye (initial concentration 10 mg/L) was 94%, for RBBR dye (initial concentration: 100 mg/L) was 92%, and for MV dye (initial concentration: 100 mg/L) was 88% using AgNPs. This demonstrates the ability to use synthesised AgNPs as a photocatalyst to degrade dyes in the different ionic states. After the photocatalytic degradation process, the degradation products result in the simple organic compounds, viz. water, carbon dioxide and residues by deamination, demethylation, dihydroxylation and cleavage of the aromatic ring through radical action. The mechanism behind the photocatalytic degradation shows that the hydroxyl radical production under UV

light resulted in the degradation of dyes. The dye degradation application is restricted for RhB dye if the concentration is more than 10 mg/L (less than 70% degradation efficiency).

3. Higher lignin and phenolic content in NSS are utilised for the catalyst preparation. Considering the wide range of lignin properties, it was extracted using alkali; the optimised extraction happened with 12% of sodium hydroxide, resulting in a 33% yield. Magnetised silver-lignin composite was prepared to make a better catalyst with magnetic properties (17.5 emu/g) to make it easier to separate after treatment. The. The utilisation of Ag/Fe/Lignin resulted in better degradation of all three types of dyes and even for a mixture of these dyes (94% degradation efficiency for 100 mg/L). The improved degradation efficiency (94% to 100%) in less time (reduced to 95 min from 150 min) resulted in the presence of H₂O₂ and the catalyst. According to reusability studies, 100 mg/L of a dye mixture degraded at more than 95% even after five degradation cycles. The affinity of dyes towards the catalyst increases photocatalytic degradation. The mechanism behind the degradation to simple organic compounds is through breaking the bonds by deamination, demethylation, dihydroxylation and cleavage of the aromatic ring by radical action. In the presence of H₂O₂ and UV light due to the generation of more hydroxyl radicals (OH•), the degradation happens more rapidly, even at higher concentrations of a mixture of dye solution. This promotes the application of prepared catalysts for industrial wastewater treatment, especially textile wastewater.

Remediation of wastewater from the textile sector can be successful if the pollutants are effectively degraded rather than just separated. The degradation of a mixture of dyes was successfully expedited by the addition of hydrogen peroxide while under the influence of UV light using a composite made from NSS-agricultural refuse. The research results in the use of NSS-based materials in the treatment of textile wastewater.

Future study

- The preparation of lignin composite with AgNPs and magnetic nanoparticles can be optimised to get better results for sunlight-mediated photocatalytic studies. The study can be extended to check the yield of lignin with different pre-treatments and lignin modifications in order to improve the properties of catalyst.
- Even though the maximum efficiency is attained in UV light, considering the availability of natural sources of light, the effectiveness of Ag/Fe/Lignin in sunlight in the presence of H₂O₂ can be analysed and optimised for different factors affecting the degradation of dyes.
- Polymer composite-like sponges have more adsorption capacity than normal powder-type adsorbents, but the polymers used for the composite preparation themselves create environmental pollution. Thus, this study is limited to the formation of the normal composite. But the study can be extended to the formation of sponge-type composites with natural polymers or by considering lignin as a binding agent and using suitable additives to make stable polymer composite.
- For large-scale applications with even higher concentrations of pollutants, a combination of electrodes using lignin composite with UV light supply can be analysed.
- The degradation efficiency of emerging pollutants such as pharmaceuticals, antibiotic resistance genes, pesticides and dyes specifically for individual industries can be analyzed using Ag/Fe/Lignin within a reactor setup.

REFERENCES

- Abebe, B., Murthy, H. C. A., and Amare, E. (2018). 'Summary on Adsorption and Photocatalysis for Pollutant Remediation: Mini Review'. *J. Encapsulation Adsorpt. Sci.*, 08(04), 225–255.
- Agarwal, U. P., McSweeney, J. D., and Ralph, S. A. (2011). 'FT-Raman investigation of milled-wood lignins: Softwood, hardwood, and chemically modified black spruce lignins'. *J. Wood Chem. Technol.*, 31(4), 324–344.
- Ahmad, M. A., Eusoff, M. A., Oladoye, P. O., Adegoke, K. A., and Bello, O. S. (2020a). 'Statistical optimization of Remazol Brilliant Blue R dye adsorption onto activated carbon prepared from pomegranate fruit peel'. *Chem. Data Collect.*, 28, 100426.
- Ahmad, W., Qaiser, S., Ullah, R., Mohamed Jan, B., Karakassides, M. A., Salmas, C. E., Kenanakis, G., and Ikram, R. (2020b). 'Utilization of Tires Waste-Derived Magnetic-Activated Carbon for the Removal of Hexavalent Chromium from Wastewater'. *Materials (Basel)*, 14(1), 34.
- Ahmed, M. J. K., Ahmaruzzaman, M., and Reza, R. A. (2014). 'Lignocellulosic-derived modified agricultural waste: Development, characterisation and implementation in sequestering pyridine from aqueous solutions'. *J. Colloid Interface Sci.*, 428, 222–234.
- Akpor, O., Edewor-Kuponiya, T., Nwonuma, C., and Amira, O. (2013). 'Phosphate and Nitrate Removal from Aqueous Solution by Carbonated and Uncarbonated African Nutmeg (*Monodora*)'. *J. Environ. Earth Sci.*, 3(10), 99–109.
- Al-Gheethi, A. A., Azhar, Q. M., Senthil Kumar, P., Yusuf, A. A., Al-Buriahi, A. K., Radin Mohamed, R. M. S., and Al-shaibani, M. M. (2022). 'Sustainable approaches for removing Rhodamine B dye using agricultural waste adsorbents: A review'. *Chemosphere*, 287(P2), 132080.
- Al-Kahtani, A. A. (2017). 'Photocatalytic Degradation of Rhodamine B Dye in Wastewater Using Gelatin/CuS/PVA Nanocomposites under Solar Light Irradiation'.

J. Biomater. Nanobiotechnol., 08(01), 66–82.

Al-Zahrani, S. S., and Al-Garni, S. M. (2019). ‘Biosynthesis of Silver Nanoparticles from *Allium ampeloprasum* Leaves Extract and Its Antifungal Activity’. *J. Biomater. Nanobiotechnol.*, 10(01), 11–25.

Alipour, A., and Lakouarj, M. M. (2019). ‘Photocatalytic degradation of RB dye by CdS-decorated nanocomposites based on polyaniline and hydrolyzed pectin: Isotherm and kinetic’. *J. Environ. Chem. Eng.*, 7(1), 102837.

Alshehri, A. A., and Malik, M. A. (2020). ‘Phytomediated photo-induced green synthesis of silver nanoparticles using *Matricaria chamomilla* L. and its catalytic activity against rhodamine B’. *Biomolecules*, 10(12), 1–24.

Amal, M. S., Mosad, A. G., Mohamed, S. A.-A., Hassan, M. F. M., Omar, M. K., Ahmed, K. E.-Z., and Mamdouh, A.-M. (2017). ‘Chemical constituents and biological activities of different solvent extracts of *Prosopis farcta* growing in Egypt’. *J. Pharmacogn. Phyther.*, 9(5), 67–76.

Anooj, E. S., Suganthi, V., and Praseetha, P. K. (2019). ‘Synthesis and characterization of graphene quantum dots from turmeric powder (*Berberis aristata*) and its biomedical applications’. *Indian J. Public Heal. Res. Dev.*, 10(7), 1239–1243.

Ansar, S., Tabassum, H., Aladwan, N. S. M., Naiman Ali, M., Almaarik, B., AlMahrouqi, S., Abudawood, M., Banu, N., and Alsubki, R. (2020). ‘Eco friendly silver nanoparticles synthesis by *Brassica oleracea* and its antibacterial, anticancer and antioxidant properties’. *Sci. Rep.*, 10(1), 1–12.

Aravind, M., Ahmad, A., Ahmad, I., Amalanathan, M., Naseem, K., Mary, S. M. M., Parvathiraja, C., Hussain, S., Algarni, T. S., Pervaiz, M., and Zuber, M. (2021). ‘Critical green routing synthesis of silver NPs using jasmine flower extract for biological activities and photocatalytic degradation of methylene blue’. *J. Environ. Chem. Eng.*, 9(1), 104877.

Ashiq, H., Nadeem, N., Mansha, A., Iqbal, J., Yaseen, M., Zahid, M., and Shahid, I. (2022). ‘G-C₃N₄/Ag@CoWO₄: A novel sunlight active ternary nanocomposite for potential photocatalytic degradation of rhodamine B dye’. *J. Phys. Chem. Solids*, 161,

110437.

Ashokan, A. P., Paulpandi, M., Dinesh, D., Murugan, K., Vadivalagan, C., and Benelli, G. (2017). 'Toxicity on Dengue Mosquito Vectors Through Myristica fragrans-Synthesized Zinc Oxide Nanorods, and Their Cytotoxic Effects on Liver Cancer Cells (HepG2)'. *J. Clust. Sci.*, 28(1), 205–226.

Atas, M. S., Dursun, S., Akyildiz, H., Citir, M., Yavuz, C. T., and Yavuz, M. S. (2017). 'Selective removal of cationic micro-pollutants using disulfide-linked network structures'. *R. Soc. Chem.*, 7, 25969–25977.

Auwal, M. S., Saka, S., Mairiga, I. A., Sanda, K. A., Shuaibu, A., and Ibrahim, A. (2014). 'Preliminary phytochemical and elemental analysis of aqueous and fractionated pod extracts of *Acacia nilotica* (Thorn mimosa)'. *Vet. Res. forum an Int. Q. J.*, 5(2), 95–100.

Aziz, N. S., Sofian-Seng, N. S., and Wan Mustapha, W. A. (2018). 'Functional properties of oleoresin extracted from white pepper (*Piper nigrum* L.) retting waste water'. *Sains Malaysiana*, 47(9), 2009–2015.

Baker, S., Perianova, O. V., Prudnikova, S. V., Kuzmin, A., Potkina, N. K., Khohlova, O. Y., and Lobova, T. I. (2020). 'Phytogenic Nanoparticles to Combat Multi Drug Resistant Pathogens and Photocatalytic Degradation of Dyes'. *Bionanoscience*, 10(2), 486–492.

Balakrishnan, S., Ibrahim, K. S., Duraisamy, S., Sivaji, I., Kandasamy, S., Kumarasamy, A., and Kumar, N. S. (2020). 'Antiquorum sensing and antibiofilm potential of biosynthesized silver nanoparticles of *Myristica fragrans* seed extract against MDR *Salmonella enterica* serovar Typhi isolates from asymptomatic typhoid carriers and typhoid patients'. *Environ. Sci. Pollut. Res.*, 27(3), 2844–2856.

Balakrishnan, S., Sivaji, I., and Kandasamy, S. (2017). 'Biosynthesis of silver nanoparticles using *Myristica fragrans* seed (nutmeg) extract and its antibacterial activity against multidrug-resistant (MDR) *Salmonella enterica* serovar Typhi isolates'. *Environ. Sci. Pollut. Res.*, 7, 14758–14769.

Bameri, I., Saffari, J., Baniyaghoob, S., and Ekrami-Kakhki, M.-S. (2022). 'Synthesis

of magnetic nano-NiFe₂O₄ with the assistance of ultrasound and its application for photocatalytic degradation of Titan Yellow: Kinetic and isotherm studies'. *Colloid Interface Sci. Commun.*, 48, 100610.

Bankar, A., Joshi, B., Kumar, A. R., and Zinjarde, S. (2010). 'Banana peel extract mediated novel route for the synthesis of silver nanoparticles'. *Colloids Surfaces A Physicochem. Eng. Asp.*, 368(1–3), 58–63.

Barka, N., Ouzaout, K., Abdennouri, M., and Makhfouk, M. El. (2013). 'Dried prickly pear cactus (*Opuntia ficus indica*) cladodes as a low-cost and eco-friendly biosorbent for dyes removal from aqueous solutions'. *J. Taiwan Inst. Chem. Eng.*, 44(1), 52–60.

Bhatia, D., Sharma, N. R., Singh, J., and Kanwar, R. S. (2017). 'Biological methods for textile dye removal from wastewater: A review'. *Crit. Rev. Environ. Sci. Technol.*, 47(19), 1836–1876.

Bilal, M., Rasheed, T., Iqbal, H. M. N., Li, C., Wang, H., Hu, H., Wang, W., and Zhang, X. (2018). 'Photocatalytic degradation, toxicological assessment and degradation pathway of C.I. Reactive Blue 19 dye'. *Chem. Eng. Res. Des.*, 129, 384–390.

Bogdanchikova, N., Kharlanov, A. N., and Kazantsev, S. O. (2019). 'Oxidation of a wood extractive betulin to biologically active oxo-derivatives using supported gold catalysts'. *Green Chem.*, 3370–3382.

Brand-Williams, W., Cuvelier, M. E., and Berset, C. (1995). 'Use of a free radical method to evaluate antioxidant activity'. *LWT - Food Sci. Technol.*, 28(1), 25–30.

Budnyak, T. M., Onwumere, J., Pylypchuk, I. V., Jaworski, A., Chen, J., Rokicińska, A., Lindström, M. E., Kuśtrowski, P., Sevastyanova, O., and Slabon, A. (2021). 'LignoPhot: Conversion of hydrolysis lignin into the photoactive hybrid lignin/Bi₄O₅Br₂/BiOBr composite for simultaneous dyes oxidation and Co²⁺ and Ni²⁺ recycling'. *Chemosphere*, 279, 130538.

Cardoso, I. M. F., Cardoso, R. M. F., Pinto da Silva, L., and Esteves da Silva, J. C. G. (2022). 'UV-Based Advanced Oxidation Processes of Remazol Brilliant Blue R Dye

Catalyzed by Carbon Dots'. *Nanomaterials*, 12(12), 2116.

Chand, K., Jiao, C., Lakhan, M. N., Shah, A. H., Kumar, V., Fouad, D. E., Chandio, M. B., Ali Maitlo, A., Ahmed, M., and Cao, D. (2021). 'Green synthesis, characterization and photocatalytic activity of silver nanoparticles synthesized with *Nigella Sativa* seed extract'. *Chem. Phys. Lett.*, 763, 138218.

Chandra, M., Pawan, A., Bafila, S., Mishra, D., Negi, K., Kumar, R., and Bughani, A. (2020). 'Adsorptive removal of Remazol Brilliant Blue R dye from its aqueous solution by activated charcoal of *Thuja orientalis* leaves : an eco - friendly approach'. *SN Appl. Sci.*, 2(2), 1–10.

Chandra Pragada, S., and Thalla, A. K. (2021). 'Polymer-based immobilized Fe₂O₃–TiO₂/PVP catalyst preparation method and the degradation of triclosan in treated greywater effluent by solar photocatalysis'. *J. Environ. Manage.*, 296, 113305.

Chen, X., Kuo, D. H., Lu, D., Hou, Y., and Kuo, Y. R. (2016). 'Synthesis and photocatalytic activity of mesoporous TiO₂ nanoparticle using biological renewable resource of un-modified lignin as a template'. *Microporous Mesoporous Mater.*, 223, 145–151.

Chen, X., Li, H., Qiao, X., Jiang, T., Fu, X., and He, Y. (2021). 'Agarose oligosaccharide- silver nanoparticle- antimicrobial peptide- composite for wound dressing'. *Carbohydr. Polym.*, 269, 118258.

Cherian, T., Ali, K., Fatima, S., Saquib, Q., Ansari, S. M., Alwathnani, H. A., Al-Khedhairi, A. A., Al-Shaeri, M., and Musarrat, J. (2019). 'Myristica fragrans bio-active ester functionalized ZnO nanoparticles exhibit antibacterial and antibiofilm activities in clinical isolates'. *J. Microbiol. Methods*, 166, 105716.

Chung, I. L. L. M. I. N., Rahuman, A. A., Marimuthu, S., Kirthi, A. V., Anbarasan, K., Padmini, P., and Rajakumar, G. (2017). 'Green synthesis of copper nanoparticles using *Eclipta prostrata* leaves extract and their antioxidant and cytotoxic activities'. *Exp. Ther. Med.* 14, 18–24.

Cleland, G. E., Brady, E., Burgess, J., and Yang, J. (2015). *Determination of Triphenylmethane Dyes and Their Metabolites in Shrimp Using a Modified Quechers*

Extraction and Lc-Ms / Ms.

- Corral-Bobadilla, M., Lostado-Lorza, R., Somovilla-Gomez, F., and Escribano-García, R. (2021). 'Effective use of activated carbon from olive stone waste in the biosorption removal of Fe(III) ions from aqueous solutions'. *J. Clean. Prod.*, (294), 126332.
- Członka, S., Strąkowska, A., Kairyte, A., and Kremensas, A. (2020). 'Nutmeg filler as a natural compound for the production of polyurethane composite foams with antibacterial and anti-aging properties'. *Polym. Test.*, 86, 106479.
- Das, S., Singh, V. K., Dwivedy, A. K., Chaudhari, A. K., Upadhyay, N., Singh, A., Deepika, and Dubey, N. K. (2020). 'Fabrication, characterization and practical efficacy of Myristica fragrans essential oil nanoemulsion delivery system against postharvest biodeterioration'. *Ecotoxicol. Environ. Saf.*, 189, 110000.
- Devatha, C. P., Thalla, A. K., and Katte, S. Y. (2016). 'Green synthesis of iron nanoparticles using different leaf extracts for treatment of domestic waste water'. *J. Clean. Prod.*, 139, 1425–1435.
- Dipankar, C., and Murugan, S. (2012). 'Colloids and Surfaces B : Biointerfaces The green synthesis , characterization and evaluation of the biological activities of silver nanoparticles synthesized from Iresine herbstii leaf aqueous extracts'. *Colloids Surfaces B Biointerfaces*, 98, 112–119.
- Donar, Y. O., Bilge, S., and Sinağ, A. (2020). 'Utilisation of lignin as a model biomass component for preparing a highly active photocatalyst under UV and visible light'. *Mater. Sci. Semicond. Process.*, 118, 105151.
- El-Shamy, A. gamal. (2022). 'Novel in-situ synthesis of nano-silica (SiO₂) embedded into polyvinyl alcohol for dye removal: Adsorption and photo-degradation under visible light'. *Polymer (Guildf.)*, 242, 124579.
- Eprasad, A., Yulizar, Y., Yunarti, R. T., and Apriandanu, D. O. B. (2020). 'Fabrication of Gd₂O₃ nanoparticles in hexane-water system using Myristica fragrans Hoult leaves extract and their photodegradation activity of malachite green'. *IOP Conf. Ser. Mater. Sci. Eng.*, IOP Publishing Ltd, 1–6.

- Eskalen, H., Yaykaşlı, H., Kavgacı, M., and Kayış, A. (2022). 'Investigating the PVA/TiO₂/CDs polymer nanocomposites: effect of carbon dots for photocatalytic degradation of Rhodamine B'. *J. Mater. Sci. Mater. Electron.*, 33(7), 4643–4658.
- Esvandi, Z., Foroutan, R., Peighambaroust, S. J., Akbari, A., and Ramavandi, B. (2020). 'Uptake of anionic and cationic dyes from water using natural clay and clay/starch/MnFe₂O₄ magnetic nanocomposite'. *Surfaces and Interfaces*, 21, 100754.
- Faisal, S., Jan, H., Shah, S. A., Shah, S., Khan, A., Akbar, M. T., Rizwan, M., Jan, F., Wajidullah, Akhtar, N., Khattak, A., and Syed, S. (2021). 'Green Synthesis of Zinc Oxide (ZnO) Nanoparticles Using Aqueous Fruit Extracts of Myristica fragrans: Their Characterizations and Biological and Environmental Applications'. *ACS Omega*, 6(14), 9709–9722.
- Far, H., Hamici, M., Brihi, N., Haddadi, K., Boudissa, M., Chihi, T., and Fatmi, M. (2022). 'High-performance photocatalytic degradation of NiO nanoparticles embedded on α -Fe₂O₃ nanoporous layers under visible light irradiation'. *J. Mater. Res. Technol.*, 19, 1944–1960.
- Favaro, G., Confortin, D., Pastore, P., and Brustolon, M. (2012). 'Application of LC-MS and LC-MS-MS to the analysis of photo-decomposed crystal violet in the investigation of cultural heritage materials aging'. *J. Mass Spectrom.*, 47(12), 1660–1670.
- Fu, H., Huang, J., and Gray, K. (2021). 'Crumpled graphene balls adsorb micropollutants from water selectively and rapidly'. *Carbon N. Y.*, 183, 958–969.
- Gautam, R. K., Rawat, V., Banerjee, S., Sanroman, M. A., Soni, S., Singh, S. K., and Chattopadhyaya, M. C. (2015). 'Synthesis of bimetallic Fe-Zn nanoparticles and its application towards adsorptive removal of carcinogenic dye malachite green and Congo red in water'. *J. Mol. Liq.*, 212, 227–236.
- Ghaedi, M., Heidarpour, S., Nasiri, S., and Sahraie, R. (2012). 'Comparison of silver and palladium nanoparticles loaded on activated carbon for efficient removal of Methylene blue : Kinetic and isotherm study of removal process'. *Powder Technol.*, 228, 18–25.

- Ghorbani, M., Sheibani, S., Abdizadeh, H., and Golobostanfard, M. R. (2023). 'Modified BiFeO₃-rGO nanocomposite by controlled synthesis to enhance adsorption and visible-light photocatalytic activity'. *J. Mater. Res. Technol.*, 22, 1250–1267.
- Gokulan, R., Prabhu, G. G., and Jegan, J. (2019). 'Remediation of complex remazol effluent using biochar derived from green seaweed biomass'. *Int. J. Phytoremediation*, 21(12), 1179–1189.
- Gómez-Avilés, A., Peñas-Garzón, M., Bedia, J., Rodríguez, J. J., and Belver, C. (2019). 'C-modified TiO₂ using lignin as carbon precursor for the solar photocatalytic degradation of acetaminophen'. *Chem. Eng. J.*, 358, 1574–1582.
- Haider, A., and Kang, I. K. (2015). 'Preparation of silver nanoparticles and their industrial and biomedical applications: A comprehensive review'. *Adv. Mater. Sci. Eng.*, 2015, 165257.
- Hashemi, F., Rizi, H. B., Gheisari, K., Motamedi, H., Pereira, M., and Shirinbayan, M. (2020). 'Investigation of magnetic composites using as photocatalyst and antibacterial application'. *Inorg. Chem. Commun.*, 119, 108031.
- Hii, H. T. (2021). 'Adsorption Isotherm And Kinetic Models For Removal Of Methyl Orange And Remazol Brilliant Blue R By Coconut Shell Activated Carbon'. *Trop. Aquat. Soil Pollut.*, 1(1), 1–10.
- Hoerger, C. C., Schenzel, J., Strobel, B. W., and Bucheli, T. D. (2009). 'Analysis of selected phytotoxins and mycotoxins in environmental samples'. *Anal. Bioanal. Chem.*, 395(5), 1261–1289.
- Hoornweg, D., and Bhada-Tata, P. (2012). 'What a waste: A Global Review of Solid Waste Management'. *World Bank Urban Dev. Ser. Knowl. Pap.*, 1–116.
- HU, Y., Hamed, O., Salghi, R., Abidi, N., Jodeh, S., and Hattab, R. (2017). 'Extraction and characterization of cellulose from agricultural waste argan press cake'. *Cellul. Chem. Technol.*, 51, 263–272.
- Hussin, M. H. (2018). 'Extraction, modification and characterization of lignin from oil palm fronds as corrosion inhibitors for mild steel in acidic solution'. 1–226.

- Idris, R., Tawiequrrohman Yuliansyah, A., and Purwono, S. (2018). 'Development of Biobriquette from Nutmeg Seed Shells'. *E3S Web Conf.*, EDP Sciences, 1–4.
- Idris, Y. R., Bayu, H. T., Wintoko, J., Murachman, B., Yuliansyah, A. T., and Purwono, S. (2017). 'Kinetic Modelling of the Pyrolysis of Biomass for the Development of Charcoal Briquette'. *IOP Conf. Ser. Mater. Sci. Eng.*, 206(1), 1–7.
- Ikram, R., Mohamed Jan, B., Sidek, A., and Kenanakis, G. (2021). 'Utilization of eco-friendly waste generated nanomaterials in water-based drilling fluids; state of the art review'. *Materials (Basel)*, 14(15), 1–28.
- Isik, Z., Saleh, M., Bilici, Z., and Dizge, N. (2021). 'Remazol Brilliant Blue R (RBBR) dye and phosphate adsorption by calcium alginate beads modified with polyethyleneimine'. *Water Environ. Res.*, 93(11), 2780–2794.
- Islam, W. A. S. S. C. R. U. (2020). 'Photocatalytic degradation of rhodamine B under UV irradiation using Shorea robusta leaf extract - mediated bio - synthesized silver nanoparticles'. *Int. J. Environ. Sci. Technol.*, 17(4), 2059–2072.
- Izah, S. C., Zige, D. V, Alagoa, K. J., Uhunmwangho, E., and Iyamu, A. (2016). 'Antibacterial Efficacy of Aqueous Extract of Myristica fragrans (Common Nutmeg)'. *EC Pharmacol. Toxicol.*, 6, 241–250.
- Jabbar, Z. H., and Ebrahim, S. E. (2021). 'Synthesis, characterization, and photocatalytic degradation activity of core/shell magnetic nanocomposites (Fe₃O₄@SiO₂@Ag₂WO₄@Ag₂S) under visible light irradiation'. *Opt. Mater. (Amst)*, 122.
- Jana, R., Gupta, A., Choudhary, R., and Pandey, O. P. (2020). 'Influence of cationic doping at different sites in NaNbO₃ on the photocatalytic degradation of methylene blue dye'. *J. Sol-Gel Sci. Technol.*, 96(2), 405–415.
- Jawad, A. H., Abdulhameed, A. S., Kashi, E., Yaseen, Z. M., ALOthman, Z. A., and Khan, M. R. (2021). 'Cross-Linked Chitosan-Glyoxal/Kaolin Clay Composite: Parametric Optimization for Color Removal and COD Reduction of Remazol Brilliant Blue R Dye'. *J. Polym. Environ.*, 30, 164–178.

- Jelin, F. J., Kumar, S. S., Malini, M., M. Vanaja, and Annadurai, G. (2015). 'Environment-assisted green approach agnps by nutmeg (*Myristica fragrans*): Inhibition potential accustomed to pharmaceuticals'. *Eur. J. Biomed. Pharm. Sci.*, 2(3), 258–274.
- Jiang, M., Chen, L., and Niu, N. (2022). 'Enhanced adsorption for malachite green by functionalized lignin magnetic composites: Optimization, performance and adsorption mechanism'. *J. Mol. Struct.*, 1260, 132842.
- Jiang, Y. H., Li, A. Y., Deng, H., Ye, C. H., Wu, Y. Q., Linmu, Y. D., and Hang, H. L. (2019). 'Characteristics of nitrogen and phosphorus adsorption by Mg-loaded biochar from different feedstocks'. *Bioresour. Technol.*, 276, 183–189.
- Johari, M. A., and Khong, H. Y. (2019). 'Total Phenolic Content and Antioxidant and Antibacterial Activities of *Pereskia bleo*'. *Adv. Pharmacol. Sci.*, 2019, 1–4.
- John, S. (2019). 'Green Synthesis of Gold Nanoparticle using Nutmeg Fruit Extract'. *Int. J. Sci. Res.*, 8(5), 1704–1706.
- Joshi, K. M., Shinde, D. R., Nikam, L. K., Panmand, R., Sethi, Y. A., Kale, B. B., and Chaskar, M. G. (2019). 'Fragmented lignin-assisted synthesis of a hierarchical ZnO nanostructure for ammonia gas sensing'. *RSC Adv.*, 9(5), 2484–2492.
- Kabir Ahmad, R., Anwar Sulaiman, S., Yusup, S., Sham Dol, S., Inayat, M., and Aminu Umar, H. (2021). 'Exploring the potential of coconut shell biomass for charcoal production'. *Ain Shams Eng. J.*, 13(1), 101499.
- Khalil, M. M. H., Ismail, E. H., El-Baghdady, K. Z., and Mohamed, D. (2014). 'Green synthesis of silver nanoparticles using olive leaf extract and its antibacterial activity'. *Arab. J. Chem.*, 7(6), 1131–1139.
- Khan, I., Saeed, K., and Khan, I. (2017). 'Nanoparticles: Properties, applications and toxicities'. *Arab. J. Chem.*, 12(7), 908–931.
- Khandel, P., and Kumar, S. (2018). 'Mycogenic nanoparticles and their bio - prospective applications : current status and future challenges'. *J. Nanostructure Chem.*, 8(4), 369–391.

Kim, J., Nguyen, T. V. T., Kim, Y. H., Hollmann, F., and Park, C. B. (2022). 'Lignin as a multifunctional photocatalyst for solar-powered biocatalytic oxyfunctionalization of C–H bonds'. *Nat. Synth.*, 1(3), 217–226.

Kordy, M. G. M., Abdel-Gabbar, M., Soliman, H. A., Aljohani, G., Binsabt, M., Ahmed, I. A., and Shaban, M. (2022). 'Phyto-Capped Ag Nanoparticles: Green Synthesis, Characterization, and Catalytic and Antioxidant Activities'. *Nanomaterials*, 12(373), 1–20.

Krishnan, S., Jaiganesh, P. S., Karunakaran, A., Kumarasamy, K., and Lin, M. C. (2021). 'The effect of pH on the photocatalytic degradation of cationic and anionic dyes using polyazomethine/ZnO and polyazomethine/TiO₂ nanocomposites'. *Int. J. Appl. Sci. Eng.*, 18(5), 1–8.

Lai, H. J. (2021). 'Adsorption of Remazol Brilliant Violet 5R (RBV-5R) and Remazol Brilliant Blue R (RBBR) from Aqueous Solution by Using Agriculture Waste'. *Trop. Aquat. Soil Pollut.*, 1(1), 11–23.

Le, V. H., Huynh, L. T. N., Tran, T. N., Ho, T. T. N., Hoang, M. N., and Nguyen, T. H. (2021). 'Comparative desalination performance of activated carbon from coconut shell waste/carbon nanotubes composite in batch mode and single-pass mode'. *J. Appl. Electrochem.*, 51(9), 1313–1322.

Leal, C. C. A., Rocha, O. R. S. Da, Duarte, M. M. M. B., Dantas, R. F., Motta, M. Da, Filho, N. M. L. De, and Silva, V. L. Da. (2010). 'Evaluation of the adsorption process of Remazol Black B dye in liquid effluents by green coconut mesocarp'. *Afinidad*, 67(546), 136–142.

Lee, S. Y., Kang, D., Jeong, S., Do, H. T., and Kim, J. H. (2020). 'Photocatalytic Degradation of Rhodamine B Dye by TiO₂ and Gold Nanoparticles Supported on a Floating Porous Polydimethylsiloxane Sponge under Ultraviolet and Visible Light Irradiation'. *ACS Omega*, 5(8), 4233–4241.

Lewis, J., Miller, M., Crumb, J., Al-sayaghi, M., Buelke, C., Tesser, A., and Alshami, A. (2019). 'Biochar as a filler in mixed matrix materials : Synthesis , characterization , and applications'. *J. Appl. Polym. Sci.*, 136(41), 48027.

Li, J., Zhang, J., Natarajan, H., Zhang, J., and Ashok, B. (2019). 'Modification of agricultural waste tamarind fruit shell powder by in situ generation of silver nanoparticles for antibacterial filler applications'. *Int. J. Polym. Anal. Charact.*, 24(5), 421–427.

Li, T., Senesi, A. J., and Lee, B. (2016). 'Small Angle X-ray Scattering for Nanoparticle Research'. *Chem. Rev.*, 116(18), 11128–11180.

Lis, A., Aleš, H., Nad, R., Jablonsk, M., and Šurina, I. (2022). 'About Hydrophobicity of Lignin : A Review of Selected Chemical Methods for Lignin Valorisation in Biopolymer Production'. *Energies*, 15(17), 1–27.

Liu, Y., Jin, C., Yang, Z., Wu, G., Liu, G., and Kong, Z. (2021). 'Recent advances in lignin-based porous materials for pollutants removal from wastewater'. *Int. J. Biol. Macromol.*, 187, 880–891.

Losada-Barreiro, S., and Bravo-Díaz, C. (2017). 'Free radicals and polyphenols: The redox chemistry of neurodegenerative diseases'. *Eur. J. Med. Chem.*, 133, 379–402.

Luis López-Miranda, J., Borjas-Garcia, S. E., Esparza, R., and Rosas, G. (2016). 'Synthesis and Catalytic Evaluation of Silver Nanoparticles Synthesized with *Aloysia triphylla* Leaf Extract'. *J. Clust. Sci.*, 27(6), 1989–1999.

Ma, Y. zhi, Zheng, D. feng, Mo, Z. ye, Dong, R. jing, and Qiu, X. qing. (2018). 'Magnetic lignin-based carbon nanoparticles and the adsorption for removal of methyl orange'. *Colloids Surfaces A Physicochem. Eng. Asp.*, 559, 226–234.

Madhumithaa, S., Roy, A., Rajeshkumar, S., and Lakshmi, T. (2019). 'Preparation and characterization of nutmeg oleoresin-mediated silver nanoparticles'. *Drug Invent. Today*, 12(10), 2456–2458.

Malini, P. S. G., Premalatha, V., and Rani S. (2019). 'Green Synthesis and Characterization of Silver Nanoparticles using Ethanol Extract of *Myristica fragrans* (Nutmeg) and Its Biological Applications'. *J. Nanosci. Technol.*, 5(3), 738–740.

Mariana, M., Alfatah, T., Abdul Khalil, H. P. S., Yahya, E. B., Olaiya, N. G., Nuryawan, A., Mistar, E. M., Abdullah, C. K., Abdulmadjid, S. N., and Ismail, H.

(2021a). ‘A current advancement on the role of lignin as sustainable reinforcement material in biopolymeric blends’. *J. Mater. Res. Technol.*, 15, 2287–2316.

Mariana, M., Mistar, E. M., Alfatah, T., and Supardan, M. D. (2021b). ‘High-porous activated carbon derived from *Myristica fragrans* shell using one-step KOH activation for methylene blue adsorption’. *Bioresour. Technol. Reports*, 16, 100845.

Mary Ealias, A., and Saravanakumar, M. P. (2018). ‘Facile synthesis and characterisation of AlNs using Protein Rich Solution extracted from sewage sludge and its application for ultrasonic assisted dye adsorption: Isotherms, kinetics, mechanism and RSM design’. *J. Environ. Manage.*, 206, 215–227.

Mathiarasu, R. R., Manikandan, A., Panneerselvam, K., George, M., Raja, K. K., Almessiere, M. A., Slimani, Y., Baykal, A., Asiri, A. M., Kamal, T., and Khan, A. (2021). ‘Photocatalytic degradation of reactive anionic dyes RB5, RR198 and RY145 via rare earth element (REE) lanthanum substituted CaTiO₃ perovskite catalysts’. *J. Mater. Res. Technol.*, 15, 5936–5947.

Memon, G. Z. (2014). ‘Adsorption of Selected Pesticides from Aqueous Solutions Using Cost effective Walnut Shells’. *IOSR J. Eng.*, 4(10), 43–56.

Mendu, V., Shearin, T., Campbell, J. E., Stork, J., Jae, J., Crocker, M., Huber, G., and DeBolt, S. (2012). ‘Global bioenergy potential from high-lignin agricultural residue’. *Proc. Natl. Acad. Sci.*, 109(10), 4014–4019.

Mohami, R., Shakeri, A., and Nasrollahzadeh, M. (2022). ‘Mannich-mediated synthesis of a recyclable magnetic kraft lignin-coated copper nanostructure as an efficient catalyst for treatment of environmental contaminants in aqueous media’. *Sep. Purif. Technol.*, 285, 120373.

Mojtaba, S., Alireza, S., and Ramakrishna, S. (2019). ‘Green synthesis of supermagnetic Fe₃O₄ – MgO nanoparticles via Nutmeg essential oil toward superior anti-bacterial and anti-fungal performance’. *J. Drug Deliv. Sci. Technol.*, 54, 101352.

Morosanu, I., Teodosiu, C., Coroaba, A., and Paduraru, C. (2019). ‘Sequencing batch biosorption of micropollutants from aqueous effluents by rapeseed waste: Experimental assessment and statistical modelling’. *J. Environ. Manage.*, 230, 110–

118.

Mosaviniya, M., Kikhavani, T., Tanzifi, M., Tavakkoli Yaraki, M., Tajbakhsh, P., and Lajevardi, A. (2019). 'Facile green synthesis of silver nanoparticles using *Crocus Haussknechtii* Bois bulb extract: Catalytic activity and antibacterial properties'. *Colloids Interface Sci. Commun.*, 33, 100211.

Motelica, L., Ficai, D., Ficai, A., Oprea, O. C., Kaya, D. A., and Andronesu, E. (2020). 'Biodegradable antimicrobial food packaging: Trends and perspectives'. *Foods*, 9(10), 1–36.

Mukunthan, K. S., and Balaji, S. (2012). 'Cashew apple juice (*Anacardium occidentale* L.) speeds up the synthesis of silver nanoparticles'. *Int. J. Green Nanotechnol. Biomed.*, 4(2), 71–79.

Muraro, P. C. L., Mortari, S. R., Vizzotto, B. S., Chuy, G., Santos, C. dos, Brum, L. F. W., and Silva, W. L. da. (2020). 'Iron oxide nanocatalyst with titanium and silver nanoparticles: Synthesis, characterization and photocatalytic activity on the degradation of Rhodamine B dye'. *Sci. Rep.*, 10(1), 1–9.

Mustikasari, K., Komari, N., Santoso, M., and Ersam, T. (2015). 'Synthesis of Myristicyl Ethanoate from Myristicin Aldehyde Kamilia'. *Int. Conf. Nat. Math. Environ. Sci.*, 157–160.

Niazi, N. K., Murtaza, B., Bibi, I., Shahid, M., White, J. C., Nawaz, M. F., Bashir, S., Shakoor, M. B., Choppala, G., Murtaza, G., and Wang, H. (2016). 'Removal and Recovery of Metals by Biosorbents and Biochars Derived From Biowastes'. *Environ. Mater. Waste*, 149–177.

Obi, F. O., Ugwuishiwu, B. O., and Nwakaire, J. N. (2016). 'Agricultural waste concept , generation , utilization and management'. *Niger. J. Technol.*, 35, 957–964.

Olajuyigbe, F. M., Fatokun, C. O., and Oyelere, O. M. (2018). 'Biodelignification of some agro-residues by *Stenotrophomonas* sp. CFB-09 and enhanced production of ligninolytic enzymes'. *Biocatal. Agric. Biotechnol.*, 15, 120–130.

P. González-García. (2018). 'Activated carbon from lignocellulosics precursors : A

review of the synthesis methods , characterization techniques and applications’.

Renew. Sustain. Energy Rev., 82, 1393–1414.

Pauline, M. C., Sangeetha, R., Manikandan, M., Loganathan¹, P., and Kalaiarasi, J. M. V. (2019). ‘Myristica fragrans (Nutmeg) oil mediated silver nanoparticle synthesis , characterisation and its antimicrobial assessment’. *Uttar Pradesh J. Zool.*, 40(2), 54–59.

Podasca, V. E., Buruiana, T., and Buruiana, E. C. (2019). ‘Photocatalytic degradation of Rhodamine B dye by polymeric films containing ZnO, Ag nanoparticles and polypyrrole’. *J. Photochem. Photobiol. A Chem.*, 371, 188–195.

Pranati, T., Anitha, R., Rajeshkumar, S., and Lakshmi, T. (2019). ‘Preparation of Silver nanoparticles using Nutmeg oleoresin and its Antimicrobial activity against Oral pathogens’. *Res. J. Pharm. Technol.*, 12(6).

Punypwar, S., and Mutnuri, S. (2022). ‘Laundry greywater treatment by anaerobic filters and vertical flow constructed wetlands’. *Water Environ. J.*, (May 2021), 1–9.

Pype, R., Flahaut, S., and Debaste, F. (2019). ‘On the importance of mechanisms analysis in the degradation of micropollutants by laccases: The case of Remazol Brilliant Blue R’. *Environ. Technol. Innov.*, 14, 100324.

Quesada, H. B., Baptista, A. T. A., Cusioli, L. F., Seibert, D., Oliveira Bezerra, C. de, and Bergamasco, R. (2019). ‘Surface water pollution by pharmaceuticals and an alternative of removal by low-cost adsorbents: A review’. *Chemosphere*, 222, 766–780.

Ragan, S., Megonnell, N., Court, C., Leigh, M. E., Ragan, S., and Megonnell, N. (2011). ‘Activated carbon from renewable resources- lignin’. *Cellul. Chem. Technol.*, 45(7–8), 527–531.

Rahman, A. U., Ullah, A., Yuan, Q., Wei, Y., and Ahmad, A. (2019). ‘Tuber extract of *Arisaema flavum* eco-benignly and effectively synthesizes silver nanoparticles : Photocatalytic and antibacterial response against multidrug resistant engineered *E. coli* QH4’. *J. Photochem. Photobiol. B Biol.*, 193, 31–38.

Rahmat, M., Rehman, A., Rahmat, S., Bhatti, H. N., Iqbal, M., Khan, W. S., Bajwa, S. Z., Rahmat, R., and Nazir, A. (2019). 'Highly efficient removal of crystal violet dye from water by MnO₂ based nanofibrous mesh/photocatalytic process'. *J. Mater. Res. Technol.*, 8(6), 5149–5159.

Rahmat, N. A., Ali, A. A., Salmiati, Hussain, N., Muhamad, M. S., Kristanti, R. A., and Hadibarata, T. (2016). 'Removal of Remazol Brilliant Blue R from Aqueous Solution by Adsorption Using Pineapple Leaf Powder and Lime Peel Powder'. *Water. Air. Soil Pollut.*, 227(4), 1–11.

Rainert, K. T., Nunes, H. C. A., Gonçalves, M. J., Helm, C. V., and Tavares, L. B. B. (2021). 'Decolorization of the synthetic dye Remazol Brilliant Blue Reactive (RBBR) by *Ganoderma lucidum* on bio-Adsorbent of the solid bleached sulfate paperboard coated with polyethylene terephthalate'. *J. Environ. Chem. Eng.*, 9(2), 104990.

Raj, A., Yadav, A., Rawat, A. P., Singh, A. K., Kumar, S., Pandey, A. K., Sirohi, R., and Pandey, A. (2021). 'Kinetic and thermodynamic investigations of sewage sludge biochar in removal of Remazol Brilliant Blue R dye from aqueous solution and evaluation of residual dyes cytotoxicity'. *Environ. Technol. Innov.*, 23, 101556.

Ramasamy, K., Dhavamani, S., Natesan, G., Sengodan, K., Sengottayan, S. N., Tiwari, M., Shivendra Vikram, S., and Perumal, V. (2021). 'A potential role of green engineered TiO₂ nanocatalyst towards enhanced photocatalytic and biomedical applications'. *Environ. Sci. Pollut. Res.*, 28(30), 41207–41223.

Ramya P. (2022). 'Anti-Diabetic Activity of Silver Nanoparticles Synthesized From The Hydroethanolic Extract of *Myristica Fragrans* Seeds'. *Appl. Biochem. Biotechnol.*, 194(3), 1136–1148.

Rao, S. S., Saptami, K., Venkatesan, J., and Rekha, P. D. (2020). 'Microwave-assisted rapid synthesis of silver nanoparticles using fucoidan: Characterization with assessment of biocompatibility and antimicrobial activity'. *Int. J. Biol. Macromol.*, 163, 745–755.

Reghioua, A., Barkat, D., Jawad, A. H., Abdulhameed, A. S., Al-Kahtani, A. A., and Alothman, Z. A. (2021a). 'Parametric optimization by Box-Behnken design for

synthesis of magnetic chitosan-benzil/ZnO/Fe₃O₄nanocomposite and textile dye removal'. *J. Environ. Chem. Eng.*, 9(3), 105166.

Reghioua, A., Barkat, D., Jawad, A. H., Abdulhameed, A. S., Rangabhashiyam, S., Khan, M. R., and ALothman, Z. A. (2021b). 'Magnetic Chitosan-Glutaraldehyde/Zinc Oxide/Fe₃O₄ Nanocomposite: Optimization and Adsorptive Mechanism of Remazol Brilliant Blue R Dye Removal'. *J. Polym. Environ.*, 29, 3932–3947.

Rema, J., and Krishnamoorthy, B. (2012). 'Nutmeg and mace'. *Handb. Herbs Spices Second Ed.*, Elsevier Inc., 399–416.

Rinaldi, R., Jastrzebski, R., Clough, M. T., Ralph, J., Kennema, M., Bruijninx, P. C. A., and Weckhuysen, B. M. (2016). 'Paving the Way for Lignin Valorisation: Recent Advances in Bioengineering, Biorefining and Catalysis'. *Angew. Chemie - Int. Ed.*, 55(29), 8164–8215.

Rizwan, M., Amin, S., Kudaibergenova, B. M., Rauf, A., Siddique, M., Ullah, K., Bawazeer, S., Farooq, U., Mabkhot, Y. N., and Ramadan, M. F. (2020). 'Green synthesis and antimicrobial potential of silver Nanoparticles with Boerhavia procumbens extract'. *J. Pure Appl. Microbiol.*, 14(2), 1437–1451.

Rohini, B. R., and Ramachandran, R. (2020). 'Synthesis, Characterization and Study on the Biocompatibility of Myristica fragrans (Nutmeg) Incorporated Hydroxyapatite Dental Biocomposite'. *Trends Biosci.*, 11(16), 2620–2623.

Rout, T., Pradhan, D., Singh, R. K., and Kumari, N. (2016). 'Exhaustive study of products obtained from coconut shell pyrolysis'. *J. Environ. Chem. Eng.*, 4(3), 3696–3705.

Roy, S. D., Das, K. C., and Dhar, S. S. (2021). 'Conventional to green synthesis of magnetic iron oxide nanoparticles; its application as catalyst, photocatalyst and toxicity: A short review'. *Inorg. Chem. Commun.*, 134, 109050.

Sagadevan, S., Anita Lett, J., Vennila, S., Varun Prasath, P., Saravanan Kaliaraj, G., Fatimah, I., Léonard, E., Mohammad, F., Al-Lohedan, H. A., Alshahateet, S. F., and Lee, C. T. (2021). 'Photocatalytic activity and antibacterial efficacy of titanium

dioxide nanoparticles mediated by *Myristica fragrans* seed extract'. *Chem. Phys. Lett.*, 771, 138527.

Saha, P. (2010). 'Assessment on the removal of methylene blue dye using tamarind fruit shell as biosorbent'. *Water. Air. Soil Pollut.*, 213(1–4), 287–299.

Salah, M., and El-Haggag, P. (2007). 'Sustainability of Agricultural and Rural Waste Management'. *Sustain. Ind. Des. Waste Manag.*, 223–260.

Salindeho, N., Purnomo, H., and Kekenusa, J. (2014). 'Physicochemical Characteristics and Fatty Acid Profile of Smoked Skipjack Tuna (*Katsuwonus pelamis*) Using Coconut Fiber , Nutmeg Shell and Their Combination as Smoke Sources'. 6(7), 3841–3846.

Salomatina, E. V, Fukina, D. G., Koryagin, A. V, Titaev, D. N., Suleimanov, E. V, and Smirnova, A. (2021). 'Preparation and photocatalytic properties of titanium dioxide modified with gold or silver nanoparticles'. *J. Environ. Chem. Eng.*, 9(5), 106078.

Saratale, R. G., Cho, S. K., Saratale, G. D., Kadam, A. A., Ghodake, G. S., Magotra, V. K., Kumar, M., Bharagava, R. N., Varjani, S., Palem, R. R., Mulla, S. I., Kim, D. S., and Shin, H. S. (2022). 'Lignin-Mediated Silver Nanoparticle Synthesis for Photocatalytic Degradation of Reactive Yellow 4G and In Vitro Assessment of Antioxidant, Antidiabetic, and Antibacterial Activities'. *Polymers (Basel)*, 14(3), 1–18.

Saravanakumar, A., Ganesh, M., Peng, M. M., Aziz, A. S., and Jang, H. T. (2015). 'Comparative antioxidant and antimycobacterial activities of *Opuntia ficus-indica* fruit extracts from summer and rainy seasons'. *Front. Life Sci.*, 8(2), 182–191.

Sasidharan, D., Namitha, T. R., Johnson, S. P., Jose, V., and Mathew, P. (2020). 'Synthesis of silver and copper oxide nanoparticles using *Myristica fragrans* fruit extract: Antimicrobial and catalytic applications'. *Sustain. Chem. Pharm.*, 16, 100255.

Sathishkumar, P., Arulkumar, M., and Palvannan, T. (2012). 'Utilization of agro-industrial waste *Jatropha curcas* pods as an activated carbon for the adsorption of reactive dye Remazol Brilliant Blue R (RBBR)'. *J. Clean. Prod.*, 22(1), 67–75.

- Saxena, R. (2012). 'Phytochemical Studies on Myristica fragrance Essential Oil'. *Biol. Forum – An Int. J.*, 4(2), 22–64.
- Seerangaraj, V., Sathiyavimal, S., Shankar, S. N., Nandagopal, J. G. T., Balashanmugam, P., Al-Misned, F. A., Shanmugavel, M., Senthilkumar, P., and Pugazhendhi, A. (2021). 'Cytotoxic effects of silver nanoparticles on *Ruellia tuberosa*: Photocatalytic degradation properties against crystal violet and coomassie brilliant blue'. *J. Environ. Chem. Eng.*, 9(2), 105088.
- Shafey, A. M. El. (2020). 'Green synthesis of metal and metal oxide nanoparticles from plant leaf extracts and their applications: A review'. *Green Process. Synth.*, 9(1), 304–339.
- Shagholani, H., Ghoreishi, S. M., and Mousazadeh, M. (2015). 'Improvement of interaction between PVA and chitosan via magnetite nanoparticles for drug delivery application'. *Int. J. Biol. Macromol.*, 78, 130–136.
- Shahi, A. (2014). 'Kraft lignin: a novel alternative to oil spill cleanup recycling industrial waste'. *Can. Young Sci. J.*, 2014(3), 42–46.
- Shaikh, W. A., Chakraborty, S., and Islam, R. U. (2020). 'Photocatalytic degradation of rhodamine B under UV irradiation using *Shorea robusta* leaf extract-mediated bio-synthesized silver nanoparticles'. *Int. J. Environ. Sci. Technol.*, 17(4), 2059–2072.
- Shankar, S., and Rhim, J. W. (2017). 'Preparation and characterization of agar/lignin/silver nanoparticles composite films with ultraviolet light barrier and antibacterial properties'. *Food Hydrocoll.*, 71, 76–84.
- Sharma, G., Sharma, A. R., Kurian, M., Bhavesh, R., Nam, J. S., and Lee, S. S. (2014). 'Green synthesis of silver nanoparticle using *Myristica Fragrans* (Nutmeg) seed extract and its biological activity.' *Nanomater. Biostructures*, 9(1), 325–332.
- Sharma, J., Sharma, S., and Soni, V. (2021). 'Classification and impact of synthetic textile dyes on Aquatic Flora: A review'. *Reg. Stud. Mar. Sci.*, 45, 101802.
- Shigwenya, E., Patrick, M., Kareru, G., Gachui, E., Augustine, M., Nyabola, O., Indire, S., Jared, W., and Nyang, O. (2019). 'Biosynthesis of iron nanoparticles using

Ageratum conyzoides extracts , their antimicrobial and photocatalytic activity'. *SN Appl. Sci.*, 500 (2019).

Sidorowicz, A., Szymański, T., and Rybka, J. D. (2021). 'Photodegradation of biohazardous dye brilliant blue r using organometallic silver nanoparticles synthesized through a green chemistry method'. *Biology (Basel)*., 10(8), 1–16.

Silva, T. L., Ronix, A., Pezoti, O., Souza, L. S., Leandro, P. K. T., Bedin, K. C., Beltrame, K. K., Cazetta, A. L., and Almeida, V. C. (2016). 'Mesoporous activated carbon from industrial laundry sewage sludge: Adsorption studies of reactive dye Remazol Brilliant Blue R'. *Chem. Eng. J.*, 303, 467–476.

Singh, J., and Dhaliwal, A. S. (2020). 'Plasmon-induced photocatalytic degradation of methylene blue dye using biosynthesized silver nanoparticles as photocatalyst'. *Environ. Technol. (United Kingdom)*, 41(12), 1520–1534.

Singh, R. H., Sankat, C. K., and Mujaffar, S. (2015). 'The nutmeg and spice industry in Grenada: Innovations and competitiveness Acase study'. 1–35.

Slavov, L., Abrashev, M. V., Merodiiska, T., Gelev, C., Vandenberghe, R. E., Markova-Deneva, I., and Nedkov, I. (2010). 'Raman spectroscopy investigation of magnetite nanoparticles in ferrofluids'. *J. Magn. Magn. Mater.*, 322(14), 1904–1911.

Soleimani, M., and Kaghazchi, T. (2007). 'Agricultural waste conversion to activated carbon by chemical activation with phosphoric acid'. *Chem. Eng. Technol.*, 30(5), 649–654.

Srisasiwimon, N., Chuangchote, S., Laosiripojana, N., and Sagawa, T. (2018). 'TiO₂ / Lignin-based Carbon Compositated Photocatalysts for Enhanced Photocatalytic Conversion of Lignin to High Value Chemicals'. *ACS Sustain. Chem. Eng.*, 6(11), 13968–13976.

Stagos, D. (2020). 'Antioxidant activity of polyphenolic plant extracts'. *Antioxidants*, 9(1), 1–7.

Stamm, C., Räsänen, K., Burdon, F. J., Altermatt, F., Jokela, J., Joss, A., Ackermann, M., and Eggen, R. I. L. (2016). 'Unravelling the Impacts of Micropollutants in

Aquatic Ecosystems: Interdisciplinary Studies at the Interface of Large-Scale Ecology'. *Adv. Ecol. Res.*, 55, 183–223.

Stratil, P., Klejdus, B., and Kubáň, V. (2006). 'Determination of total content of phenolic compounds and their antioxidant activity in vegetables - Evaluation of spectrophotometric methods'. *J. Agric. Food Chem.*, 54(3), 607–616.

Suguna, Y. (2013). 'Sunlight induced removal of Rhodamine B from water through Semiconductor Photocatalysis: Effects of Adsorption, Reaction Conditions and Additives'. *Res. J. Mater. Sci.*, 1(4), 9–17.

Sulaiman, S. F., and Ooi, K. L. (2012a). 'Antioxidant and anti food-borne bacterial activities of extracts from leaf and different fruit parts of *Myristica fragrans* Houtt'. *Food Control*, 25(2), 533–536.

Sulaiman, S. F., and Ooi, K. L. (2012b). 'Antioxidant and anti food-borne bacterial activities of extracts from leaf and different fruit parts of *Myristica fragrans* Houtt'. *Food Control*, 25(2), 533–536.

Suprihatin, I. E., Lestari, G. A. D., Mardhani, R., and Edoway, V. (2020). 'Silver nanoparticles (AgNPs) as photocatalyst in the photodegradation of rhemazol brilliant blue'. *IOP Conf. Ser. Mater. Sci. Eng.*, 959(1), 11–17.

Suryaningsih, S., Nurhilal, O., Mohanty, M. K., and Mishra, S. (2017). 'Kinetic Modelling of the Pyrolysis of Biomass for the Development of Charcoal Briquette Kinetic Modelling of the Pyrolysis of Biomass for the Development of Charcoal Briquette'. *IOP Conf. Ser. Mater. Sci. Eng.*, 206, 012063.

Suteu, D., Malutan, T., and Bilba, D. (2010). 'Removal of reactive dye Brilliant Red HE-3B from aqueous solutions by industrial lignin: Equilibrium and kinetics modeling'. *Desalination*, 255(1–3), 84–90.

Suzuki, K., Saito, Y., Okazaki, N., and Suzuki, T. (2020). 'Graphite-shell-chains selectively and efficiently produced from biomass rich in cellulose and chitin'. *Sci. Rep.*, 10(1), 1–7.

Syahiddin, D. S., and Muslim, A. (2018). 'Adsorption of Cu (II) Ions onto *Myristica*

- Fragrans Shell-based Activated Carbon : Isotherm , Kinetic and Thermodynamic Studies'. *J. Korean Chem. Soc.*, 62(2), 79–86.
- Tepe, O. (2018). 'Catalytic Removal of Remazol Brilliant Blue R by Manganese Oxide Octahedral Molecular Sieves and Persulfate'. *J. Environ. Eng.*, 144(9), 1–11.
- Thakur, S., Govender, P. P., Mamo, M. A., Tamulevicius, S., Kumar, Y., and Kumar, V. (2017). 'Progress in lignin hydrogels and nanocomposites for water purification : Future perspectives'. *Vaccum*, 146, 342–355.
- Thamaraiselvan, C., Thakur, A. K., Gupta, A., and Arnusch, C. J. (2021). 'Electrochemical Removal of Organic and Inorganic Pollutants Using Robust Laser-Induced Graphene Membranes'. *ACS Appl. Mater. Interfaces*, 13(1), 1452–1462.
- Thomas, T., and Thalla, A. K. (2022). 'Nutmeg seed shell biochar as an effective adsorbent for removal of remazol brilliant blue reactive dye: kinetic, isotherm, and thermodynamic study'. *Energy Sources, Part A Recover. Util. Environ. Eff.*, 44(1), 893–911.
- Thommes, M., Kaneko, K., Neimark, A. V, Olivier, J. P., Rodriguez-reinoso, F., Rouquerol, J., and Sing, K. S. W. (2015). 'Physisorption of gases , with special reference to the evaluation of surface area and pore size distribution (IUPAC Technical Report)'. *Pure Appl. Chem.*, 87, 1051–1069.
- Thummaneni, C., Surya Prakash, D. V., Golli, R., and Vangalapati, M. (2022). 'Green synthesis of silver nanoparticles and characterization of caffeic acid from Myristica fragrans (Nutmeg) against antibacterial activity'. *Mater. Today Proc.*, 62, 4001–4005.
- Tkaczyk, A., Mitrowska, K., and Posyniak, A. (2020). 'Synthetic organic dyes as contaminants of the aquatic environment and their implications for ecosystems: A review'. *Sci. Total Environ.*, 717, 137222.
- Tu, W., Liu, Y., Chen, M., Zhou, Y., Xie, Z., Ma, L., Li, L., and Yang, B. (2022). 'Carbon nitride coupled with Ti₃C₂-Mxene derived amorphous Ti-peroxo heterojunction for photocatalytic degradation of rhodamine B and tetracycline'. *Colloids Surfaces A Physicochem. Eng. Asp.*, 640, 128448.

- Ulum, B., Ilyas, S., Fahri, A. N., Mutmainna, I., Anugrah, M. A., Yudasari, N., Demmalino, E. B., and Tahir, D. (2020). 'Composite Carbon-lignin/ Zinc Oxide Nanocrystalline Ball-like Hexagonal Mediated from *Jatropha curcas* L Leaf as Photocatalyst for Industrial Dye Degradation'. *J. Inorg. Organomet. Polym. Mater.*, 30(12), 4905–4916.
- Uma, S., Thalla, A. K., and Devatha, C. P. (2020). 'Co-digestion of Food Waste and Switchgrass for Biogas Potential : Effects of Process Parameters'. *Waste and Biomass Valorization*, 11(3), 827–839.
- Umar, K., Haque, M. M., Muneer, M., Harada, T., and Matsumura, M. (2013). 'Mo, Mn and la doped TiO₂: Synthesis, characterization and photocatalytic activity for the decolourization of three different chromophoric dyes'. *J. Alloys Compd.*, 578, 431–438.
- Vannarath, A., and Thalla, A. K. (2021). 'Synthesis and characterisation of an ultra-light , hydrophobic and flame-retardant robust lignin-carbon foam for oil-water separation'. *J. Clean. Prod.*, 325, 129263.
- Velsankar, K., Aswin Kumara, R. M., Preethi, R., Muthulakshmi, V., and Sudhahar, S. (2020a). 'Green synthesis of CuO nanoparticles via *Allium sativum* extract and its characterizations on antimicrobial, antioxidant, antilarvicidal activities'. *J. Environ. Chem. Eng.*, 8(5), 104123.
- Velsankar, K., Preethi, R., Ram, P. S. J., Ramesh, M., and Sudhahar, S. (2020b). 'Evaluations of biosynthesized Ag nanoparticles via *Allium Sativum* flower extract in biological applications'. *Appl. Nanosci.*, 10(9), 3675–3691.
- Vijayakumar, G., Kesavan, H., Kannan, A., Arulanandam, D., Kim, J. H., Kim, K. J., Song, H. J., Kim, H. J., and Rangarajulu, S. K. (2021). 'Phytosynthesis of copper nanoparticles using extracts of spices and their antibacterial properties'. *Processes*, 9(8), 1341.
- Vilas, V., Philip, D., and Mathew, J. (2014). 'Phytochemical-capped biogenic gold nanocrystals with chemocatalytic and radical scavenging potential'. *J. Mol. Liq.*, 200, 390–397.

- Waheeb, A. S., Alshamsi, H. A. H., Al-Hussainawy, M. K., and Saud, H. R. (2020). 'Myristica fragrans shells as potential low cost bio-adsorbent for the efficient removal of rose bengal from aqueous solution: Characteristic and kinetic study'. *Indones. J. Chem.*, 20(5), 1152–1162.
- Wang, J., Ma, X., Fang, G., Pan, M., Ye, X., and Wang, S. (2011). 'Preparation of iminodiacetic acid functionalized multi-walled carbon nanotubes and its application as sorbent for separation and preconcentration of heavy metal ions'. *J. Hazard. Mater.*, 186(2–3), 1985–1992.
- Wang, S., Zheng, Y., Yan, W., Chen, L., Dummi Mahadevan, G., and Zhao, F. (2016). 'Enhanced bioleaching efficiency of metals from E-wastes driven by biochar'. *J. Hazard. Mater.*, 320, 393–400.
- Wang, T., Liu, X., Ting Xu, Wei, M., Ma, C., Huo, P., and Yan, Y. (2020). 'Lignin-controlled photocatalyst of porous BiVO₄-C nanocomposite for enhancing photocatalytic activity toward pollutant under visible-light'. *Appl. Surf. Sci.*, 523, 146401.
- Widjanarko, S. B., Kusnadi, J., and Berhimpon, S. (2014). 'Antioxidant potential of flesh , seed and mace of nutmeg (Myristica fragrans Antioxidant Potential of Flesh , Seed and Mace of Nutmeg (Myristica fragrans Hoult)'. *Int. J. ChemTech Res.*, 6(4), 2460–2468.
- Xiang, Z., Han, W., Zhu, W., Zhang, Y., and Deng, J. (2020). 'Photocatalytic conversion of lignin to chemicals and fuels'. *ChemSusChem*, 13(17), 419–4213.
- Yazdani, M. R. (2018). 'Engineered adsorptive materials for water remediation-Development, characterization, and application'. 1–69.
- Yonten, V., Tanyol, M., Yildirim, N., Yildirim, N. C., and Ince, M. (2016). 'Optimization of Remazol Brilliant Blue R dye removal by novel biosorbent *P. eryngii* immobilized on Amberlite XAD-4 using response surface methodology'. *Desalin. Water Treat.*, 57(33), 15592–15602.
- You-Ji, L., and Wei, C. (2011). 'Photocatalytic degradation of Rhodamine B using nanocrystalline TiO₂-zeolite surface composite catalysts: Effects of photocatalytic

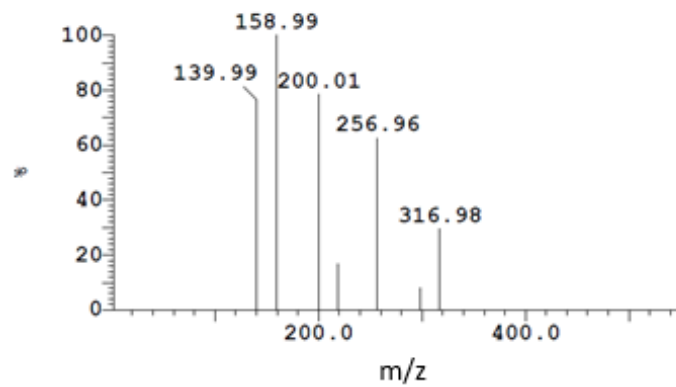
- condition on degradation efficiency'. *Catal. Sci. Technol.*, 1(5), 802–809.
- Yuan, X., Dissanayake, P. D., Gao, B., Liu, W. J., Lee, K. B., and Ok, Y. S. (2021). 'Review on upgrading organic waste to value-added carbon materials for energy and environmental applications'. *J. Environ. Manage.*, 296, 113128.
- Zahoor, M., and Ali Khan, F. (2018). 'Adsorption of aflatoxin B1 on magnetic carbon nanocomposites prepared from bagasse'. *Arab. J. Chem.*, 11(5), 729–738.
- Zhang, L., and Jaroniec, M. (2020). 'Fundamentals of adsorption for photocatalysis'. *Interface Sci. Technol.*, 31, 39–62.
- Zhang, L., Wan, L., Chang, N., Liu, J., Duan, C., Zhou, Q., Li, X., and Wang, X. (2011). 'Removal of phosphate from water by activated carbon fiber loaded with lanthanum oxide'. *J. Hazard. Mater.*, 190(1–3), 848–855.
- Zhang, Y., Yu, F., Cheng, W., Wang, J., and Ma, J. (2017). 'Adsorption Equilibrium and Kinetics of the Removal of Ammoniacal Nitrogen by Zeolite X / Activated Carbon Composite Synthesized from Elutrilithe'. *Hindawi J. Chem.*, 2017, 1–9.
- Zhao, H., Cheng, Y., Zhang, Z., Zhang, B., Pei, C., Fan, F., and Ji, G. (2021). 'Biomass-derived graphene-like porous carbon nanosheets towards ultralight microwave absorption and excellent thermal infrared properties'. *Carbon N. Y.*, 173, 501–511.
- Zhao, X., Su, S., Wu, G., Li, C., Qin, Z., Lou, X., and Zhou, J. (2017). 'Facile synthesis of the flower-like ternary heterostructure of Ag/ZnO encapsulating carbon spheres with enhanced photocatalytic performance'. *Appl. Surf. Sci.*, 406, 254–264.
- Zulfiqar, M., Chowdhury, S., Samsudin, M. F. R., Siyal, A. A., Omar, A. A., Ahmad, T., and Sufian, S. (2020). 'Effect of organic solvents on the growth of TiO₂ nanotubes: An insight into photocatalytic degradation and adsorption studies'. *J. Water Process Eng.*, 37, 101491.

APPENDICES

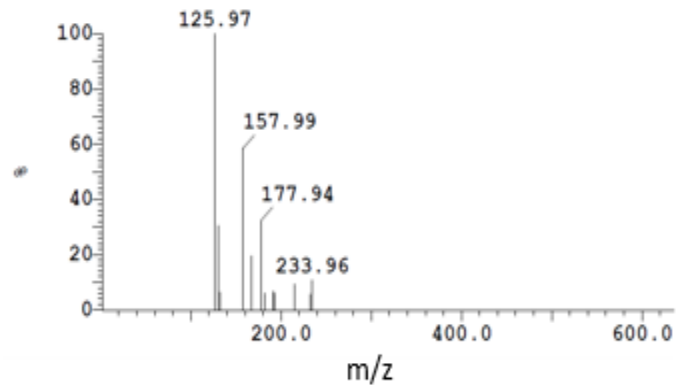
APPENDIX A

LCMS chromatogram for degradation for dyes using silver NPs

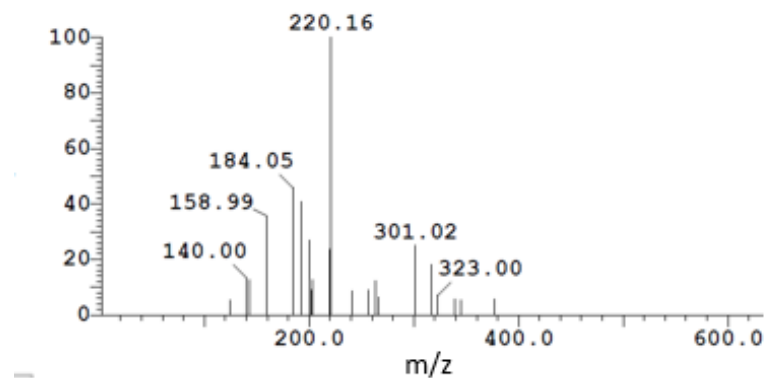
a) MV dye degradation



b) RBBR dye degradation



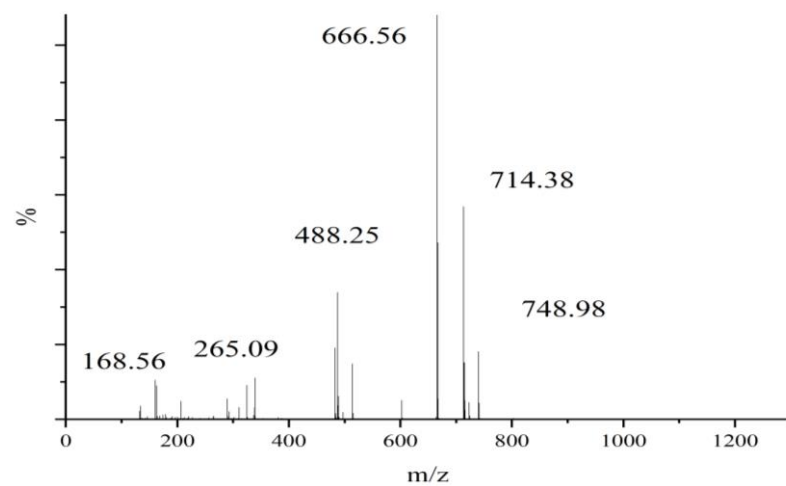
c) RhB dye degradation



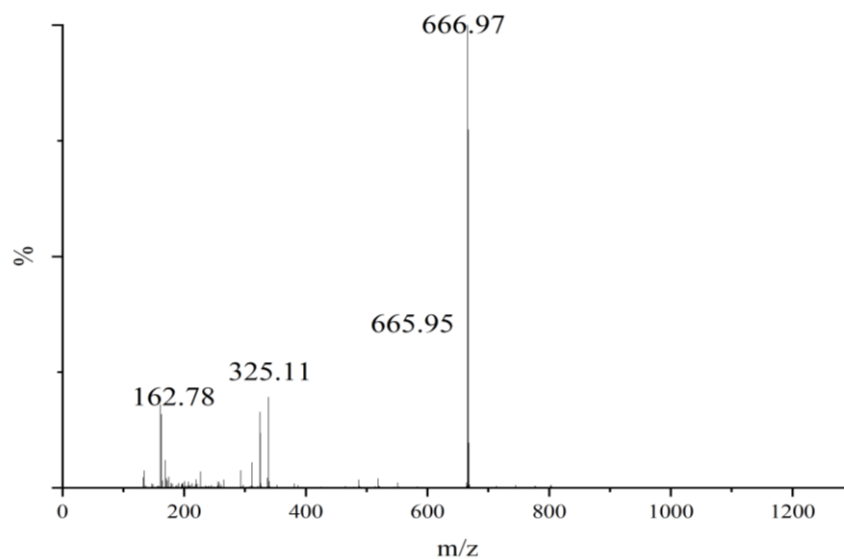
APPENDIX B

LCMS chromatogram for degradation for mixture of dyes using Ag/Fe/Lignin at different reaction times:

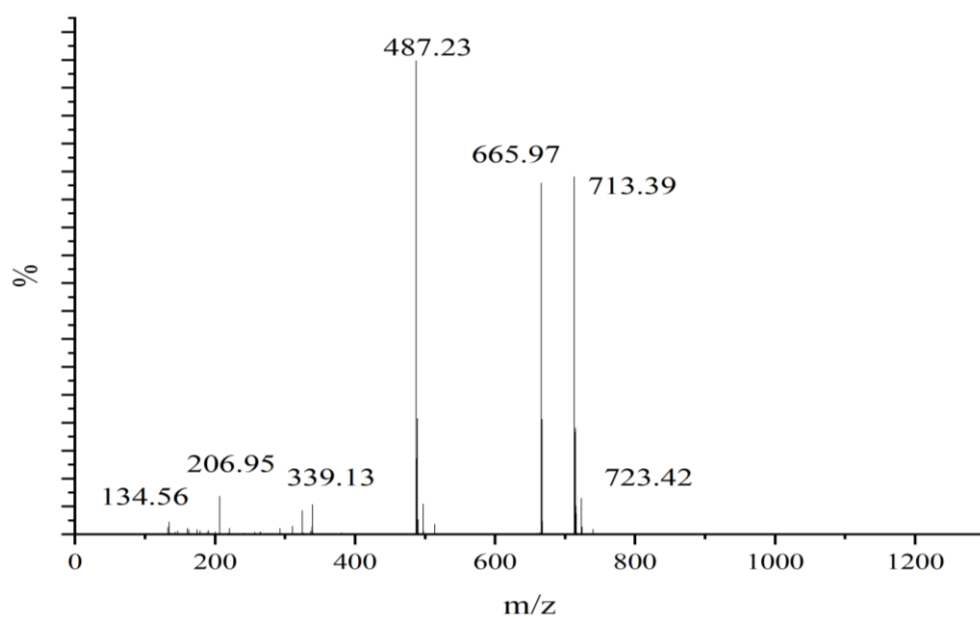
a) Initial



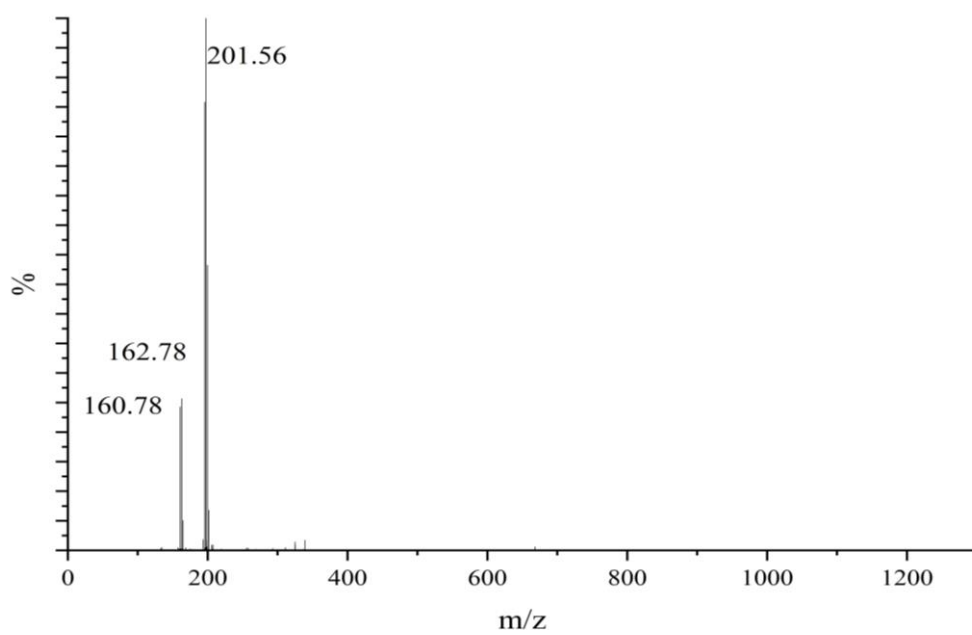
b) 30 min



c) 60 min



d) 90 min



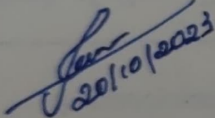
NATIONAL INSTITUTE OF TECHNOLOGY KARNATAKA, SURATHKAL

List of Publications based on PhD Research Work

S. No.	Title of the paper	Authors (in the same order as in the paper. Underline the Research Scholar's name)	Name of the Journal/ Conference/ Symposium, Vol., No., Pages	Month & Year of Publication	Category *
1	Nutmeg seed shell biochar as an effective adsorbent for removal of remazol brilliant blue reactive dye: kinetic, isotherm, and thermodynamic study	<u>Teema Thomas</u> , Arun Kumar Thalla	Energy Sources, Part A: Recovery, Utilisation, and Environmental Effects (Taylor & Francis), IF: 2.9, Volume 44, Issue 1, DOI: 10.1080/15567036.2022.2050850	February 2022	1
2	Synthesis of silver NPs using <i>Myristica fragrans</i> seed shell: Assessment of antibacterial, antioxidant properties and photocatalytic degradation of dyes	<u>Teema Thomas</u> , Arun Kumar Thalla	Journal of Environmental Chemical Engineering (Elsevier) IF: 7.968, Volume 11, Issue 2, 109585, DOI: DOI: 10.1016/j.jece.2023.109585	April 2023	1
3	Nutmeg seed shell-based silver NP/PVA composite for the synthesis of antimicrobial food packaging films	<u>Teema Thomas</u> , Arun Kumar Thalla	International Conference on Sustainable Chemical and Environmental Engineering, Rethymno, Crete, Greece	31 Aug – 04 Sep 2022	3

4	Green synthesis of silver nanoparticles using nutmeg seed shell extract	<u>Teema Thomas</u> , Arun Kumar Thalla	BREEECH 2021, CSIR, Dehradun, India	1-4 Dec 2021	3
5	Antimicrobial and antioxidant property of plant extractives: enhancement of bioactivity- A review	<u>Teema Thomas</u> Arun Kumar Thalla	NCCE-NITK, NITK Surathkal.	30-31 Jan 2020	3

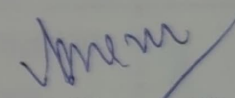
* Category: 1: Journal paper, full paper reviewed 2: Journal paper, Abstract reviewed 3: Conference/Symposium paper, full paper reviewed 4: Conference/Symposium paper, abstract reviewed 5: others (including papers in Workshops, NITK Research Bulletins, Short notes etc.)


20/10/2023

Teema Thomas

Research Scholar

Name & Signature, with Date



Dr. Arun Kumar Thalla

Research Guide

Name & Signature, with Date